EARLY MIOCENE CARBONATE DISSOLUTION IN THE EASTERN EQUATORIAL PACIFIC

A Dissertation

by

JULIA KEEGAN WILSON

Submitted to the Office of Graduate and Professional Studies of
Texas A&M University
in partial fulfillment of the requirements for the degree of

DOCTOR OF PHILOSOPHY

Chair of Committee,	Mitchell Lyle
Committee Members,	Niall Slowey
	Franco Marcantonio
	Matthew Schmidt
Head of Department,	Deborah Thomas

December 2014

Major Subject: Oceanography

ABSTRACT

As the world's largest ocean, the Pacific Ocean is intrinsically linked to the major changes in current and past climate via several mechanisms, in particular, through the carbon cycle's influence on atmospheric CO_2 concentrations. One way to understand the ocean carbon cycle is to study fluctuations in the $CaCO_3$ content of ocean sediments and determine the nature, timing, and drivers of those events. As part of a larger effort to reconstruct Cenozoic paleoclimate in the eastern equatorial Pacific, XRF records are used here to define an early Miocene low $CaCO_3$ event in the equatorial Pacific that corresponds to the seismic horizon termed "Lavender". The low $CaCO_3$ interval is correlated at submeter scale in 4 drill sites from IODP Expedition 320/321 and has been identified by seismic reflection throughout the region, indicating a large perturbation in the global carbon cycle at the time of its deposition. Using multi-element XRF data, we have determined that this event was caused by $CaCO_3$ dissolution, with peak dissolution occurring at 16.9 Ma. The event begins prior to the Miocene Climate Optimum (MCO) with peak dissolution coinciding with the initial warming step of the MCO. Three potential disrupters of $CaCO_3$ deposition are investigated: a change in organic carbon burial to the deep ocean, reducing deep dissolved inorganic carbon (DIC); a change in mantle CO_2 outgassing associated with the formation and emplacement of the Columbia River basalt province; and basin-basin fractionation, where development of a new $CaCO_3$ depocenter in the Atlantic reduces $CaCO_3$ deposition in the Pacific. Of these 3 possibilities, the timing of the Lavender event favors basin-basin fractionation.

DEDICATION

"For all things come of thee, and of thine own have we given thee."

1 Chronicles 29:14

ACKNOWLEDGEMENTS

I would like to thank my committee chair, Dr. Mitchell Lyle, and my committee members, Drs. Franco Marcantonio, Niall Slowey, and Matthew Schmidt, for their guidance and support throughout the course of this research. I would especially like to thank Mitch for reminding me that it does not matter how much work you do if you do not write it down.

A large portion of my work was completed at IODP in the ODASES lab, so special thanks go to David Houpt and Phil Rumford at IODP for all of their help early on in my research. Their training and assistance with the XRF scanning and core sampling were invaluable.

I want to thank my friend, Jennifer Hertzberg, for keeping me grounded and allowing me to bounce ideas off of her, as well as for writing down my thesis topics and reminding me of them when needed. Also, thanks to Jennifer for her help in editing and reviewing my manuscripts, and for her star power. Special thanks go to Dr. Anna Stepanova for all of her help with the chemistry portion of my work. It was nice to have someone in the lab to work with and learn from. Thanks to Andrew Parker for computational assistance and to Luz Romero for help with the geochemical analyses.

Funding for this project was provided by the ODASES program at TAMU, a post-cruise USAC grant to Dr. Mitchell Lyle, NSF grant OCE-0962184 to Dr. Mitchell Lyle, and NSF S-STEM grant 0806926 to Drs. Mary Jo Richardson and Wilford Gardner. Additional funding was provided by a number of scholarships and fellowships

from the Department of Oceanography, the College of Geosciences, and the Texas Sea Grant Program.

Thanks to my family for their incredible support throughout my studies which included yet another move across the country. Finally, thanks to my wonderful husband for believing in me and pushing me to succeed. I could not have done this without all of your support and love.

NOMENCLATURE

Al	Aluminum
Al_2O_3	Aluminum Oxide
AgCl	Silver Chloride
Ba	Barium
$BaSO_4$	Barium Sulfate
bio-Ba	Biogenic Barium
bio-SiO_2	Biogenic Silica or Opal
BSU	Boise State University
C	Carbon
(C)	Component
Ca	Calcium
$CaCO_3$	Calcium Carbonate
CaO	Calcium Oxide
CCD	Carbonate Compensation Depth
CCSF-A	Core Composite Depth Below Seafloor
Cl	Chlorine
cm	Centimeter
C_{org}	Organic Carbon
CO_2	Carbon dioxide
$CO_{2(aq)}$	Aqueous Carbon Dioxide
CO_3^{2-}	Carbonate Ion

CSF-A	Core Depth Below Seafloor
Cu	Copper
DDW	Type II reagent-grade deionized water
DIC	Dissolved Inorganic Carbon (ΣCO_2)
DOC	Dissolved Organic Carbon
DSDP	Deep Sea Drilling Project
EEP	Eastern Equatorial Pacific
eV	Electron Volt
Fe	Iron
Fe_2O_3	Iron Oxide
GPTS	Geomagnetic Polarity Time Scale
GIN	Greenland, Iceland, Norwegian
h	Hour(s)
HCl	Hydrochloric Acid
HCO_3^-	Bicarbonate
H_2CO_3	Carbonic Acid
$HClO_4$	Perchloric Acid
HF	Hydroflouric Acid
HNO_3	Nitric Acid
H_2O	Water
H_2O_2	Hydrogen Peroxide
H_3PO_4	Phosphoric Acid

HR-ICP-MS	High Resolution Inductively Coupled Plasma Mass Spectrometer
IC	Inorganic Carbon
ID	Identification
In	Indium
IODP	Integrated Ocean Drilling Program
K	Potassium
K_2O	Potassium Oxide
ka	Thousands of Years Ago
km	Kilometer(s)
KOH	Potassium Hydroxide
kV	Kilovolt(s)
LIP	Large Igneous Provence
m	Meter(s)
M	Molar
Ma	Million Years Ago
MAR	Mass Accumulation Rate
mbsf	Meters Below Seafloor
mcd	Meters Composite Depth
$\text{Med\%}_e$	Median Weight Percent of a Sedimentary Component
mg	Milligram(s)
mg/L	Milligram per Liter
milli-Q	Type I, Ultrapure Water

min	Minute(s)
mL	Milliliter(s)
mm	Millimeter(s)
MCO	Miocene Climate Optimum
Mn	Manganese
MnO	Manganese Oxide
m.y.	Million Years
μA	Microamperes
μg	Microgram(s)
μL	Microliter(s)
μm	Micrometer(s)
N	Normal
Na_2CO_3	Sodium Carbonate
NADW	North Atlantic Deep Water
NCW	Northern Component Water
NMS	Normalized Median-Squared
NMS_C	Normalized Median-Squared of some Component (C)
NIST	National Institute of Standards and Technology
nm	Nanometer
ODP	Ocean Drilling Program
pCO_2	Partial Pressure of Carbon Dioxide
PEAT	Pacific Equatorial Age Transect

PeakArea_e	Peak Area of the Element
$\text{PeakArea}_{e,med}$	Median Peak Area of the Element
PhD	Doctor of Philosophy
ppb	Parts per Billion
Rh	Rhodium
rpm	Revolutions per Minute
s	Second(s)
S	Sulfur
S_e	Elemental Scaling
Si	Silicon
SiO_2	Silica
Th	Thorium
Ti	Titanium
TiO_2	Titanium Dioxide
U	Uranium
USA	United States of America
wt%	Weight Percent
XRF	X-Ray Fluorescence
y	Year(s)
~	Approximately
[ ]	Concentration
°	Degree(s)

°C/N/W	Degrees Celcius/North/West
ΣCO_2	Dissolved Inorganic Carbon (DIC)
>	Greater Than
‘	Minutes
%	Percent
‰	Per Mil

TABLE OF CONTENTS

Page

LIST OF FIGURES

Page

LIST OF TABLES

Page

`

CHAPTER I

INTRODUCTION

1.1 Background

The study of carbonate chemistry is integral to developing a further understanding of the potential impacts of increased atmospheric carbon dioxide (CO_2) and changes in calcium carbonate ($CaCO_3$) compensation in the oceans. The $CaCO_3$ records of concentration, accumulation rate, etc., reflect changes in ocean circulation, ocean chemistry, and upper ocean productivity, as well as atmospheric CO_2. Additionally, carbonate saturation state and carbonate dissolution influence isotopic and elemental records of ocean chemistry and temperature. The distribution of $CaCO_3$ in marine sediments throughout the equatorial Pacific Ocean can be correlated for thousands of kilometers and shows coherent variability [*Anderson et al.*, 2008; *Lyle et al.*, 2002; *Farrell and Prell*, 1991; *Mayer et al.*, 1985]. Accumulation of $CaCO_3$ or calcite in marine sediments can only occur above the calcite compensation depth (CCD) and typically, above the lysocline. The lysocline is the depth in the ocean at which the solubility of $CaCO_3$ increases substantially and $CaCO_3$ begins to dissolve [*Boudreau et al.*, 2010]. The CCD is the depth below which calcite cannot accumulate in the sediments [*Berger*, 1972; *Müller and Mangini*, 1980; *Volat et al.*, 1980]. The questions of how and why $CaCO_3$ variability in marine sediments is generated are integral to developing a further understanding of the potential impacts of increased atmospheric carbon dioxide (CO_2) and changes in $CaCO_3$ compensation depth in the oceans. Changes in the $CaCO_3$ content of sediments further back in time can provide records of

`

variability in oceanic conditions at longer scale periodicities and information regarding variations in climate over those time periods.

Three main factors govern $CaCO_3$ content in marine sediments: (1) dilution by non-carbonate terrigenous material, (2) fluctuations in the productivity of calcite-secreting organisms versus silica-secreting ones, and (3) carbonate dissolution [*Volat et al*., 1980; *Cranston and Buckley*, 1990]. In the eastern equatorial Pacific (EEP), dilution by terrigenous material is generally disregarded as a cause of decreased $CaCO_3$ content in sediment due to the lack of river basins draining into the area and the lack of eolian dust input to the area [*Volat et al*., 1980]. Windblown dust is typically 1-5% of the total sediment [*Piela et al*., 2012; *Xie and Marcantonio*, 2012; *Hovan*, 1995] and is not sufficient to dilute the biogenic fraction.

Because changes in climate clearly influence productivity, it follows that productivity and $CaCO_3$ content of sediment should be related, however there is a question as to whether higher productivity will necessarily result in increased $CaCO_3$ accumulation [*Volat et al*., 1980]. Increased upwelling, the cycling up of nutrients from below the thermocline, will result in increased productivity by siliceous organisms, as well as calcareous organisms. In the EEP, where terrigenous input is negligible, increased upwelling would therefore result in higher sedimentation rates. Sediment trap data show a strong correlation between the increase in organic carbon (C_{org}) rain and both $CaCO_3$ and opal fluxes, however the increase in $CaCO_3$ slows with productivity while the increase of opal flux continues to increase [*Dymond and Collier*, 1988; *Honjo et al*., 1995]. Evidence for productivity as a control on $CaCO_3$ sedimentation also

`

includes the apparent co-variation of accumulation rates of $CaCO_3$ along with other biogenic phases, such as opal, phosphorous, and organic matter [*Anderson et al.*, 2008]. Since it is not expected that other biogenic phases would be sensitive to changes in $CaCO_3$ preservation, co-variation would indicate a biological productivity control on the $CaCO_3$ accumulation in the sediments.

However, accumulation rates of biogenic phases in EEP sediments evaluated by normalizing to ^{230}Th do not show the expected pronounced glacial maxima evident in records generated using more traditional stratigraphic methods [*Anderson et al.*, 2008; *Marcantonio et al.*, 1996; *Thomas et al.*, 2000]. Results of studies by *Marcantonio et al.* [1996] and *Thomas et al.* [2000] indicate that productivity, at least in the EEP, is just one of the controls on $CaCO_3$ sedimentation. *Lyle et al.* [2000] argues that there is a depositional spike of $CaCO_3$ (increased production of $CaCO_3$) at approximately 18 thousand years ago (ka), although there is a strong dissolution signal as well.

The $CaCO_3$ content in marine sediments is largely controlled by changes in the [CO_3^{2-}] of seawater [*Anderson et al.*, 2008]. Sea surface pCO$_2$ depends both on the concentration of aqueous CO_2 ($CO_{2(aq)}$) and its solubility coefficient [*Marchitto et al.*, 2005]. One of the mechanisms which can lower sea surface $CO_{2(aq)}$ is the speciation of dissolved inorganic carbon (DIC or ΣCO_2) shifting away from $CO_{2(aq)}$. DIC is represented by the following:

$$DIC = \left[CO_{2(aq)}\right] + [HCO_3^-] + [CO_3^{2-}]$$

where the concentration of $CO_{2(aq)}$ is negligible [*Marchitto et al.*, 2005]. Carbon dioxide is utilized in the ocean through the following equations:

`

$$CO_{2(aq)} + H_2O \leftrightarrow H_2CO_3$$

where H_2CO_3 (carbonic acid) is produced and immediately dissociated and hydrogen ions (H^+) are produced via the following:

$$H_2CO_3 \leftrightarrow HCO_3{}^- + H^+$$

$$HCO_3{}^- \leftrightarrow CO_3{}^{2-} + H^+$$

The increase of H+ ions decreases the pH, thereby causing the seawater to become more acidic:

$$pH = -log[H^+]$$

As pH decreases, acidity increases, and vice versa. This increase in acidity is buffered through the use of CO_3^{2-}, which reacts with some of the $CO_{2(aq)}$ as it is drawn down from the atmosphere to produce more HCO_3^-:

$$CO_{2(aq)} + CO_3{}^{2-} + H_2O \rightarrow 2HCO_3{}^-$$

This causes the decrease in acidity to proceed more slowly than it would in an unbuffered system. As the concentration of $CO_{2(aq)}$ increases, an increased amount of CO_3^{2-} is used in system buffering and therefore is unavailable for marine organisms to use through their biological functions and we see dissolution of $CaCO_3$ to compensate.

Remembering the definition of DIC, the concentration of $CO_{2(aq)}$ drops as the DIC equilibrium shifts to the right and the ratio of alkalinity to DIC increases, thereby increasing $CaCO_3$ preservation. Conversely, $[CO_3^{2-}]$ drops as the ratio of alkalinity to DIC decreases [*Marchitto et al.*, 2005], as when atmospheric CO_2 is taken up by the ocean. The CO_3^{2-} decrease, therefore, promotes dissolution of $CaCO_3$ throughout the water column as well as at the seafloor. Additionally, as increased organic matter

`

reaches the sea floor and is respired, metabolic CO_2 is released into pore waters, resulting in additional $CaCO_3$ dissolution [*Volat et al.*, 1980; *Emerson and Bender*, 1981]. $CaCO_3$ dissolution, at least in the EEP, is the main factor governing the content of $CaCO_3$ in marine sediments.

Currently the earth is in a period of time of rapidly increasing atmospheric [CO_2] due to burning fossil fuels, and it is essential to understand how changes in the level of atmospheric CO_2 affect the global oceans. One way to examine potential future changes resulting from increased CO_2 in the oceans is to look at past fluctuations in the $CaCO_3$ content of ocean sediments and determine the nature, timing, and drivers of those fluctuations.

1.2 Study Area

The Integrated Ocean Drilling Program (IODP) Pacific Equatorial Age Transect (PEAT) project was designed to recover a continuous Cenozoic record of the equatorial Pacific by coring above the paleoposition of the equator at successive crustal ages on the Pacific plate with the goal of constructing a Cenozoic megasplice to better understand climate change over the last 60 million years (m.y.). One of the primary goals of the PEAT project is to produce continuous records tracking the effects of climate change in the EEP with enough detail to resolve orbitally-forced climate cycles. An additional goal is to detail the nature and changes of the CCD throughout the Cenozoic [*Pälike et al.*, 2010].

A significant part of climate change is recorded by variability in the chemical composition of sediments. The goal of this PhD project is to target the beginning of the

`

Neogene, from the Oligocene-Miocene boundary through the beginning of the Miocene Climate Optimum (MCO) using sediment cores collected during IODP Expeditions 320/321, focusing on the carbonate dissolution event that occurred around approximately 17 million years ago (Ma). This event was first identified on seismic sections collected as part of Deep Sea Drilling Program (DSDP) Leg 85. *Mayer et al*. [1986] designated this seismic horizon as the "Lavender" horizon, and we have used this designation throughout this project. Figure 1 shows a correlation of field seismic data and synthetic seismogram for DSDP Site 574, with the Lavender seismic interval highlighted. The Lavender seismic horizon is associated with a major, sharp, early Miocene decrease in $CaCO_3$ and is regionally traceable, seen in cores collected during DSDP Leg 85, Ocean Drilling Program (ODP) Leg 199, and IODP Expedition 320/321.

1.2.1 Transect and Individual Site Locations

Four individual site locations cored as part of the IODP Expedition 320/321 PEAT project contain the major Neogene sediment sections for the equatorial Pacific megasplice: U1335, U1336, U1337, and U1338. These sites are located between 7°42'N and 2°30'N and range from approximately (~) 4200 to ~4400 meters (m) water depth (see Chapter II). What makes these locations ideal for studying the early Neogene is their location on the northwestward moving Pacific Plate. The plate moves northwest at a rate of ~0.25° per million years, thus coring locations are moved out of the high-productivity, high-sedimentation zone at the equator, preventing older sediments from being buried too deeply beneath younger sediments [*Pälike et al.*, 2010]. Details regarding individual site locations are provided in Chapters II and IV.

`

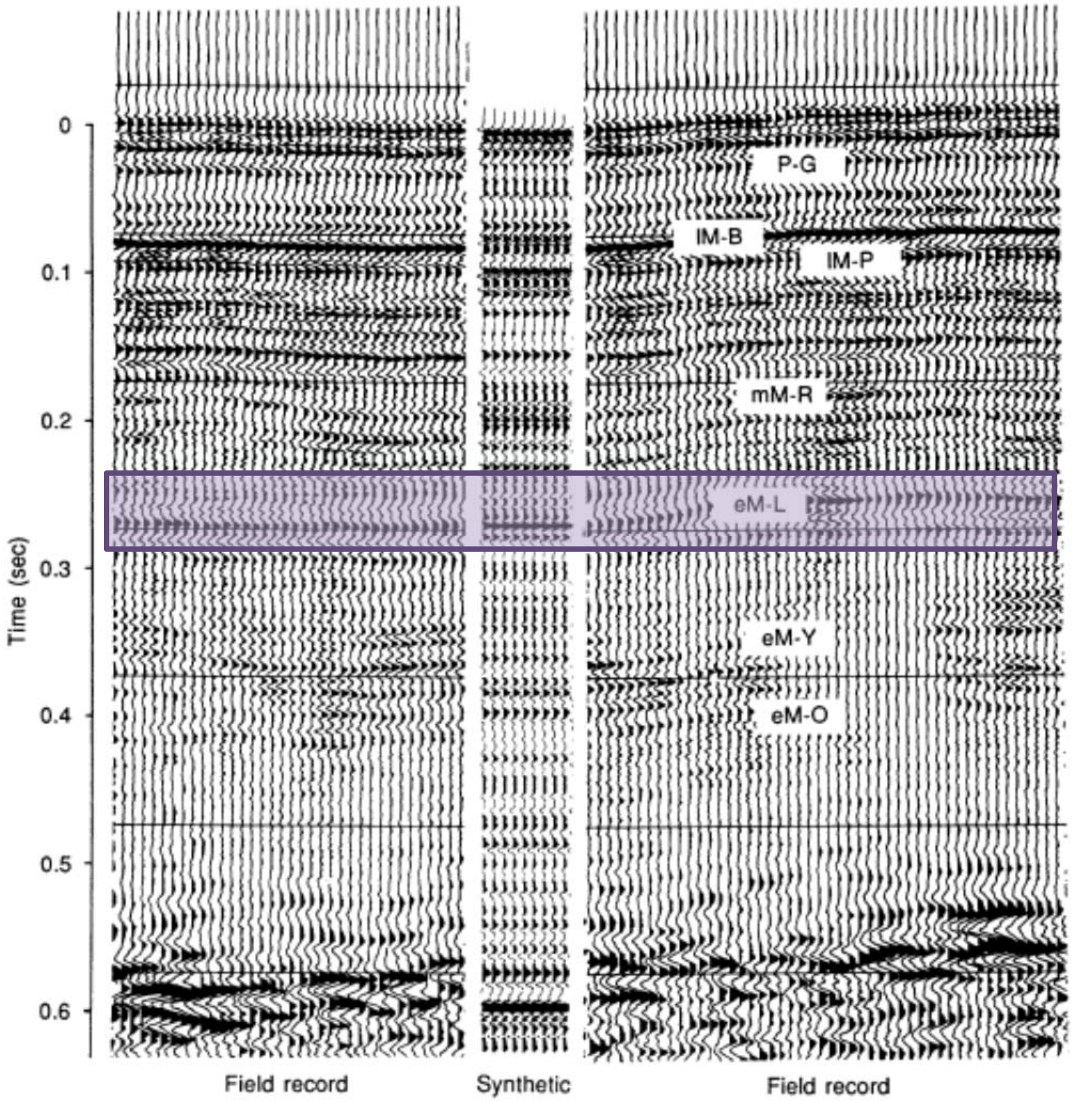

Figure 1 Lavender seismic interval. Correlation of field seismic data from an 80-cubic-inch water gun with synthetic seismogram at DSDP Site 574 with the Lavender seismic interval highlighted. [Modified from *Mayer et al.,* 1986].

`

1.3 Study Goals

The EEP provides an ideal setting to explore the major changes in the global climate system throughout the Cenozoic. The period of time just following the Oligocene-Miocene transition has been largely ignored in previous studies, so filling this data gap will provide further information on changes in the carbon cycle between ~15 and 23 Ma. The goals of this project are to:

1. Collect and calibrate bulk sediment chemistry data on IODP Expeditions 320/321 Neogene cores, U1335, U1336, U1337, and U1338 for the appropriate Neogene sections.
2. Determine the difference between dissolution and productivity signals in the IODP Expeditions 320/321 Neogene cores, U1335, U1336, U1337, and U1338 and to correlate carbonate dissolution events across multiple cores.
3. Examine the nature, timing, and potential forcing mechanisms of the Lavender Dissolution Interval which occurred at ~17 Ma and was identified by *Mayer et al.* in 1985, and correlate the event across the region.
4. Compare other climate proxy records, including those of benthic foraminiferal $\delta^{13}C$ and $\delta^{18}O$, and the timing of changes in these proxy records in relation to the dissolution event and explore potential causes of differences in that timing.

`

1.4 Hypotheses

Based on the stated goals of this study, the hypotheses of this research project are as follows:

1. X-ray fluorescence (XRF) scanning can be used to distinguish between productivity and dissolution events occurring during the Miocene as seen in sediment cores.
2. The Lavender seismic horizon identified by *Mayer et al*. [1985] was a $CaCO_3$ dissolution event that can be correlated across the EEP.
3. The Lavender Dissolution Interval was the result of basin-basin fractionation caused by an increase in Atlantic Northern Component Water (NCW) formation and $CaCO_3$ deposition in the Atlantic.

1.5 Manuscript Organization

This dissertation is organized into five chapters. Chapter I provides an introduction to the project, a review of the carbon cycle, and possible drivers for the decreased carbonate content of sediment cores in the EEP. Additionally, study goals and hypotheses are stated in this chapter.

Chapter II is a data report reprinted with permission from IODP and details the procedures for XRF scanning and initial data collection that is the basis of this work. This chapter addresses parts of Study Goals 1 and 2 and Hypothesis 1.

Chapters III and IV will be submitted as a manuscript for publication together. Chapter III will be the supplemental material for the manuscript and includes detailed procedures for bulk geochemical analyses and XRF data calibration. The fully calibrated data sets for Sites U1335, U1336, U1337, and U1338 are provided in Chapter III. This chapter allows for full data calibration and aids in addressing Study Goals 1, 2, and 4, as well as Hypothesis 2.

Chapter IV is the bulk of the manuscript that takes the fully calibrated data sets and addresses the nature, timing, and forcing mechanisms of the Lavender Dissolution Interval in the EEP. Study Goals 3 and 4, as well as Hypothesis 3 are addressed in this chapter.

Chapter V summarizes the results presented in Chapters II, III, and IV and provides conclusions.

There are three appendices for this dissertation. Appendix A contains the data tables from Chapter II, Appendix B contains the data tables from Chapter III, and Appendix C contains the data tables from Chapter IV. As the majority of the data tables are too large and not necessarily useful in printed format, the first page of each table is included in the actual dissertation manuscript. The complete data tables are available in Microsoft Excel (.xls) format as supplementary files that will be submitted along with this written document. Shorter tables will be printed in their entirety, as well as provided in Microsoft Excel (.xls) format.

`

CHAPTER II

DATA REPORT: RAW AND NORMALIZED ELEMENTAL DATA ALONG THE SITE U1335, SITE U1336, AND SITE U1337 SPLICES FROM X-RAY FLUORESCENCE SCANNING[*]

2.1 Overview

We used X-ray fluorescence (XRF) scanning on samples from Sites U1335, U1336, and U1337 from Integrated Ocean Drilling Program (IODP) Expeditions 320 and 321 to measure sediment geochemical compositions at 2.5 and 5 centimeter (cm) resolution for a total of 937 m of spliced sediment column. Site U1335 was scanned from 0 to 302 meters composite depth (mcd), U1336 from 0 to 142.5 mcd, and for Site U1337 the entire splice from 0 to 491.6 mcd was scanned. Here we report the data and describe the data acquisition conditions to measure Al, Si, K, Ca, Ti, Mn, Fe, and Ba in the solid phase. We also describe a method to convert data from volume-based raw XRF scan data to a normalized mass measurement, ready for calibration by other geochemical methods. Both the raw and normalized data are reported along each of the splices for Sites U1335, U1336, and U1337.

2.2 Introduction

One primary objective of the Integrated Ocean Drilling Program (IODP) Pacific Equatorial Age Transect (PEAT) project is to produce continuous records tracking the effects of climate change in the eastern equatorial Pacific with enough detail to resolve

---

[*] This chapter reprinted with permission from "Data report: raw and normalized elemental data along the Site U1335, Site U1336, and Site U1337 splices from X-ray fluorescence scanning" by Julia K. Shackford, Mitchell Lyle, Roy Wilkens, and Jun Tian, 2014. *Proc. IODP*, Volume 320/321, Copyright 2014 by IODP.

`

orbitally forced climate cycles. A significant part of climate change is recorded by variability in the chemical composition of sediments, but this information is typically difficult to extract at a reasonable cost [*Lyle et al.*, 2012].

XRF scanning is an economical and nondestructive way to extract chemical data from split cores. XRF scanning is an X-ray optical technique that can measure the majority of the major elements and some minor elements in ~20–30 seconds (s) per measurement. The vertical spacing at which data were collected for this project is similar to that at which physical properties were gathered on board the ship. The chemical measurements collected from XRF scanning can supplement physical properties measurements to study cyclostratigraphy. If calibrated, XRF scan data can be used to understand the long-term evolution of biogeochemical cycles.

In this chapter, we present the results of XRF scanning on the spliced sedimentary sections from Sites U1335, U1336, and U1337 and describe a basic technique, following *Lyle et al*. [2012] used to normalize the data for further geochemical study. Both the raw and normalized data along the splices are presented in the tables (Appendix A). We report depth in meters composite depth (mcd) using core composite depth below seafloor (CCSF-A) methodology [*Expedition 320/321 Scientists*, 2010e]. Data at this sampling resolution collected from multiple cores along the transect, along with previously published data from Site U1338 [*Lyle et al*., 2012; *Lyle and Backman*, 2013], allow the study of geochemical cycles for long periods of time and across great distances in the eastern equatorial Pacific. Such data can be used to study

`

how biogeochemical changes in the equatorial Pacific are related to long-term changes in global climate.

2.3 Site Locations

The three sites in this data report, along with Site U1338, contain the major Neogene sediment sections for the PEAT equatorial Pacific megasplice. They are located between 7° 42’N and 3°50’N, and the locations are shown on Figure 1.

2.3.1 Site U1335

Site U1335 (5°18.735’N, 126°17.002’W; 4327.5 meters water depth) is situated on ~26 Ma crust and is located halfway between IODP Site U1336, ~340 km to the northwest, and IODP Site U1337, ~390 km to the southeast, ~250 km south of the Clipperton Fracture Zone [*Expedition 320/321 Scientists*, 2010a]. This site is located on a broad plateau that parallels the Clipperton Fracture Zone and is within north-northeast–trending abyssal hill topography. Drilling recovered 417 m of biogenic sediment above basement. Here we report XRF scan data at 2.5 cm spacing covering only part of the Site U1335 splice, from 0 to 302.66 mcd, covering the time span between about 0 to 20 Ma. Figure 2 shows $CaCO_3$ normalized median-squared (NMS) data from 0 to 302.66 mcd.

`

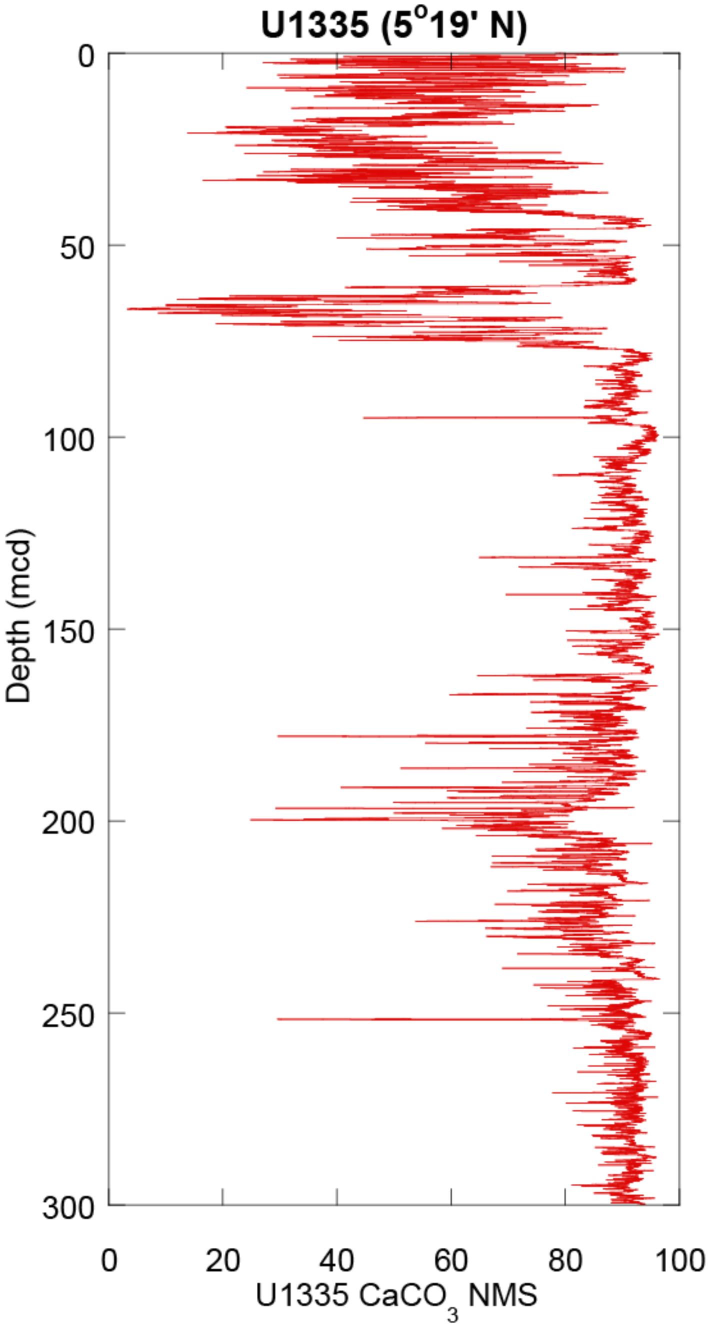

Figure 2 U1335 $CaCO_3$ NMS. Values are plotted with depth meters composite depth (mcd) for Site U1335.

`

2.3.2 Site U1336

Site U1336 (7°42.067'N, 128°15.253'W; 4286 meters water depth) is located on 32 Ma crust, ~340 km northwest of Site U1335 [*Expedition 320/321 Scientists*, 2010b]. It is ~30 km north of the center of the Clipperton Fracture Zone on a local high that is draped with ~300 m of sediment cover. The abyssal hills are oriented slightly west of due north. Coring revealed a hiatus at the top of the section to ~12 Ma. Here we report XRF scan data at 2.5 cm spacing covering only part of the Site U1336 splice, from 0 to 142.46 mcd. The Site U1336 scanning covers an age span roughly from 12 Ma (the top of the sediment column) to 22 Ma. The splice used for this project is a revised version of the shipboard splice based on *Wilkens et al*. [2013]. The revisions are due primarily to a poorly recovered interval at roughly 152 mcd that resulted in cores being appended to one another below this depth, rather than being tied together. The appended interval is below the scanned interval. Figure 3 shows $CaCO_3$ NMS data from 0 to 142.46 mcd.

`

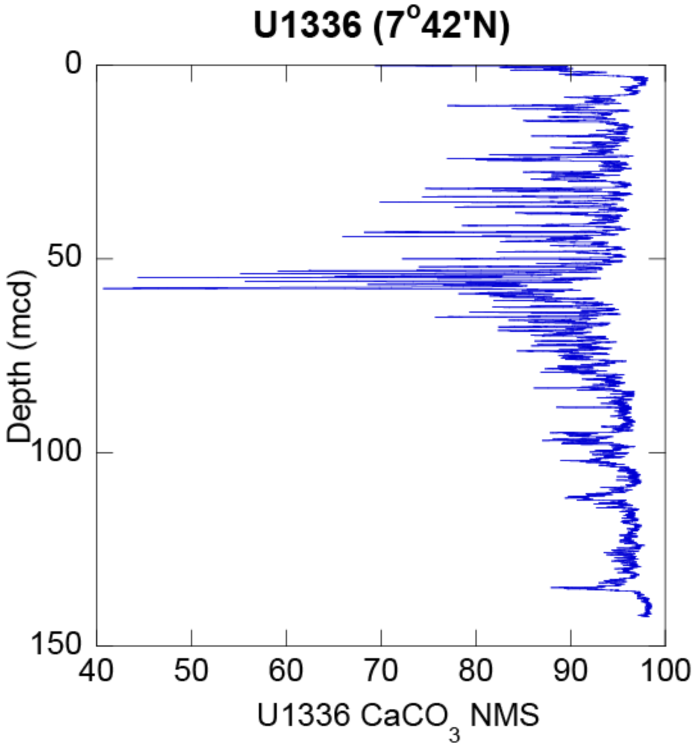

Figure 3 U1336 $CaCO_3$ NMS. Values are plotted with depth meters composite depth (mcd) for Site U1336.

`

2.3.3 Site U1337

Site U1337 (3°50.009'N, 123°12.352'W; 4463 m water depth) is located on ~24 Ma crust between the Galapagos and Clipperton Fracture Zones [*Expedition 320/321 Scientists*, 2010c]. It is situated ~390 km southeast of Site U1335. The site is on a plateau between higher topography south of the site and a ridge to the north. Here we report XRF scan data for the entire Site U1337 splice, from 0 to 491.62 mcd, covering the entire spliced section. The upper sediment column (0-102.45 cm along the splice) was scanned at 5 cm intervals in order to tie to the high-resolution scan (0.5 cm interval) scanned by Koichi Iijima [*unpublished data*]. The remainder of the sediment column was scanned at 2.5 cm spacing. The splice we use has some changes from the original shipboard splice due to core disturbance, especially at greater depth, and trouble with correlating the four cores that make up the Site U1337 splice. The splice is the revised splice reported in *Wilkens et al*. [2013]. A depth of close to 490 mcd was reached with only three gaps from the four holes. Figure 4 shows $CaCO_3$ NMS from 0 to 475 mcd for U1337.

`

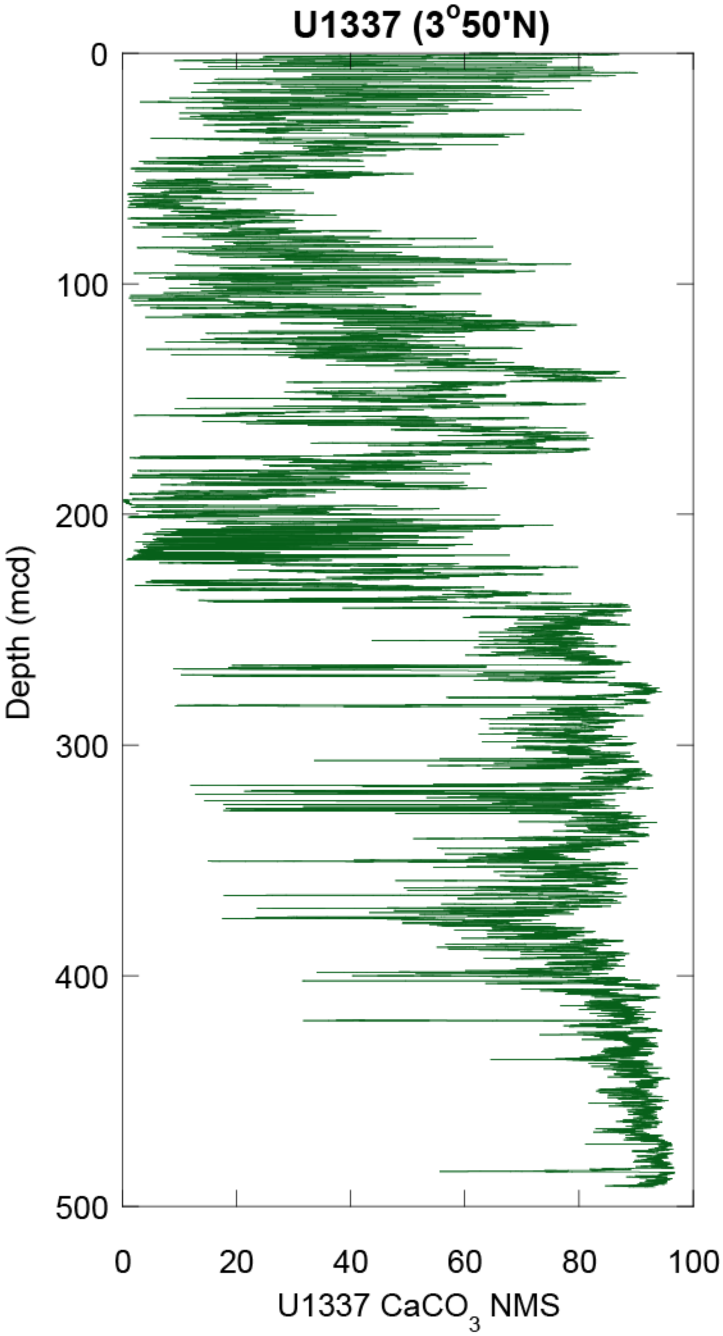

Figure 4 U1337 $CaCO_3$ NMS. Values are plotted with depth meters composite depth (mcd) for Site U1337.

2.4 X-Ray Fluorescence Scanning of the Sites U1335, U1336, and U1337 Spliced Sections

Sites U1335, U1336, and U1337 exhibit the characteristic variations in sedimentary calcium carbonate content that result in the common seismic stratigraphy found throughout the equatorial Pacific east of Hawaii [*Mayer et al*., 1986]. It has been difficult in the past to understand and determine what forcing mechanisms caused these carbonate cycles, which in turn caused these common seismic horizons, because they were poorly resolved by low-resolution shipboard sampling and analysis. Through the use of XRF scanning and discrete geochemical sampling to calibrate the XRF scan data, we can potentially determine calcium carbonate content, biogenic opal, biogenic barium (bio-Ba), and clay content in fine enough detail to better understand why sedimentary carbonate has varied in the equatorial Pacific.

XRF scanning can be used to study the biogeochemically active elements Ca, Si, and Ba in order to understand changes in productivity [*Lyle et al*., 2012]. These data can then be compared to changes in preservation to further understand changes in the overall carbon cycle. XRF scan data can also be used to measure alumnosilicate elements including Al, K, and Ti to better understand the dust input to the region [*Lyle et al*., 2012]. Measuring redox-sensitive elements such as Fe and Mn gives information about the sedimentary redox environment, as well as a measure of distal hydrothermal plume deposition near the basement [*Lyle et al*., 2012].

XRF uses the characteristic fluorescence of elements exposed to high-energy X-ray illumination to estimate a sample’s chemical composition. High-energy X-ray

`

photons eject inner-shell electrons from atoms being illuminated by the X-rays [*Jansen et al*., 1998], and the vacancies are filled by outer shell electrons. The excess energy is released as characteristic X-ray fluorescence energies for each element. The intensity of the fluorescence can be used to determine the abundance of different elements within the illuminated sample. With a scanning XRF, the detector is moved by a stepping system along a sediment core so that multiple measurements can be taken automatically [*Richter et al*., 2006].

2.5 Methods and Materials

The spliced sediment columns from Sites U1335, U1336, and U1337 were XRF-scanned using the third-generation Avaatech XRF scanner at the IODP Gulf Coast Repository in College Station, Texas (USA) (odases.tamu.edu/research-facilities/xrf-request/). This XRF scanner is equipped with a Canberra X-PIPS SDD, model SXD 15C-150-500 150 eV resolution X-ray detector and uses an X-ray tube with a Rh-anode to generate the incident X-rays that illuminate the sample. The XRF scanner is configured to analyze split sediment core halves for elements between Al and U on the periodic table. The X-ray tube and detector are mounted on a moving track so that multiple spots at different depths can be analyzed on a split core during the scanning run and multiple scans with different settings can be programmed in to run automatically [*Richter et al*., 2006]. There are, however, parameters that are controlled by the operator, such as X-ray tube current, voltage, measurement time (live time), filters, and area of X-ray illumination. The downcore position step is precise to 0.1 millimeter (mm).

2.5.1 XRF Scanning

Sample spacing along each of the Site U1335 and U1336 core sections was set at 2.5 cm. For Site U1337, sample spacing was set at 2.5 cm in the lower spliced section and 5 cm in the 0-110 mcd section overlapping with Iijima's work. Two separate scans at different voltages were used on each section to gather all the chemical data. The first scan was performed at 10 kilovolts (kV) with no filter for the following elements: Al, Si, S, Cl, K, Ca, Ti, Mn, and Fe. The measurement (live) time was set at 30 s and the X-ray tube current was set to at 500 μA. A second scan for Ba was performed at 50 kV with a Cu filter, a measurement time of 10 s and the X-ray tube current set to 1000 μA. We lowered the X-ray tube current from 2000 μA used for the Site U1338 scanning [*Lyle et al*., 2012] in order to preserve tube life and reduce the possibility of peak overlap problems. The core face illuminated by X-rays was set at 1.0 cm in the downcore direction and 1.2 cm in the cross-core direction.

For the Site U1335 and U1337 cores, the scans were run down the center of the split core half (6.8 cm total diameter). For the Site U1336 cores, the majority of the scans were run down the left side of the split core half to avoid the U-channel gap left by sampling for magnetostratigraphic analyses on the archive core prior to the XRF scanner runs. On the U-channeled sections, the track in the XRF core scanner was offset ~3 cm from the core's center line. Additionally, cracks and holes from sampling in any of the cores were skipped if they corresponded with XRF sample spacing.

Each core was removed from refrigeration a minimum of 8 hours (h) prior to scanning to allow it to warm to room temperature. Each section was then covered ~15

`

min prior to scanning with 4 micrometers (µm) thick Ultralene plastic film from SPEX Centriprep, Inc. to protect the detector face from becoming contaminated during the scan. Following the methods in *Lyle et al*. [2012], the Ultralene film was placed over the core sections only once they had warmed to room temperature in order to avoid condensation building up on the film while the core sections warmed. Condensation buildup can lead to severely reduced light element (ex. Al and Si) XRF peak areas due to the condensation absorbing the low energy X-ray fluorescence coming back from the sediment to the detector [*Tjallingii et al*., 2007].

There were a few unexplained data dropouts that we found after plotting the data, one and occasionally two data points that were significantly lower than the data trends of the scan. Where we had overlapping data we found these “events” on only one of the overlapping sections. We attribute the dropouts to an intermittent instrument failure and removed them from the data sets, including those shown in Tables A1-3. We found 15 bad data points between 109 and 114 mcd in the Site U1336 core sections. Of the 15 bad data points found in the Site U1336 splice, 7 were outside of the splice, meaning they were in the overlapped section and would not have been included in the final splice even if they were kept, and 8 were within the splice, meaning that they would have been included in the final splice. All 15 bad data points were removed. Two additional bad data points were found in the Site U1336 splice at ~32 and ~83 mcd. Both of these points were removed as well.

`

2.5.2 Sediment Splices

XRF scanning was done to cores along the sediment splices, not to all sections recovered from the different holes at each site. Only core sections along the continuous spliced sections of Sites U1335 and U1336 were analyzed. We XRF scanned every archive core half included on the Site U1336 and U1337 splice tables in 2011 and 2012 and completed the XRF scanning of the Site U1335 spliced sections in January 2013. If the splice transferred from one hole to the next in the middle of a section, both sections were run in their entirety to provide enough overlap to allow for the record to be adjusted, if needed. In the Site U1337 splice, substantial changes have been made to the original continuous splice table, so additional sections were run to aid in revising that record.

Tables A1-3 contain all of the data collected, not just the data that were used to construct the final splice. Data incorporated into the splice are marked for easy extraction. Each table includes raw XRF peak area data NMS reduced data for all three cores. Depths are indicated in meters below seafloor (mbsf), which is equivalent to core depth below seafloor (CSF-A), as well as converted to meters composite depth (mcd), which is equivalent to core composite depth below seafloor (CCSF-A). References to depth throughout this dissertation are in mcd. Table A1 provides data for Site U1335, Table A2 for Site U1336, and Table A3 for Site U1337. Medians of shipboard geochemical data and calculated area medians, both used in scaling and normalizing the raw XRF area data, are presented in Table A4. For each element in Tables A1-3 we

`

have listed the raw XRF peak area, the median-scaled total, and the NMS data as described below.

2.5.3 XRF Data Reduction

Data reduction was accomplished by a three-step method generally following the methods in *Lyle et al*. [2012]. In the first step, which is an addition to the two-step reduction method developed in *Lyle et al*. [2012], negative peak area values were set to zero and removed from further calculations. Negative peak areas can appear where there are overlapping peaks and the elemental concentration is low. In this case, the measured data are actually below the modeled energy curve at 0 concentration.

Second, data were scaled by the median shipboard-measured bulk sediment elemental composition in order to scale elemental peak areas into typical ranges of sediment composition (Table A4). Finally, the scaled components were summed and normalized to 100% in order to account for changes in porosity and cracks throughout the core sections. Only sections used in the final splices were used in calculating the area medians, so changes to the final splices may require recalculation of those medians, and therefore NMS values.

To scale the XRF data, the following equation from Lyle et *al*. [2012], was used:

$$S_e = Med\%_e \times \left(PeakArea_e / PeakArea_{e,med}\right)$$

where S_e is the elemental scaling, $Med\%_e$ is the median weight percent of a sedimentary component, which was the oxide for each element (e.g., for Al, we used the oxide Al_2O_3, and for Ca, $CaCO_3$) from shipboard geochemical data, $PeakArea_e$ is the measured

`

elemental peak area in the sample, and $PeakArea_{e,med}$ is the median peak area over the data set.

To normalize the scaled XRF data, thereby removing the volume effect, each component (C) was multiplied by 100/(raw sum) to bring the total sum of components to 100%, rather than the lower value that results from high porosity or cracks:

$$NMS_C = (C) \times (100/raw\ sum)$$

where NMS_c is the normalized median-scaled value for the component and (C) is the median-scaled value of the component. The sedimentary components in these data sets are: Al_2O_3, SiO_2, K_2O, $CaCO_3$, TiO_2, MnO, Fe_2O_3, and $BaSO_4$. Normalization minimizes the high-frequency noise produced from greater porosity in the shallower portions of the splice and increased cracks and uneven surfaces in the lower sections of the splice.

Through the scaling and normalization process, we developed a way to quantitatively estimate sediment concentration based on XRF scans. XRF NMS estimates, however, can have significant errors if the model of sediment composition (the "type" sediment composition) used is very different from the actual sediment composition. In other words, errors will result if the model sediment components do not match those within the actual sediment (e.g., if Ca is found in a clay, and thus would be better represented by a CaO component) or if a major element found in the sediments is not included in the model. Despite these issues, NMS data are significantly better to study the changes in sediment composition than the raw XRF peak area since the porosity effect is removed. Raw peak area data can have larger relative errors due to the differences in porosity between the sediment layers and from technical problems landing the detector on a flat sediment surface. Very dry and cracked sediment can cause the detector not to land flat against the sediment while collecting peak area data, or to have small cracks included in the scan area and lowering the raw counts. Figure 5 shows the raw median-scaled $CaCO_3$, the NMS $CaCO_3$, and discrete $CaCO_3$ for U1335 (panel A), U1336 (panel B), and U1337 (panel C). Scaling and normalization reduces apparent noise in the XRF data and made the total range more similar to the variability seen in the shipboard data.

The NMS data can be easily calibrated to estimated sediment composition by analyzing a small set of check data that spans the typical range of sediment values and correlating the NMS data to the discrete measurements [*Lyle and Backman*, 2013].

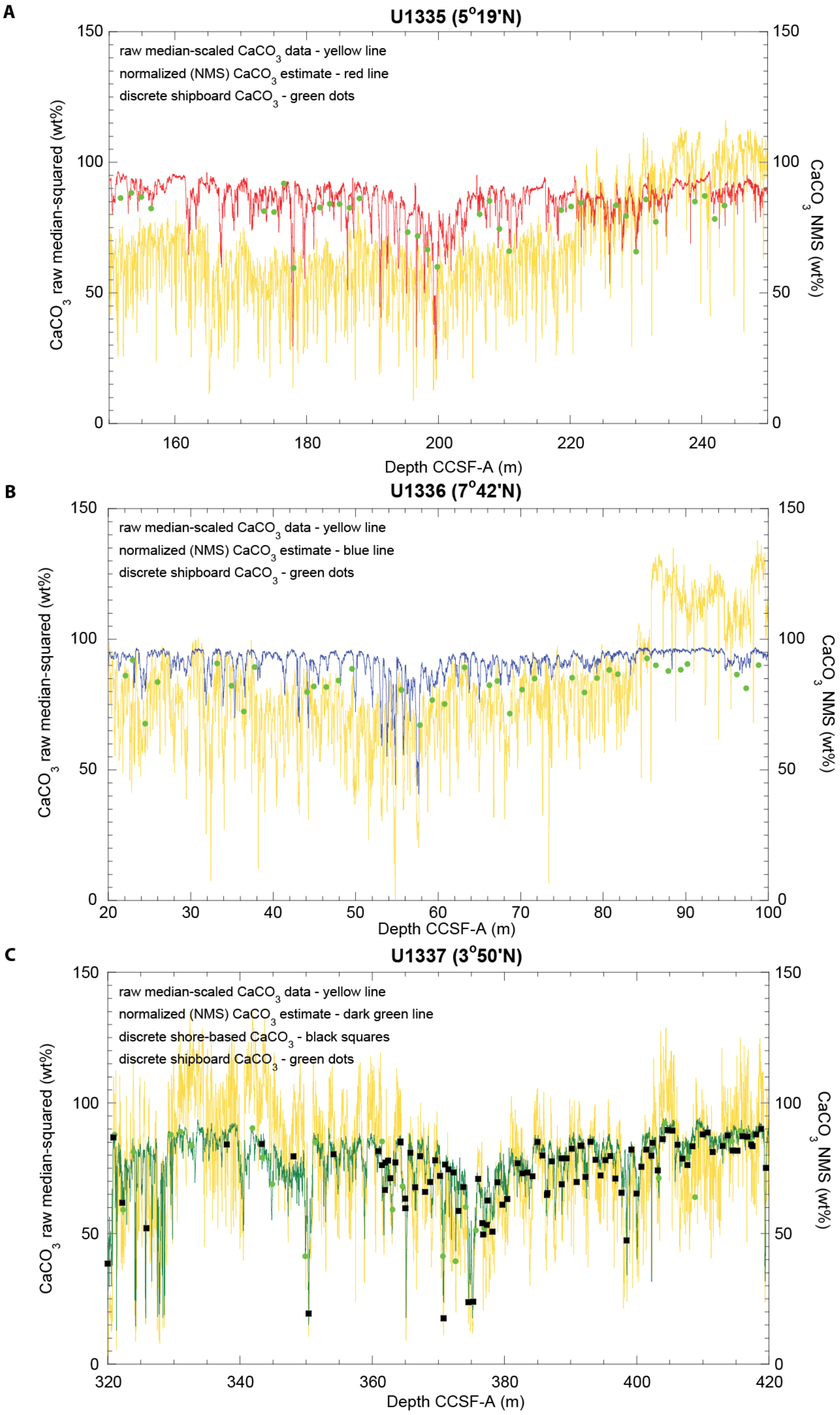

Figure 5 Comparison of raw median-scaled data with discrete samples. Raw median-scaled $CaCO_3$ data (red) are compared with normalized (NMS) $CaCO_3$ estimate (blue), discrete shipboard $CaCO_3$ (green dots), and discrete shore-based $CaCO_3$ (black squares, U1337 only). Data are shown in core composite depth below seafloor (CCSF), method A (overlapping). Normalizing the sum of components to 100% removes the amount of variability as well as corrects for volume effects. Panel A provides data for U1335, panel B for U1336, and panel C for U1337.

`

2.6 Results

One of the important uses of XRF scanning is to be able to produce high-resolution data sets, such as the >19 m.y. sediment records from Sites U1335 and U1337. The Site U1336 sediment record spans ~12.12 to 20 Ma. Figure 6 shows the NMS time series of $CaCO_3$ NMS data at three of the sites examined in this study. Also shown on that figure are biostratigraphic and magnetostratigraphic tie lines used to compare the records at each site to one another. Table A5 provides the depths, ages, and types of stratigraphic tie points shown in the figure. The upper section of the Site U1337 splice is expanded when compared with that of the Site U1335 splice due to Site U1337 being in closer proximity to the Equator since 12 Ma (1.1°–3.8°N) versus 2.4°–5.3°N for Site U1335. The closer proximity to the equator exposed Site U1337 to higher sediment deposition. As the sites moved further from the equator, they received less sediment deposition, as illustrated in the extreme by the hiatus from ~ 0 to 12 Ma at Site U1336.

`

Figure 7 shows all three sites, again with bio- and magnetostratigraphic tie lines, focusing on a very prominent $CaCO_3$ low that peaks at ~16.9 Ma and begins ~17.6 Ma. The age is earlier than the usually assumed start of the Monterey carbon isotope excursion [16.9–13.7 Ma; *Holbourn et al*., 2007] but older than that of the Columbia River Basalt flood basalt eruption [~16.8-5.5 Ma; *Reidel and Tolan*, 2013], which could have released significant amount of deep CO_2 that potentially could have caused added carbonate dissolution in the oceans. The peak $CaCO_3$ dissolution occurs at or slightly after the onset of the southeast Oregon eruptions that began the deposition of the Columbia River Basalts in North America [16.8-16.6 Ma; *Barry et al*., 2013]. The flood basalt deposition and the equatorial Pacific dissolution event can only be linked if volatile degassing is associated with the emplacement of the magma in the crust, not the eruption.

The 17 Ma carbonate dissolution event lasted ~1.2 m.y. and is strongly influenced by orbital insolation changes. The $CaCO_3$ analyses indicate cyclicity on an approximately 100,000 year (y) time scale.

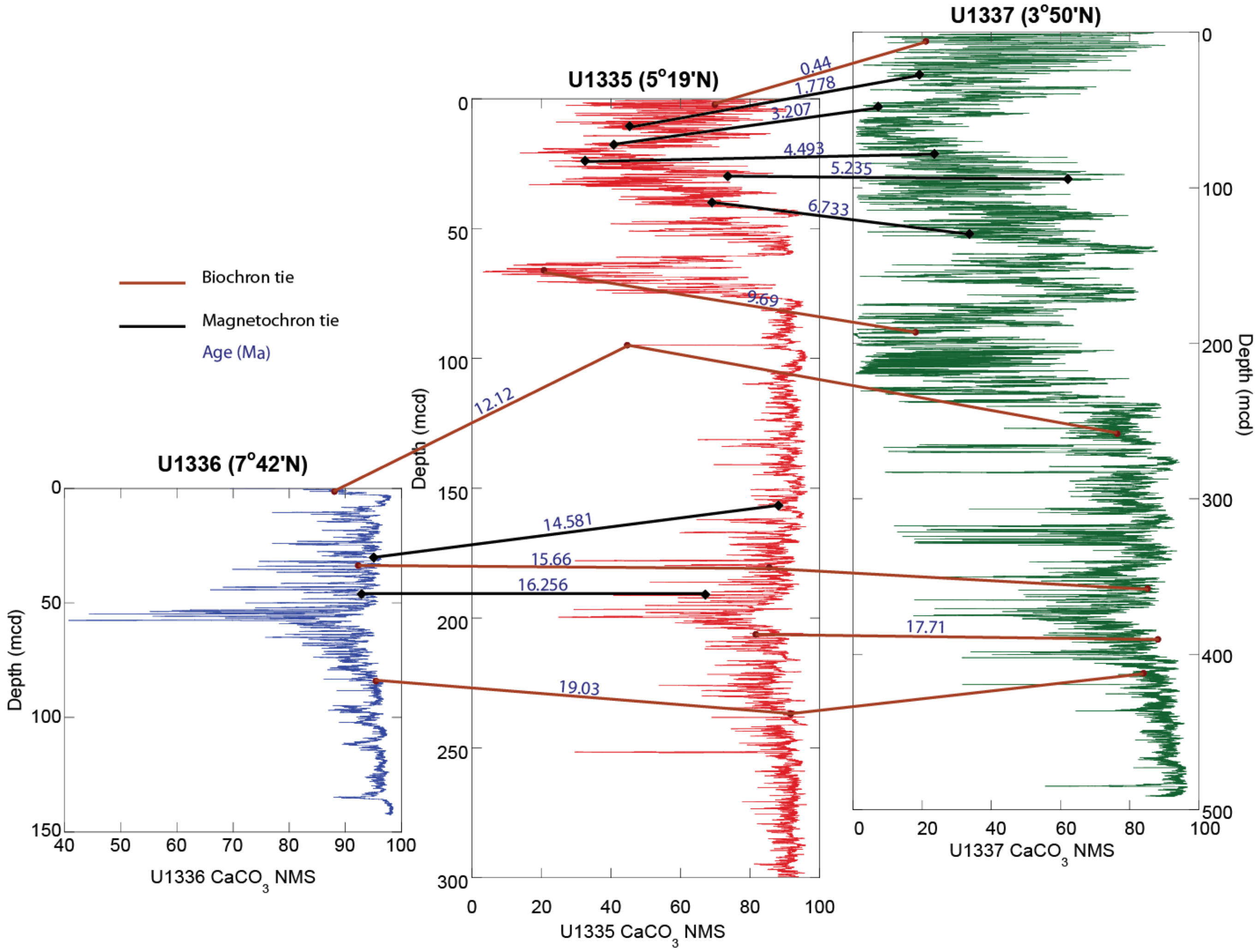

Figure 6 $CaCO_3$ NMS values and stratigraphic correlation. Correlation is between Sites U1335, U1336, and U1337. Black diamonds and lines indicate magnetostratigrapic correlation points, brown circles and lines indicate nannofossil biostratigraphic correlation points. Ages, in Ma, are shown in blue above the stratigraphic tie lines.

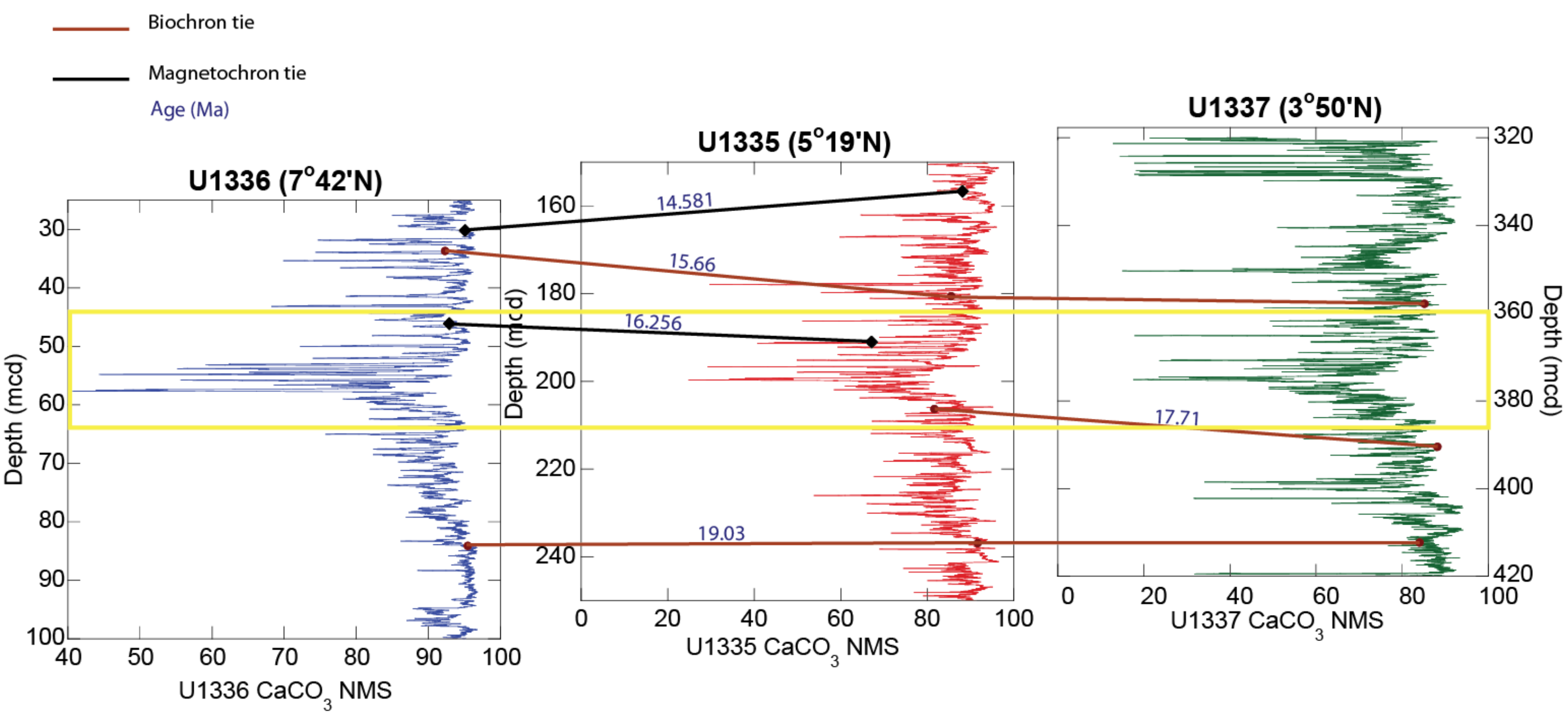

Figure 7 Focused $CaCO_3$ NMS values and stratigraphic correlation. Correlation between Sites U1335, U1336, and U1337 for the period of time surrounding the 17 Ma $CaCO_3$ dissolution interval. Black diamonds and lines indicate magnetostratigrapic correlation points, brown circles and lines indicate nannofossil biostratigraphic correlation points. Ages, in Ma, are shown in blue above the stratigraphic tie lines. Additionally, the main $CaCO_3$ dissolution signal of the Lavender event is outlined by a yellow box.

`

2.7 Conclusions

We present scanning XRF data along the splices of Sites U1335, U1336, and U1337 (41,925 total sample measurements, with 33,739 samples along the three splices) and show their use in exploring the history of the equatorial Pacific productivity zone. We found we could scan the splices for Al, Si, K, Ca, Ti, Mn, Fe, and Ba in a reasonably short amount of time, averaging slightly more than 1 hour per section. The raw data, however, are a volume measurement and must be scaled, normalized, and eventually calibrated to make an estimate of sediment composition. The NMS data reduction process described helps to make correlations between raw peak areas and measured chemical compositions more linear so that calibration is easier. To achieve good results, care must be taken to choose a sediment compositional model (median composition and type of sediment components) that is similar to the sediment under investigation. Calibration is the final step in converting XRF scan data to a compositional estimate and will be described in Chapter 3. Ideally, enough samples are measured by discrete geochemical analysis that some of the data are left out of the calibration and can be used to check the data.

`

CHAPTER III

ADDITIONAL METHODS AND XRF DATA CALIBRATION

3.1 Overview

This chapter will be submitted as the supplementary information providing analytical methods and data when Chapter 4 is submitted for publication. Various geochemical analyses were used in order to calibrate the XRF NMS data. Sediment samples were selected and obtained from the IODP Gulf Coast Repository for geochemical analysis. Samples were logged, freeze-dried, ground, and stored in plastic containers containing desiccant to prevent rehydration. Aliquots of these samples were used for elemental concentration, $CaCO_3$, C_{org}, and SiO_2 analyses.

3.2 Bulk Geochemical Analyses Methods

3.2.1 Carbon and Carbonate Analytical Methods

Inorganic carbon (IC) and C_{org} analyses were completed following *Lyle et al.* [2000] and $CaCO_3$ was determined by the "difference" method, as well as by utilizing the UIC Inc. Model CM-5012 CO_2 coulometer attached to an Automate FX automatic sample preparation module for $CaCO_3$ analysis. Total carbon was measured utilizing the coulometer that measures CO_2 released when a sediment sample is combusted. Approximately 10-15 mg of dried, homogenized sample was added to a fused quartz glass combustion boat and combusted at 1000°C. Impurities were removed from the CO_2 gas coming from sample combustion using post-combustion scrubbers. Chlorine was removed as silver chloride (AgCl) in a second furnace containing silver wool and

`

heated to 475°C. Two additional scrubbers were attached following the second furnace to remove NO_x and H_2O from the CO_2.

To measure C_{org}, homogenized samples were acidified off-line to remove $CaCO_3$ and run through the same furnace apparatus as the total carbon samples. 50-70 mg of sample was measured and placed in a fused quartz glass boat. The sample was wet with a few drops of Type II reagent-grade deionized water (DDW) and then 500 microliters (μL) of 10% HCl was added and the slurry was stirred. The glass stirring rod was rinsed with additional 10% HCl to prevent cross contamination between samples and to prevent loss of sample by sticking to the stirring rod. This process was repeated a second time and the samples were lightly covered and placed in an oven to dry. When the samples were dry, they were placed in the combustion furnace, one at a time, and the CO_2 evolved from the C_{org} samples was recorded from the coulometer. Inorganic carbon was calculated by subtracting the C_{org} carbon value from the total carbon value. The $CaCO_3$ weight percent was calculated by multiplying IC carbon by 8.33 [*Lyle et al*., 2000].

$CaCO_3$ was also measured using the UIC Inc. Model CM-5012 CO_2 coulometer attached to Automate FX automatic sample preparation module for $CaCO_3$ analysis. Approximately 15 mg of dried homogenized sediment sample was weighed out, placed into glass vials, and capped. Sample vials were then loaded into the Automate carousel and sample information (i.e. mass and ID) input into the computer program. The system automatically acidified each sample in term and piped the CO_2 to the coulometer. The program monitors the coulometer output and moves to the next sample when there is a

`

0.15% difference between the current and previous reading. Samples were acidified using phosphoric acid (H_3PO_4) and the computer program records %$CaCO_3$ and %C.

Reproducibility and precision were confirmed by analyzing every fourth unknown sample in duplicate and by including two independent standards in each run. For automate analysis, a blank vial was analyzed at the beginning of each run and a "Midway in-house standard" was analyzed as well. For total carbon and inorganic carbon, a blank was run, as well as the Midway standard and reagent-grade sucrose. The "Midway" standard is an homogenized marine sediment from core W8709A-5BC: 5-20 cm, with an average total carbon content of 2.64 + 0.02 wt% and an average C_{org} value of 0.85 + 0.01 wt% [*Piela*, 2010]. In addition, certain samples were randomly selected for reanalysis to confirm initial results.

3.2.2 Biogenic Silica Analytical Method

Biogenic silica (bio-SiO_2 or opal) analyses were completed following methods provided in *Olivarez Lyle and Lyle* [2002], which is a modification of *Mortlock and Froelich* [1989]. *Olivarez Lyle and Lyle* [2002] found that using a 2M sodium carbonate (Na_2CO_3) leach is not sufficient for complete digestion and so concluded that more complete digestion could be achieved using a 2M potassium hydroxide (KOH) solution and allowing the digestion to proceed for between 8.5 to 10 hours. Bio-SiO_2 analysis procedures were further modified for this project to use reagent-grade 1M KOH, following *Piela et al*. [2012], who determined that, after testing, a weaker KOH solution was just as effective in bringing about full sample digestion.

`

Freeze-dried, homogenized sediment samples were weighed and transferred to 50 mL Nalgene centrifuge tubes. 5 mL of DDW was added to wash down the sides of the tubes, followed by 5 mL of 10% hydrogen peroxide (H_2O_2). Samples were then sonicated in two directions for ~10 s to disperse the sediment. Excess water was wiped from the outside of the sample tubes and the tubes were lightly covered in plastic wrap and placed in the fume hood to digest overnight.

The following day, the samples were rinsed to dilute the reagents. The rinse cycle, which was performed twice for each sample, included the following: 1) addition of 20 mL DDW, 2) centrifugation at 3400 revolutions per minute (rpm) for 15 min and, 3) decanting the supernatant. Following the first rinse cycle, a specified volume of supernatant was decanted using a 10.0 mL pipette and the waste was properly disposed. Following the second rinse cycle, the supernatant was decanted to 3 mL, making certain not to draw up any of the sediment. At this point, the sample tubes were lightly covered with foil and placed in a warm (50-60°C) oven overnight. Samples were not allowed to dry fully, as a slurry is required to proceed with the digestion [*Piela et al.*, 2012].

Following digestion, the dissolved SiO_2 was measured following the heteropoly blue method [*Hach*, 1997], during which a Hach Company DR/4000 spectrophotometer with a detection range from 0 to 1.600 ± 0.01 mg/L SiO_2 at a wavelength of 815 nanometers (nm) was utilized. To measure the SiO_2 concentration of unknown samples, 10 mL of DDW was added to the reaction vessel, followed by 50 µL of digested sample. Each sample was pipetted using a fresh pipette tip to prevent cross contamination of the samples. Additional reagents (molybdate 3, citric acid, and amino acid F) were then

`

added following Method 8186 [*Hach*, 1997], and the samples were transferred to glass cells and placed in the spectrophotometer for measurement. The darker blue the sample turned, the greater the SiO_2 content.

Following *Piela et al*. [2012], solutions of DDW, KOH, reagent-grade silica standard, and two in-house marine sediment standards were analyzed with each run to establish blanks and assess the accuracy of the sample run. The in-house standards used included a composite Eocene radiolarian ooze from ODP Site 1219A (IUP 1219A composite) and a Pleistocene diatom ooze from ODP Site 1098 (Boise State University (BSU) Site 1098 composite). Additionally, every fourth sample was run in duplicate to confirm precision and reproducibility.

3.2.3 Elemental Analytical Method

Elemental analysis for Al, Ba, Ca, Fe, Mn, Th, and Ti was completed utilizing high-resolution inductively coupled plasma-mass spectrometry (HR-ICP-MS) on the Element XR at Texas A&M University, following *Piela et al*. [2012]. Approximately 50 mg of sediment was weighed into Teflon Savillex beakers. Included in each set of samples were two standards used to monitor the digestion process and machine calibration: NIST 2702 and SX27553. Total sample digestion was achieved by using a number of strong acids including concentrated trace metal grade percholoric acid ($HClO_4$), 14N nitric acid (HNO_3), and trace metal grade hydrofluoric acid (HF). Weighed samples were placed on a hotplate, 1 mL $HClO_4$ was added to each beaker, and the beakers were heated to ~190-200°C until dense white fumes were produced by the solution. At that point, 1 mL HNO_3 was used to rinse the sides and covers of the beakers

`

and the beakers were lightly covered and allowed to reflux for approximately 1 hour. Following reflux, the covers were carefully removed and 2 mL of HF was added, allowed to fume, and then covered to reflux again for approximately 30 minutes. At this point, if the solution was not clear, an additional 2 mL of HF was added and allowed to reflux again. If the solution was clear, the covers were removed and rinsed with 14N HNO_3, and the beakers were heated until most of the liquid had evaporated. Once a thick, gel-like residue had formed at the bottom of the beaker, 1 mL 14N HNO_3 was added and the solution was transferred to a 50 mL centrifuge tube. The beakers were rinsed thoroughly with milli-Q water and the solution in the centrifuge tube was brought to 50 mL with milli-Q water. Then, the tubes were centrifuged for 10 minutes at 1500 rpm.

At this point, 1 mL of solution was removed from the original centrifuge tube and transferred to another for Al, Ca, Fe, Mn, and Ti analysis. 1000 parts per billion (ppb) of indium (In) was used as an internal standard and 500 μL was added to the new centrifuge tube. Then, 2% HNO_3 was used to bring the solution to 50 mL. To run samples for Ba and Th, 5 mL of the original solution was transferred to a third centrifuge tube and 500 μL of 1000 ppb In was added as an internal standard. 2% HNO_3 was used to bring the solution to 50 mL. These samples were then run on the HR-ICP-MS. Unlike *Piela et al.* [2012], isotope dilution analysis was not used for analysis of Ba and Th in the U1337 sediment samples, rather standard calibration analysis was completed for all elements.

`

Prior to each sample run, the HR-ICP-MS was calibrated using a set of standard solutions from SPEX. Reproducibility was determined by duplicate runs approximately every fourth sample, and multiple reruns of random samples. All geochemical data for U1337 is provided in Table B1 and Table B2 for U1338.

3.3 XRF Data Calibration

XRF NMS data can be relatively easily calibrated to estimated sediment composition by using a small set of check data that spans the typical range of sediment values and correlating the NMS data to those discrete measurements. Calibration of XRF NMS data was accomplished following the methods outlined in *Lyle and Backman* [2013]. The NMS data were calibrated using discrete samples analyzed either shipboard or at Texas A&M University. In general we used discrete geochemical sample data in addition to the shipboard geochemical data, however for TiO_2 and to calculate bio-SiO_2, the shipboard TiO_2 data was not used because most measurements were below the detection limit on the shipboard machine. The first step was to take out any data points where either the NMS or weigh percent (wt%) of the component were equal to 0, unless both the NMS and wt% were equal to 0. The second step was to plot the full data set with NMS on the x-axis and wt% on the y-axis. This was done to identify and eliminate any outliers from the calibration data set.

Approximately ⅔ of the full data set was used as calibration data and the remaining ⅓ was used as a check set. The calibration set was plotted and a best fit curve was fitted through the calibration data set. In most cases there is a linear relationship between NMS and wt% component data, however there were a few instances where the

Michaelis-Menten relationship was more appropriate for calibration purposes. Best fit equations were then applied to the data set and statistics were recorded for the full data set and the check data set. The final step involved applying the best fit equations to the full XRF scan data splices to get a predicted wt% of each sediment component and produce a full downcore record of wt% for each component.

Calibration curves and statistics for U1337 $CaCO_3$ and Fe_2O_3 are found in Figures 8 and 9, respectively. The majority of the data were calibrated using linear calibrations, such as the example provided in Figure 8. Figure 9 is an example of the Michaelis-Menten relationship. The Michaelis-Menten curve was used to calibrate the Fe_2O_3 and MnO data. Calibration figures for the remaining data are provided in Appendix B as Figures B1-14. Fully calibrated data are also provided in Tables B3 (U1335), B4 (U1336), B5 (U1337), and B6 (U1338), also found in Appendix B. For U1335 and U1336, calibrations were only completed on the $CaCO_3$ XRF data. For U1337 and U1338, calibrations were completed on Al_2O_3, $BaSO_4$, $CaCO_3$, Fe_2O_3, MnO, SiO_2, and TiO_2. The majority of U1338 $CaCO_3$ calibration data has previously been published in *Lyle and Backman* [2013], however that data was published using the compressed meters composite depth scale, so they have been replotted for easier comparison with the U1335, U1336, and U1337 $CaCO_3$ on the mcd scale. Additionally, $CaCO_3$ analytical data collected at Texas A&M University during the course of this project are also included to add to the calibration.

A)

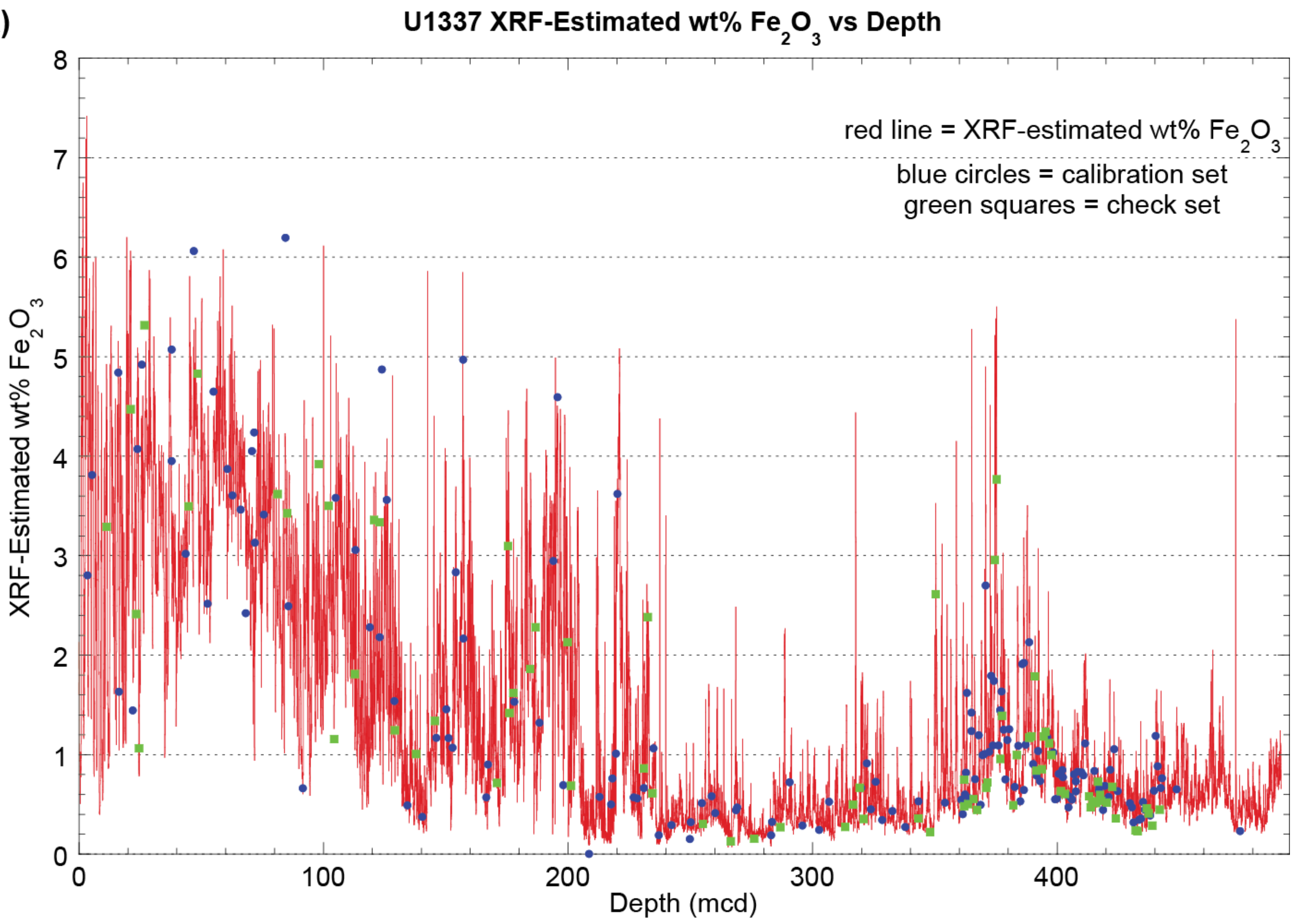

Figure 8 U1337 $CaCO_3$ NMS calibration. Calibration of U1337 $CaCO_3$ NMS using shipboard geochemical data [*Expedition 320/321 Scientists*, 2010c] and discrete samples analyzed post-cruise at Texas A&M University. A) XRF-estimated wt% $CaCO_3$ versus depth with calibration and check data sets included.

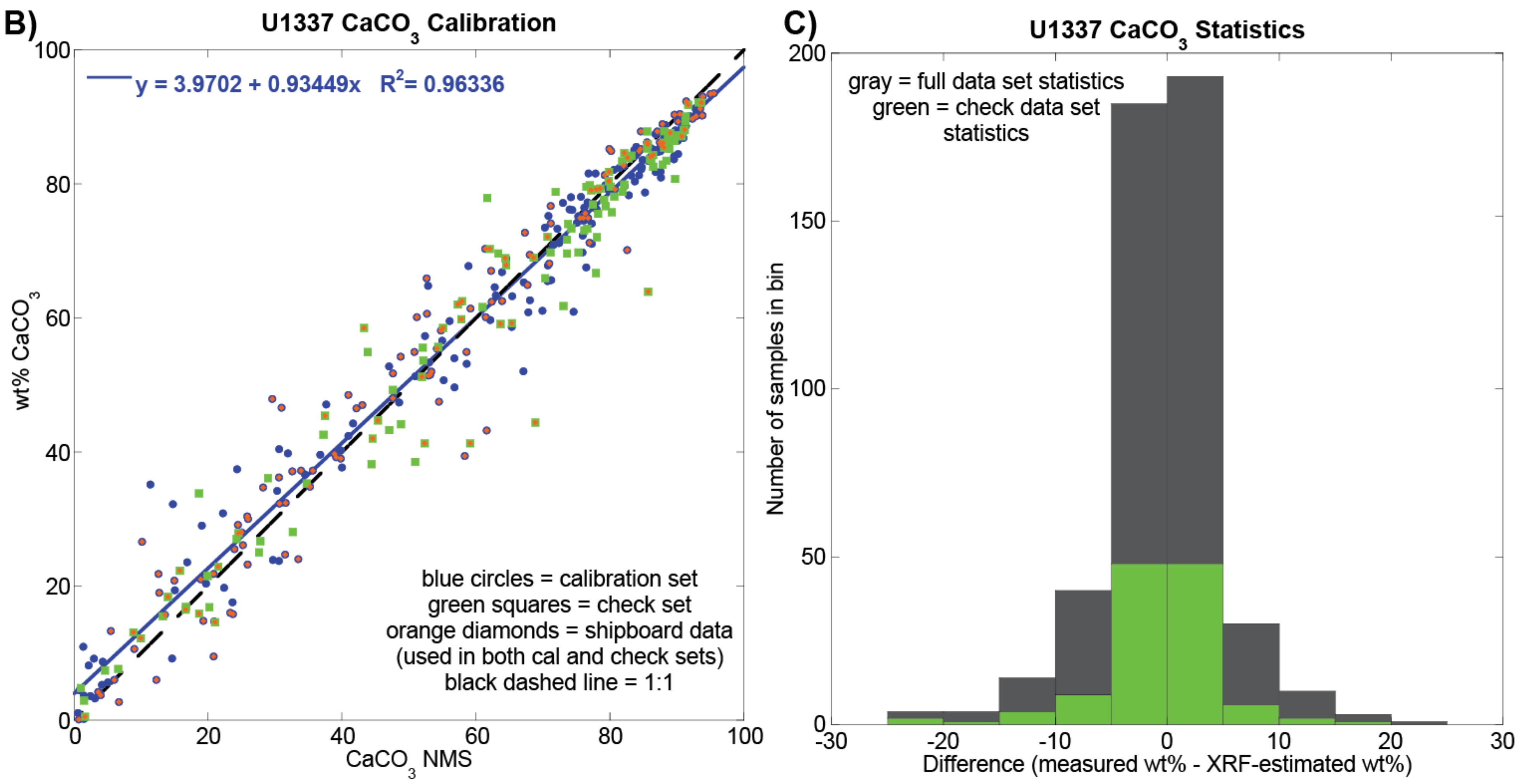

Figure 8 (cont) U1337 $CaCO_3$ NMS calibration (cont).
B) Calibration curve: A total of 363 discrete samples were used, 242 as the calibration set and 121 as the check set. A linear relationship was found between the $CaCO_3$ NMS and wt% $CaCO_3$ data, with a correlation of R^2 = 0.96336. C) Statistics for the full and check data sets.

Measured - Estimated wt% $CaCO_3$		
	Full Data Set	**Check Data Set**
Minimum	-23.919	-23.919
Maximum	20.512	16.297
Sum	-77.346	-77.397
Points	363	121
Mean	-0.213	-0.640
Median	-0.026	-0.454
RMS	5.295	5.524
Std Deviation	5.298	5.509
Variance	28.073	30.353
Std Error	0.278	0.501
Skewness	-0.384	-0.875
Kurtosis	3.236	4.234

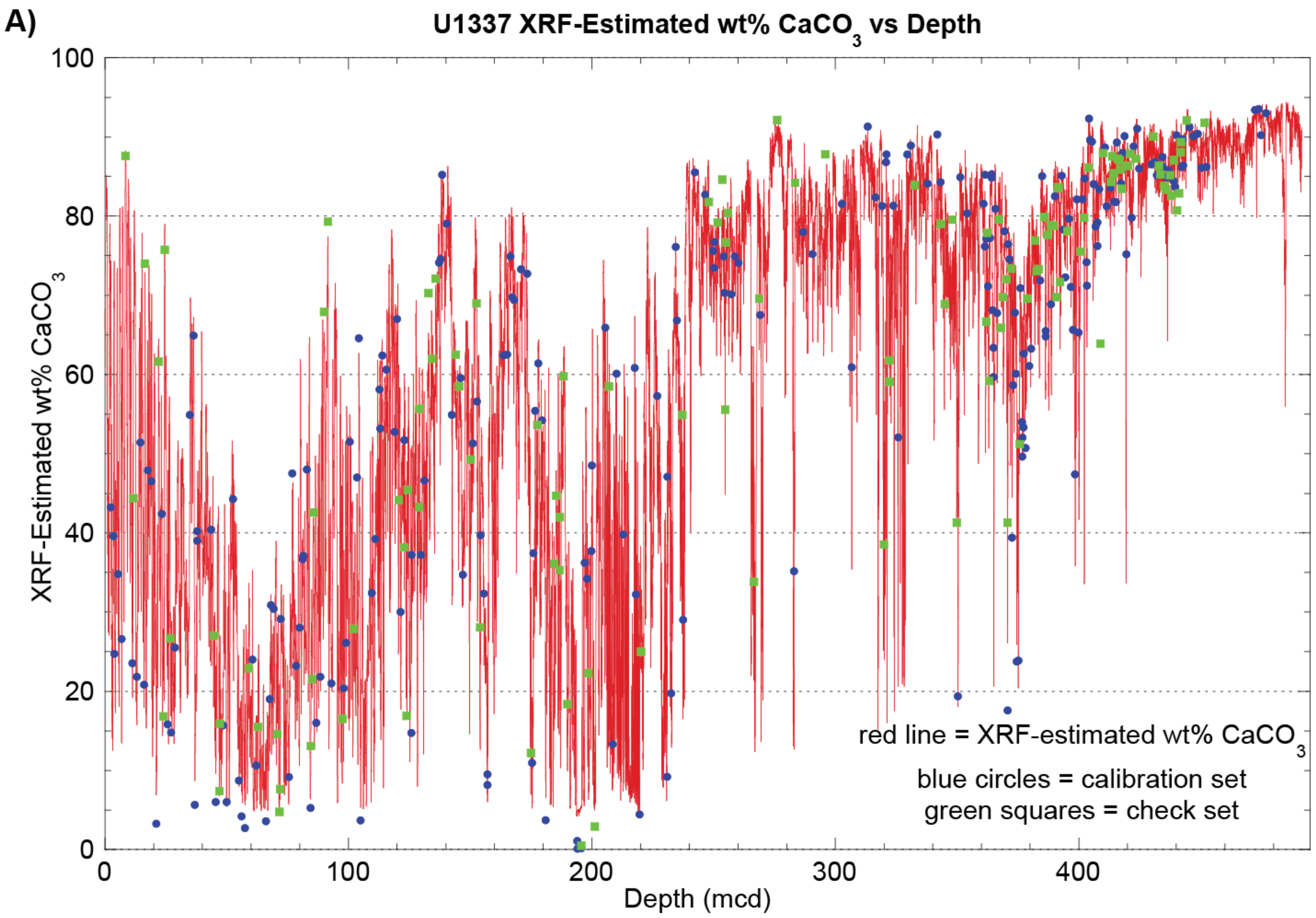

Figure 9 U1337 Fe_2O_3 NMS calibration. Calibration of U1337 Fe_2O_3 NMS data using shipboard geochemical data [*Expedition 320/321 Scientists*, 2010c] and discrete samples analyzed post-cruise at Texas A&M University. A) XRF-estimated wt% Fe_2O_3 versus depth with calibration and check data sets included.

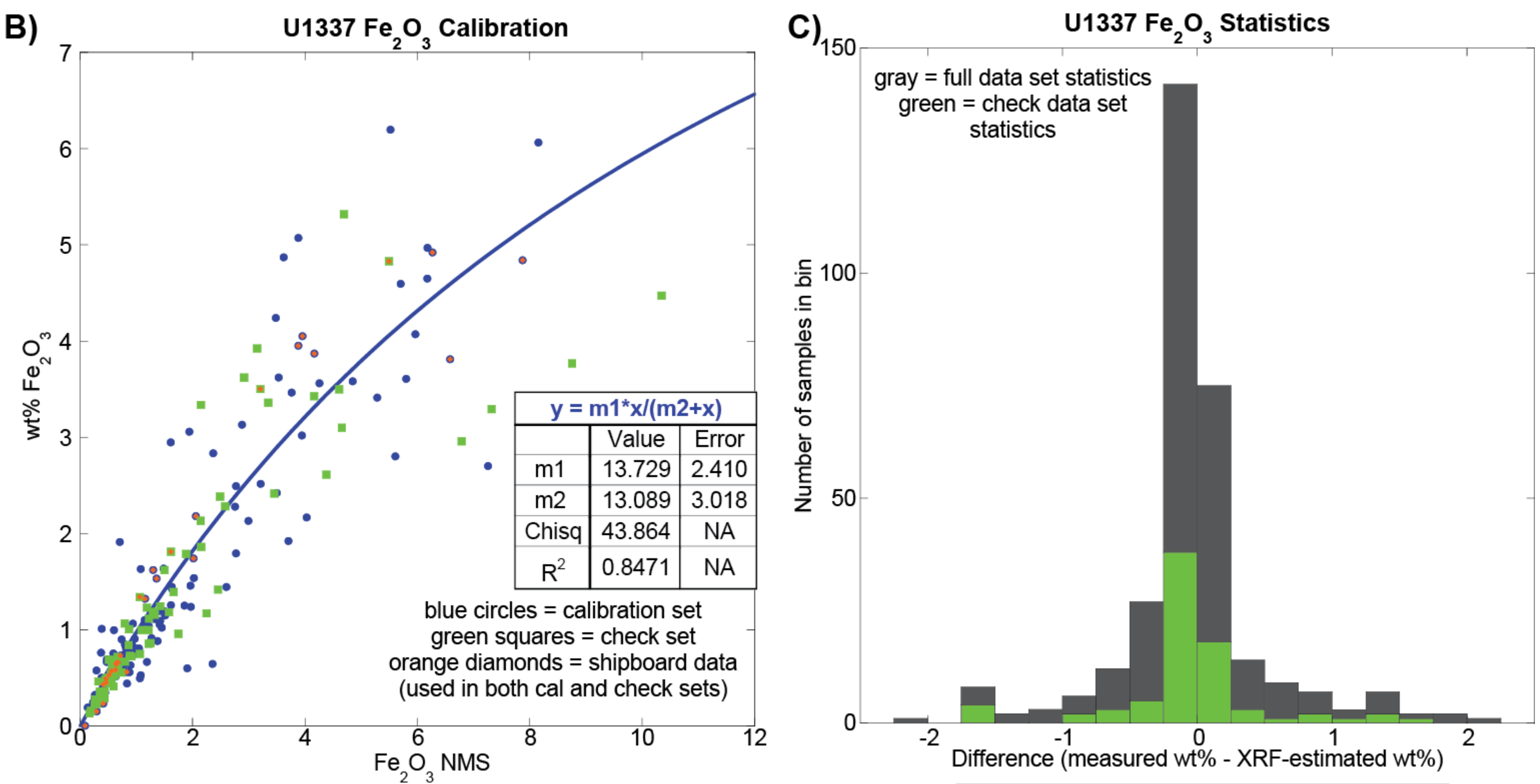

Measured - Estimated wt% $CaCO_3$		
	Full Data Set	**Check Data Set**
Minimum	-2.198	-1.73
Maximum	2.121	1.694
Sum	-6.369	-4.993
Points	241	80
Mean	-0.026	-0.062
Median	-0.044	-0.053
RMS	0.533	0.553
Std Deviation	0.533	0.553
Variance	0.284	0.306
Std Error	0.034	0.062
Skewness	0.287	-0.317
Kurtosis	4.797	3.652

Figure 9 (cont) U1337 Fe_2O_3 NMS calibration (cont). B) Calibration curve: A total of 241 discrete samples were used, 161 as the calibration set and 80 as the check set. The data do not follow a linear trend, rather the Michaelis-Menten equation was used to determine the best fit and predict the wt% Fe_2O_3. C) Statistics for the full and check data sets.

`

CHAPTER IV

EARLY MIOCENE CARBONATE DISSOLUTION IN THE EASTERN EQUATORIAL PACIFIC

4.1 Overview

Because atmospheric CO_2 concentrations are rapidly increasing due to fossil fuel burning, there is a need to understand how atmospheric CO_2 change has affected the global oceans in the past. One way to understand the ocean carbon cycle is to study fluctuations in the $CaCO_3$ content of ocean sediments and determine the nature, timing, and drivers of past climate events. In this chapter, XRF records are used to define an early Miocene low $CaCO_3$ event in the equatorial Pacific that caused a chronostratigraphic seismic horizon termed “Lavender”. The low $CaCO_3$ interval is correlated at submeter scale in 4 drill sites from IODP Expedition 320/321. The 4 drill sites are ~1400 km apart and the horizon has also been identified by seismic reflection a further 500 km to the west. The Lavender seismic horizon covered the entire eastern/central Pacific at the time it was formed. Using multi-element XRF data, we have also determined that the event causing this reflector was caused by $CaCO_3$ dissolution, not a change in bio-SiO_2 production relative to $CaCO_3$, with peak dissolution occurring at 16.9 Ma. The event begins prior to the Miocene Climate Optimum (MCO) but peak dissolution coincides with the initial warming step of the MCO as determined by foraminiferal oxygen isotopes. However, the dissolution does not align with potential CO_2 emission from the emplacement of the Columbia River

`

Basalts. The best model for the cause of this dissolution event is Atlantic-Pacific basin-basin fractionation.

4.2 Introduction

A primary objective of the Integrated Ocean Drilling Program (IODP) Pacific Equatorial Age Transect (PEAT, Expedition 320/321) project was to recover a continuous Cenozoic record of the equatorial Pacific by coring at successive crustal ages above the paleoposition of the Equator [*Pälike et al*., 2010]. Using four drillsites from the IODP PEAT expeditions, we examine the structure and timing of a calcium carbonate ($CaCO_3$) dissolution event that occurred prior to the Miocene Climate Optimum (MCO), at approximately 16.9 Ma. This event was first identified on seismic sections collected as part of DSDP Leg 85. *Mayer et al*. [1986] designated this seismic horizon as "Lavender". This seismic horizon is associated with a major, sharp, early Miocene decrease in $CaCO_3$ and is regionally traceable, seen in cores collected during DSDP Leg 85, ODP Leg 199, and IODP Expedition 320/321, as well as in seismic reflection profiles in the vicinity of 140°W [*Mayer et al*., 1986; *Mitchell et al*., 2003].

`

Seismic data collected during DSDP Leg 85 revealed the presence of a number of regionally traceable reflectors that were identified and assigned color names [*Mayer et al*., 1985; *Mayer et al*., 1986]. The Leg 85 Site 574 data indicate that the major seismic horizons are all associated with a shift or contrast in acoustic impedance resulting from lithologic change. Acoustic impedance is the product of velocity and saturated bulk density, and the relative contribution of each can be examined by plotting both velocity and density against impedance and producing a regression line [Figures 6 and 7 of *Mayer et al*., 1985]. According to *Mayer et al*. [1985] the impedance curve is responding primarily to fluctuations in the saturated bulk density rather than the velocity. Of particular interest is the Lavender reflector, which has subsequently been identified during ODP Leg 199 and IODP Expedition 320/321. *Mayer et al.* [1985] states that this event was unequivocally associated with a sharp decrease in $CaCO_3$ content of the sediment. Variations in $CaCO_3$ content are positively correlated to changes in wet bulk density, so thereby cause acoustic impedance changes and result in seismic reflectors. Figure 10 shows the downcore data from *Mayer et al.* [1986] illustrating the coincidence of a decrease in $CaCO_3$ content and a sharp change in acoustic impedance.

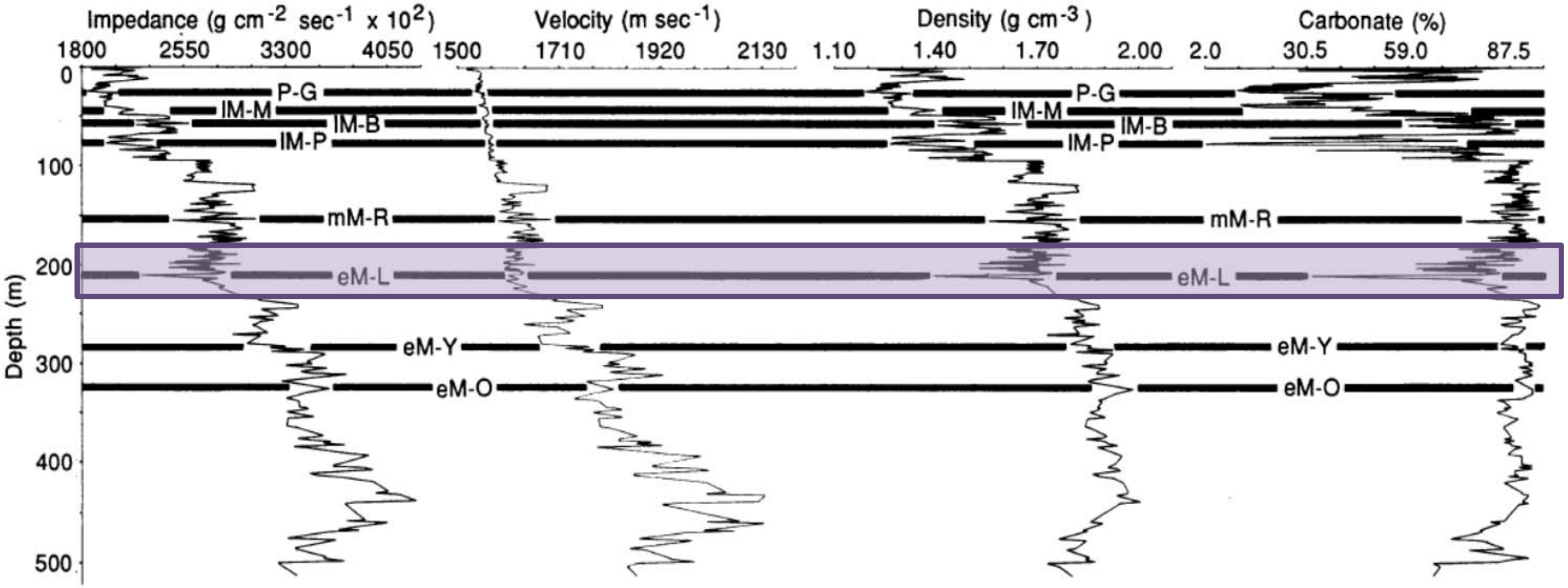

Figure 10 Summary of downhole physical properties at DSDP 574. This figure, modified from *Mayer et al.* [1986] shows the coincidence of a decrease in $CaCO_3$ content and a sharp change in acoustic impedance. The Lavender interval is highlighted.

`

Piela et al. [2012] investigated the interval at Site 574 in more detail and concluded that the decrease in $CaCO_3$ mass accumulation rate (MAR) around 17 Ma, the Lavender event, occurred during the time interval that Site 574 was carried across the equator by Pacific plate motion, when $CaCO_3$ MAR should have been highest. Other biogenic MARs peaked during the equator crossing. *Dubois and Mitchell* [2012] used seismic reflection data from the PEAT site survey to map *Mayer et al*. [1985] seismic to PEAT drilling, and compared the shipboard $CaCO_3$ profiles from Site DSDP 572, DSDP 574, ODP 849, and IODP U1335, U1336, U1337, and U1338, effectively linking Mayer's central equatorial Pacific work to the PEAT work in the EEP. In this chapter, we examine the Lavender interval identified in the cores and seismic data from IODP Expedition 320/321, cores U1335, U1336, U1337, and U1338, in an effort to determine the timing, structure, and potential drivers of the event.

4.3 Materials and Methods

4.3.1 Study Sites

Four individual site locations, U1335, U1336, U1337, and U1338, cored as part of the PEAT expeditions contain the major Neogene sediment sections for the PEAT equatorial Pacific megasplice (Figure 11). These sites are currently located between 7°42'N and 2°30'N, 117°58.2'W and 128°15.2'W, in ~4200 to ~4400 m water depth [*Expedition 320/321 Scientists*, 2010a, 2010b, 2010c, 2010d]. Crustal ages range from ~18 Ma for Site U1338 to ~32 Ma for Site U1336. These locations are ideal for studying the early Neogene, and in particular, the Lavender interval, because the northwestward movement of the Pacific plate prevented older Neogene sediments from being buried too deeply beneath younger sediments and be subject to thermal diagenesis. The latitude change of a site on the Pacific plate is about 0.25° per million years so that drill sites are moved relatively rapidly through the high-productivity, high-sedimentation zone within 2° of the equator [*Pälike et al.*, 2010]. Table C1 provides drilling location, water depth, paleolatitude at 10 Ma and 17 Ma using a fixed hotspot Pacific pole of rotation, and crustal age for each of the four PEAT Neogene sites in this study. Figure 12 shows present site locations with the plate tectonic backtrack to cover the time interval during which the Lavender event occurred. During the Lavender event, all sites except U1336 were within the equatorial high productivity zone, and Site U1337 was closest to the equator (~0.2°N).

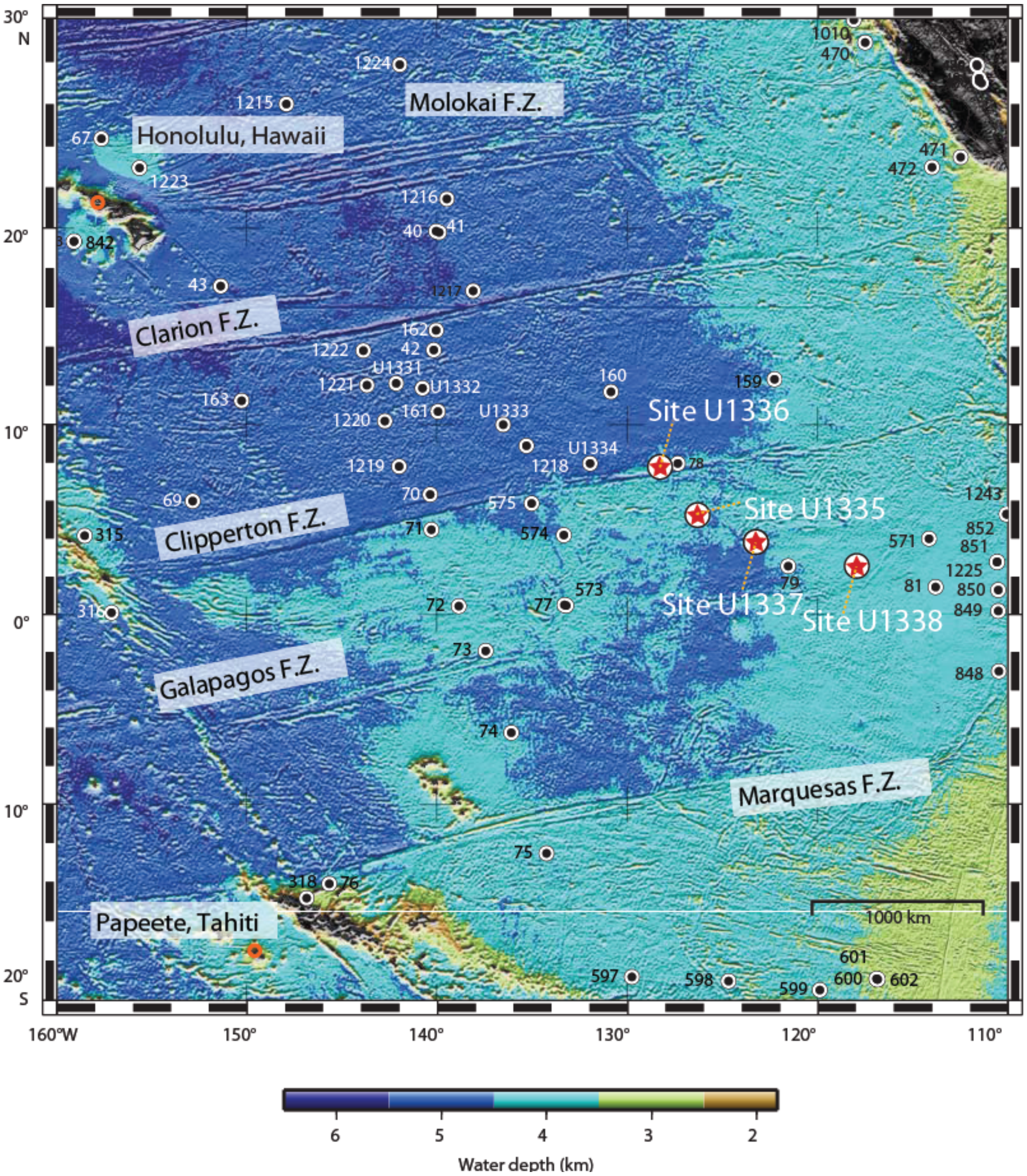

Figure 11 PEAT drilling location site map. Site map includes locations of Sites U1335, U1336, U1337, and U1338 and other PEAT drilling locations. Red stars show the location of Sites U1335, U1336, U1337, and U1338 drilled during IODP Expeditions 320 and 321. Black circles are other sites drilled during IODP, DSDP, and ODP sites. F.Z. indicates a fracture zone. Honolulu, HI and Papeete, Tahiti are indicated for orientation [Modified from *Expedition 320/321 Scientists*, 2010e].

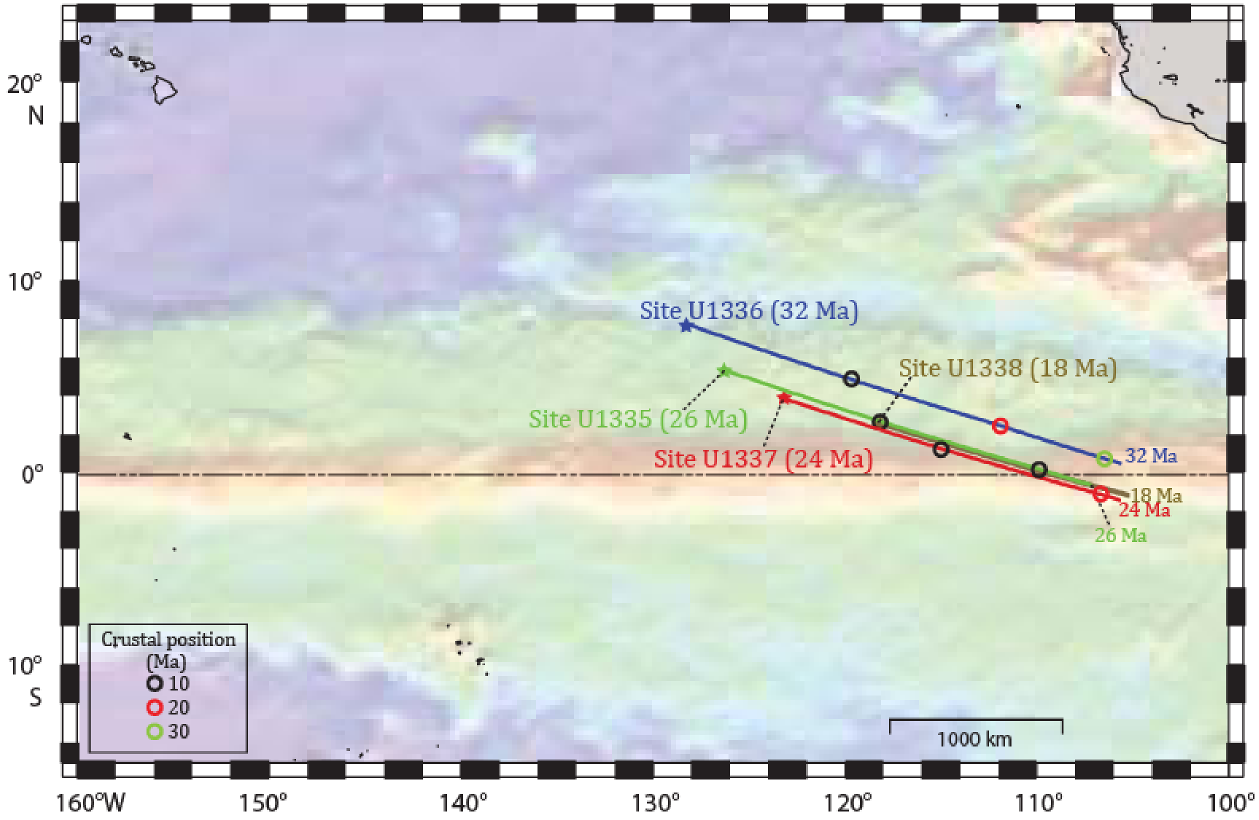

Figure 12 Neogene backtrack. Backtracked positions for PEAT sites (stars), using stage poles from *Koppers et al.* [2001] superimposed on a satellite-derived (GlobColour) map of present ocean chlorophyll-a concentrations (December 2005 mean monthly). Red = high productivity, blue = low productivity. The backtracked positions are noted every 10 m.y. back from present. Estimated basement ages are included for each site while situated at the paleo-ridge crest. [Modified from *Expedition 320/321 Scientists*, 2010e].

`

4.3.2 Bulk Sediment Chemistry Proxies

XRF scanning can be used to study the biogeochemically active elements Ca, Si, and Ba within a sediment core in order to understand changes in primary productivity and biogenic sediment burial. These data can then be compared to changes in preservation to further understand changes in the overall carbon cycle. XRF scanning can also be used to measure aluminosilicate elements including Al, K, and Ti, to better understand the dust input to the region, and to estimate levels of carbonate dissolution. Measuring redox-sensitive elements such as Fe and Mn provides information about the sedimentary redox environment, as well as distal hydrothermal plume deposition near the basement. Using calibrated XRF data, downcore changes in sediment components at the time of the Lavender event can be studied to determine whether the event is indeed a dissolution signal. In addition to calibrated XRF data, we measured four biogenic sediment components on discrete sediment samples, including $CaCO_3$, organic carbon (C_{org}), bio-SiO_2, and bio-Ba, as well as Al, Ca, Ti, Fe, Mn, and Th, on the U1337 splice.

Approximately 30% of the particulate Ba flux is buried in the sediments, making it a better proxy for exported C_{org} rain than bio-SiO_2, of which only 2 to 12% of the particulate flux is preserved in equatorial Pacific sediment [*Dymond et al*., 1992; *Dymond and Collier*, 1996; *Piela et al*., 2012]. As with Site 574 [*Piela et al*., 2012; *Mayer et al*., 1985], Site U1337 is far from terrigenous input and therefore, the Ba measured is primarily biogenic.

The TiO_2 content of the sediment measured by XRF is used as a measure of clay, since the XRF measurement of Ti is better than that of Al. Al, being a light element, has

`

a low energy characteristic fluorescence that is more readily absorbed by air. It is also more appropriate to use Ti as a measure of aluminosilicates within the sediments because significant Al can be bound to bio-SiO_2 so as to cause a significant Al signal [*Murray and Leinen*, 1996; *Dymond et al*, 1997]. This is especially important at intervals where bio-SiO_2 was initially deposited at the seafloor and then experienced early diagenesis and was partially dissolved, leaving the particle-reactive Al behind [*Dymond et al.*, 1997].

In this chapter we will use several ratios to help determine whether we observe dissolution of $CaCO_3$ or dilution by a bio-SiO_2 production event in our sediment cores. The ratio of Si/Ti has proven useful to locate intervals with high opal deposition [*Holbourn et al.*, 2014] rather than intervals with high opal contents because of $CaCO_3$ dissolution. Ca/Ba is useful for identifying intervals of increased or decreased $CaCO_3$ preservation. In the equatorial Pacific, both $CaCO_3$ and Ba particulate rain are correlated with C_{org} particulate rain, [*Dymond and Collier*, 1996; *Piela et al.*, 2012], but Ba is better and more constantly preserved in the sediments [*Dymond et al.*, 1992]. In the PEAT cores, the records of $BaSO_4$ and SiO_2 covary as both are almost completely biogenic, however the record of $CaCO_3$ shows intervals where it decreases separately from the other biogenic components. When the ratio of Ca/Ba is high, carbonate preservation is high. When the ratio is low, dissolution is increased.

4.3.3 Methods

Below is a brief summary of methods used for XRF data acquisition, processing, and calibration with bulk sediment chemical data.

`

4.3.3.1 XRF Scanning

XRF scanning is a rapid, nondestructive method to measure bulk sediment composition. When the data were calibrated, high-resolution profiles of chemical composition over long time frames are produced since the depth resolution of the XRF data is much finer than that of discrete sampling and the time that is needed for scanning each core is relatively short. A detailed description of the XRF scanning procedure [*Shackford et al*., 2014] and data can be found in Chapter 3.

XRF scan data were reduced to normalized median-scaled (NMS) data for U1335, U1336, and U1337 [*Shackford et al*., 2014], and U1338 [*Lyle et al*., 2012] and subsequently calibrated by chemical analysis of discrete samples from each drill site. The XRF data acquisition is similar in all cases. Archive halves of cores along the sediment splice were scraped, covered with thin plastic film and subjected to high-energy X-rays using an Avaatech 3rd generation scanning XRF (odases.tamu.edu/research-facilities/xrf-request/). Measurements were typically made every 2.5 cm and the energy spectrum of fluoresced X-rays was collected using a 2048 channel multichannel analyzer. The raw data were scaled using the median peak area to represent a model median sediment composition and then normalized so that the measured components totaled to 100% of the sample [*Lyle et al*., 2012]. XRF data were collected for the elements Al, Si, K, Ca, Ti, Mn, Fe, using a 10 kV tube voltage and Ba using a 50 kV tube voltage.

`

4.3.3.2 Chemical Analysis of Discrete Samples from U1337 and U1338

Data calibration was accomplished by correlating NMS data to discrete measurements from each drillsite. Calibration samples were chosen based on the variation of XRF data downcore to maximize the range of elemental variability, and bulk sediment composition of the calibration samples were measured by HR-ICP-MS. Correlations between NMS and bulk sediment weight percent (wt %) from HR-ICP-MS analysis were then used to derive a calibration relationship.

Calibration of XRF NMS data was accomplished following the methods outlined in *Lyle and Backman* [2013]. The NMS data were calibrated using discrete samples analyzed either shipboard or post-cruise at Texas A&M University. In general we used discrete geochemical sample data in addition to the shipboard geochemical data, however for TiO_2 and to calculate bio-SiO_2, the shipboard TiO_2 data was not used because the majority of measurements were below the shipboard detection limit. Geochemical data for U1337 and U1338 are included in Appendix B as Tables B1 and B2, respectively. The shipboard data is not included on those tables. Since U1335 and U1336 $CaCO_3$ was calibrated using shipboard data only, that data has not been included but is available in *Expedition 320/321 Scientists* [2010a; 2010b]. The first step was to take out any data points where either the NMS or wt% of the component were equal to 0, unless both the NMS and wt% were equal to 0. The second step was to plot the full data set as wt% versus NMS in order to identify and eliminate any outliers from the calibration data set.

`

Because the high-purity acid used in the ICP-MS analysis was contaminated with Si, the Si calibration was achieved by measurements of biogenic SiO_2 on each of the samples, and summed with an estimated clay-bound SiO_2 calculated from the XRF-estimated TiO_2 wt% and the Si/Ti ratio of upper continental crust [*Taylor and McLennon*, 1995].

For the U1337 and U1338 splices, XRF data were calibrated for all sedimentary components (i.e., Al_2O_3, $BaSO_4$, $CaCO_3$, Fe_2O_3, MnO, SiO_2, TiO_2, and bio-SiO_2). Geochemical analyses were completed on 225 discrete samples collected from the U1337 splice and were used to calibrate the XRF data from U1337. These samples were selected and obtained from the IODP Gulf Coast Repository. Samples were analyzed for IC, $CaCO_3$, C_{org} using a UIC coulometer as described in *Piela et al*. [2012], bio-SiO_2 using the sediment digestion described in *Olivarez Lyle and Lyle* [2002], and elemental concentration of Al, Ba, Ca, Fe, Mn, Th, and Ti by HR-ICP-MS after digestion in Teflon beakers using hot perchloric acid/nitric acid as described in *Piela et al*. [2012] and in Chapter 3 of this manuscript.

Approximately ⅔ of the full data set was used as calibration data and the remaining ⅓ was used as a check set. The calibration set was plotted and a best fit curve was fitted through the calibration data set. In most cases there is a linear relationship between NMS and wt% component data, however there were a few instances where the Michaelis-Menten relationship was more appropriate for calibration purposes. Best fit equations were then applied to the data set and statistics recorded for the full data set and the check data set. For the final step, we applied the best-fit equations to the full XRF

`

scan data splices to get an estimated wt% of each sediment component and produced a full downcore record of wt% for each component. $CaCO_3$ calibration for the U1337 splice included both shipboard and post-cruise analytical data. Calibrated $CaCO_3$ data from U1338 has been previously published by *Lyle and Backman* [2013].

4.3.3.3 $CaCO_3$ Calibration of XRF Scan Data, Sites U1335 and U1336

Although HR-ICP-MS analyses were not done for Sites U1335 and U1336, sufficient data exists from shipboard analyses to calibrate the $CaCO_3$. The uncalibrated NMS data for other elements are adequate to distinguish trends in the other elemental data, although absolute values are not well constrained. Data were calibrated for $CaCO_3$ using shipboard data only in cores U1335 and U1336 because we did not measure additional $CaCO_3$ values. The shipboard $CaCO_3$ data sets are more than adequate to define the $CaCO_3$ profiles at U1335 and U1336 since 1 sample every section (~1.5 m) was measured at both sites [*Expedition 320/321 Scientists,* 2010a; 2010b]. Estimated error of the calibrations for U1335 and U1336 $CaCO_3$ are 0.297 and 0.295, respectively. Profiles of the $CaCO_3$ data can be seen in Figure 13. Discrete bulk sediment compositional analyses are ultimately needed to calibrate the other XRF scan elements from U1335 and U1336.

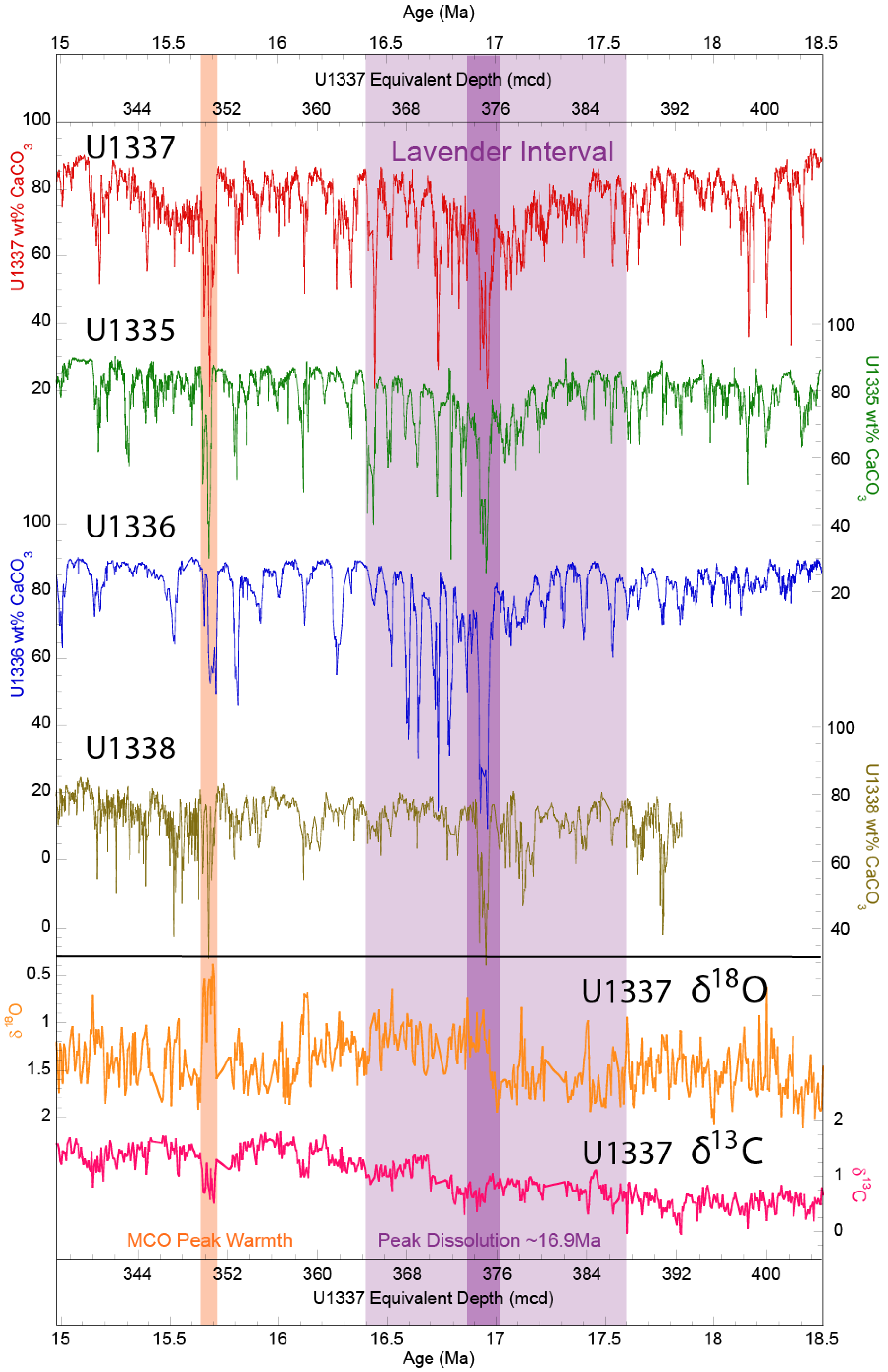

Figure 13 Neogene PEAT site $CaCO_3$. XRF-estimated wt% $CaCO_3$ for the PEAT sites: U1337 (red), U1335 (green), U1336 (blue), and U1338 (brown). Also shown are the benthic foraminiferal $\delta^{18}O$ (orange) and δ13C (pink). Peak Miocene Climate Optimum (MCO) warmth is highlighted [*Holbourn et al.*, 2014], as are the Lavender Dissolution Interval and Lavender peak dissolution.

`

4.3.4 Lavender Interval Splices and Age Model

4.3.4.1 Lavender Interval Splices

In order to more closely examine the Lavender event across multiple PEAT cores, cores were plotted in U1337 equivalent depth and then the U1337 age model was applied to all four cores. The complete $CaCO_3$ wt% data sets with ages and equivalent depths for 15 to 18.5 Ma are provided in Appendix B (Tables B3 through B6 and C2). Magneto- and biostratigraphic chronostratigraphy [*Ohneiser et al*., 2013; *Expedition 320/321 Scientists*, 2010c] were used to coarsely align the Lavender event in the four cores and AnalySeries 2.0 software [*Paillard et al*., 1996] was used to correlate the $CaCO_3$ profiles and to assign U1337 equivalent depths to all sites. We chose to use the U1337 depth since the Lavender event is well defined in that core and stable oxygen and carbon isotope data are available over the event time interval, to better constrain the actual age of the event. All original depths used in this manuscript for Sites U1336, U1337, and U1338 are the revised composite depths from *Wilkens et al.* [2013] and are in meters composite depth (mcd, using the CCSF-A method). Site U1335 uses the original composite depths (also in mcd) from *Expedition 320/321 Scientists* [2010a] since the splice was not adjusted post-cruise.

4.3.4.2 Lavender Interval Age Model

An orbitally tuned age model for the interval between 15 and 18.5 Ma has been developed by combining $\delta^{18}O$ data from Holbourn [*unpublished data*] and *Tian et al.* [2013]. Following *Holbourn et al.* [2014], the $\delta^{18}O$ and $\delta^{13}C$ in the epifaunal benthic foraminifers *Planulina wuellerstorfi* or *Cibicidoides mundulus* were measured in ~5-10

`

cm intervals. The new chronology was created using the shipboard stratigraphy and correlating the benthic foraminiferal $\delta^{18}O$ data to the computed variations of the Earth's orbit of *Laskar et al*. [2004] [*Holbourn et al*., 2014]. The tuning target was constructed using an eccentricity-tilt-precession composite with no phase shift and with equal weight eccentricity and obliquity and only ⅓ precession. The $\delta^{18}O$ minima were correlated to the eccentricity-tilt-precession maxima following a minimal tuning approach to preserve original spectral characteristics.

The published ages assigned by *Tian et al*. [2013] and Holbourn [*unpublished data*] disagreed but were adjusted by applying the Holbourn age model [*unpublished data*] to the *Tian et al*. [2013] data. Ages assigned in the supplementary material for the interval 15 to 18.5 Ma (Table C2) are based on the stable isotope age model developed following the methods described in *Holbourn et al*. [2007] and *Holbourn et al.* [2014]. The data from the upper part of the MCO, from *Tian et al*. [2013], have been adjusted to align in age with the ages on the unpublished Holbourn data using the Ager function of the ARAND software package [*Howell et al*., 2006]. The application of this age model to the *Tian et al.* [2013] data does not significantly change the previously assigned ages [*Tian et al.*, 2013].

As we do not have $\delta^{18}O$ data for the entire U1337 core, we applied the combined Holbourn-Tian age model to the core data, using the Ager function of the ARAND software package [*Howell et al.*, 2006]. This age model was also applied to the U1335, U1336, and U1338 cores in U1337 equivalent depth.

`

4.3.4.3 Comparison with Previously Published Magnetostratigraphic Age Model

The isotope age model used in this paper does not agree with the paleomagnetic age model defined by *Ohneiser et al*. [2013] for U1336 applied to the well-constrained Miocene paleomagnetic stratigraphy from that site. The lack of agreement, approximately 100,000 yr points to additional study that needs to be done to link the different chronostratrigraphies.

Ohneiser et al. [2013] reported on the upper ~85m at Site U1336, which contain stable magnetization spanning the early to middle Miocene (~19-13 Ma). Ages were assigned to magnetic reversals using the geomagnetic polarity time scale (GPTS) [*Ohneiser et al*., 2013; ATNTS2004, *Lourens et al*., 2004]. The U1336 magnetostratigraphy was developed by mapping paleomagnetic reversals for each core within the splice to chron assignments guided by first and last occurrence datums of microfossils from *Expedition 320/321 Scientists* [2010b] and could be correlated to the ATNTS2004 GPTS with confidence to the top of Chron C5Br or ~ 15.2 Ma. Below this, the astronomical calibration of *Billups et al*. [2004] was used [*Ohneiser et al*., 2013]. We observe a good match between the U1337-extrapolated age model up to about 15.5 Ma, however older sections show a mismatch.

Using either age model, the Lavender interval at Site U1336 is within Chron C5Cr, which covers the time period between 16.5 and 17 Ma following *Billups et al*. [2004]. However ages of paleomagnetic reversals in the early Miocene are not very well known. U1336 was correlated to U1337 primarily using first and last occurrences of microfossils found within the core catcher samples because magnetic data is only

`

available for U1337 to C4Ar/C5n (~9.78 Ma) in U1337 [*Expedition 320/321 Scientists*, 2010c] whereas U1336 begins with C5r.3r/C5An.1n (~12.0 Ma) [*Expedition 320/321 Scientists,* 2010b; *Ohneiser et al*., 2013]. Figure 14 shows the wt% $CaCO_3$ for both U1337 (red) and U1336 (blue) plotted on the U1337 age model. Also shown (blue dashed) is that same U1336 wt% $CaCO_3$ data plotted using the *Ohneiser et al*. [2013] age model. There is a significant offset in terms of the age of the Lavender event minimum using the *Ohneiser et al*. [2013] age model which results in the event plotting as approximately 100 ky younger than the stable isotope model. Potentially, the $CaCO_3$ correlation along with the paleomagnetic stratigraphy of *Ohneiser et al*. [2013] can be combined to refine the early Miocene paleomagnetic chronostratigraphy.

U1335 was correlated to U1337 using both magneto- and biostratigraphic data from the Expedition Proceedings [*Expedition 320/321 Scientists*, 2010a]. Where possible the same correlation tie points were used to tie multiple cores to U1337 (Table C3).

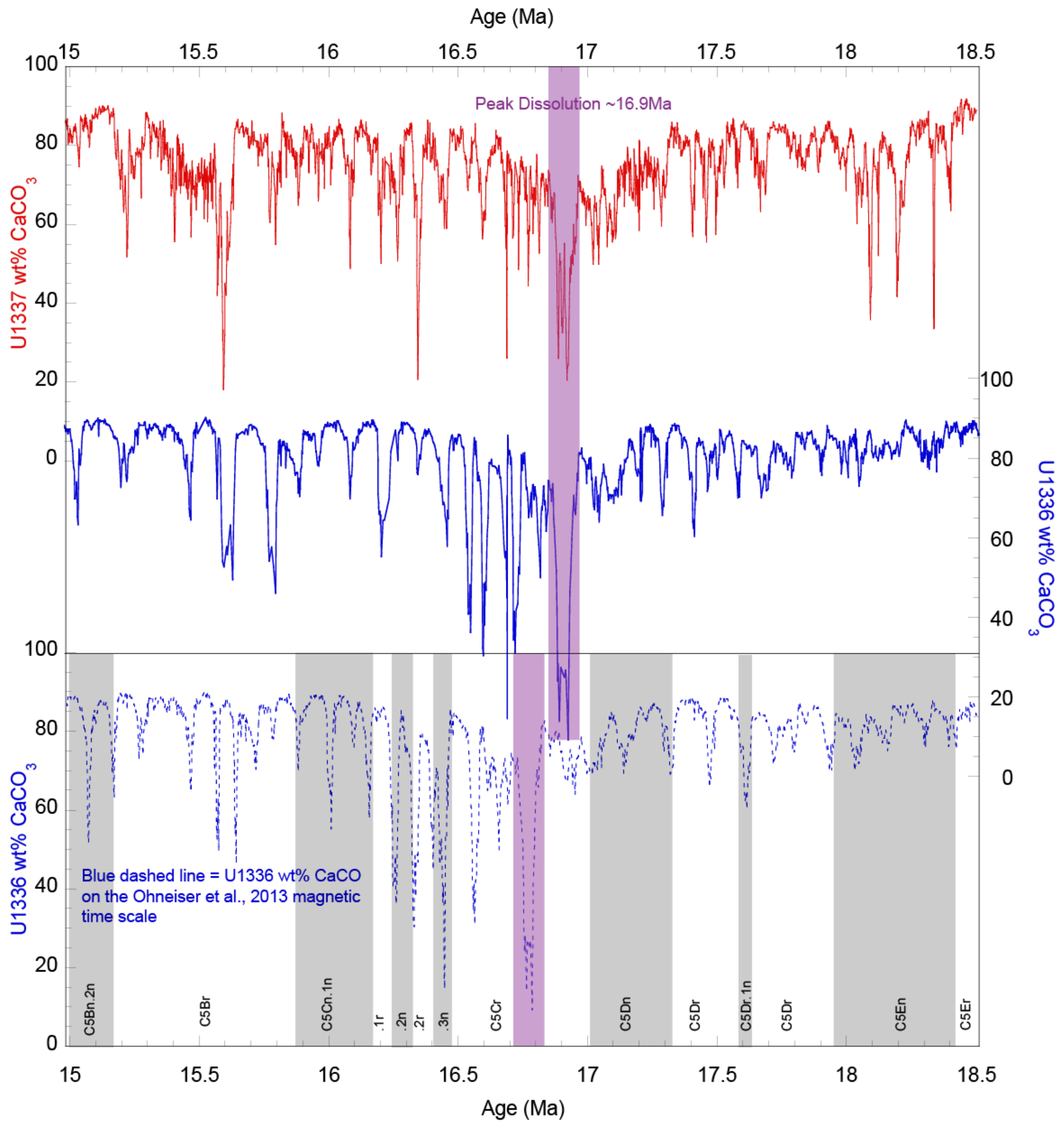

Figure 14 Age model comparison. The wt% CaCO$_3$ for both U1337 (red) and U1336 (blue) are plotted on the U1337 age model. The U1336 wt% CaCO$_3$ is also plotted as a blue dashed line plotted using the *Ohneiser et al.* [2013] age model. There is a significant offset in terms of the age of the Lavender event minimum using the *Ohneiser et al.* [2013] age model which results in the event plotting as approximately 100 ky younger than the stable isotope model.

`

4.4 Results

4.4.1 Expression of the Lavender Event at Different Drill Sites in the Equatorial Pacific

The sedimentary expression of the Lavender seismic horizon is found at multiple drill sites from DSDP Leg 85 [*Mayer et al*., 1986] and in the Neogene Expedition 320/321 drill sites [*Lyle et al*., 2010]. The Lavender event is not found in ODP Leg 138 sites because the crust that they were located on is too young—the age of the Lavender event from *Mayer et al*. [1986] is ~17 Ma and the majority of Leg 138 drilling was situated on 10-11 Ma basalt crust.

Figure 13 shows the XRF-estimated wt% $CaCO_3$ over the Lavender interval (and the basal part of the MCO) for Sites U1335-U1338, plotted in U1337 equivalent depth and approximate interpolated age. The ages are assigned using an initial age and a linear sedimentation rate over the depth interval shown so that age as well as time could be plotted. The more precise ages are in Table C2, and the age-depth model is shown in Figure 15. Ages shown on Figure 13 are approximate but since the model sedimentation rate, ~25 m/m.y is nearly matched by the linear approximation between 15 to 18.5 Ma (Figure 14), the ages in this interval need little correction.

`

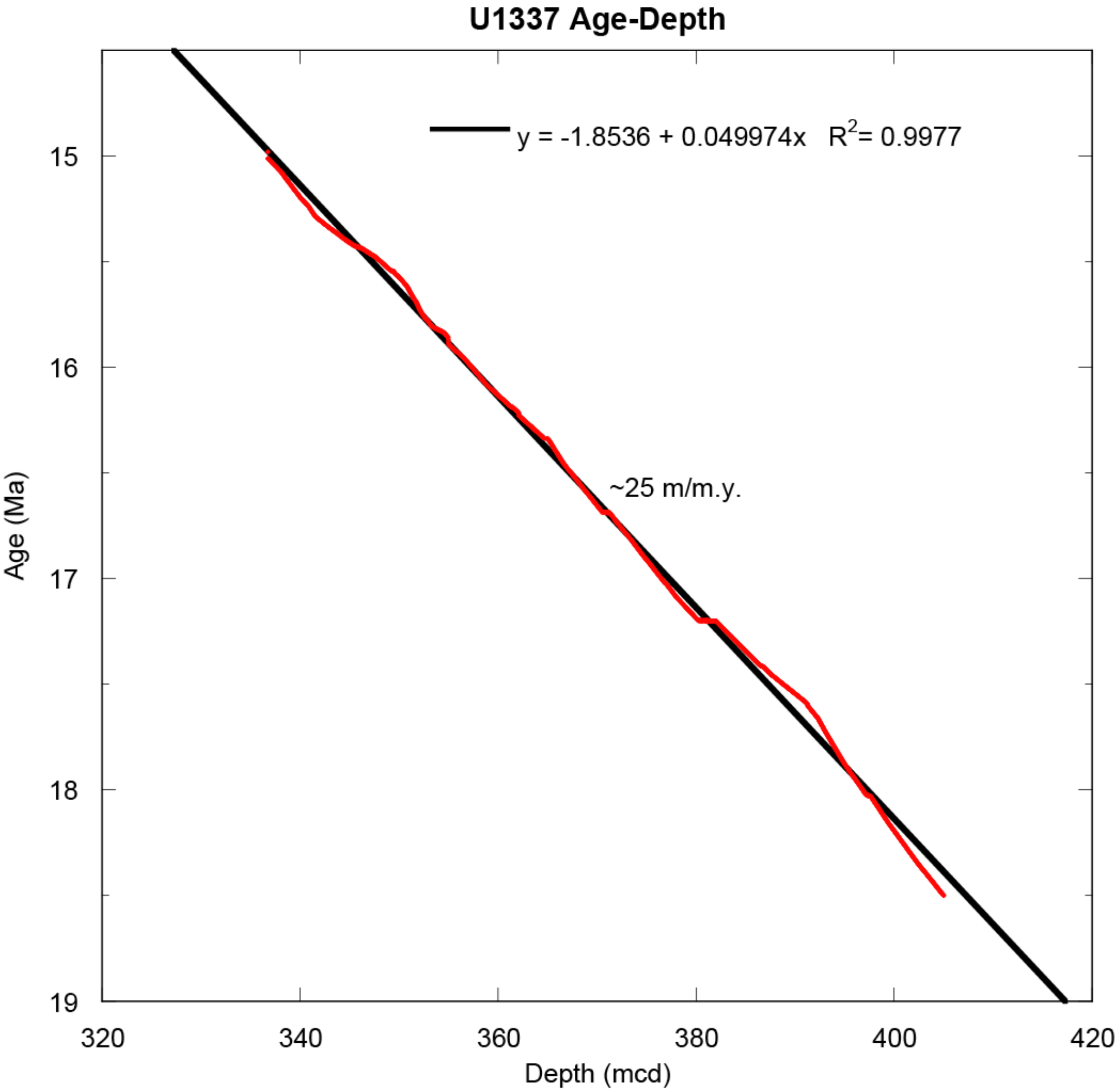

Figure 15 U1337 Age-Depth plot. Age-depth plot based on benthic foraminiferal δ^{18}O indicates almost linear sedimentation (~25 m/m.y.) during the time interval of interest.

`

4.4.2 The $CaCO_3$ Expression of the Lavender Interval

We define the Lavender interval to be from 17.6 Ma to 16.4 Ma. The Lavender interval began about 17.6 Ma with a gradual decrease in $CaCO_3$ accompanied by orbitally-driven low $CaCO_3$ transients, culminating at 16.9 Ma with a sharp $CaCO_3$ minimum (~30% $CaCO_3$ in U1337). $CaCO_3$ then gradually recovered, with more orbital cyclicity, from an average low near 60% in U1337 back to more typical values of 80% at about 16.4 Ma. Thus, the total span of the Lavender interval is about 1.2 million years.

The Lavender event is most poorly defined in Site U1338 compared to the other records since the interval is in the basal sediment section, i.e. within 30 m of the base of the core. Hydrothermal sedimentation adds additional variability and there can also be minor to significant thermal diagenesis [*Moore*, 2008]. Also, the splice is ambiguous within this interval. That said, *Holbourn et al*. [2014] has previously defined the 15.5 Ma peak warming event in U1338 from benthic isotope data between 423.6 and 425.0 mcd, to match the stable isotope data for U1337, so the tie point at 15.5 Ma between U1338 and U1337 is well-constrained.

4.4.3 Stable Isotopes Across the MCO and Lavender Interval

The benthic foraminiferal $\delta^{13}C$ and $\delta^{18}O$ data for site U1337 are shown at the base of Figure 13 from *Tian et al*. [2013] and *Holbourn* [unpublished] for the Lavender interval and the basal part of the MCO. Table C3 provides the original magneto- and bio-chronostratigraphic tie points used in the initial correlation. The low $CaCO_3$ transient at 15.5 Ma associated with peak warming of the MCO has been more extensively studied and therefore was used as a way to constrain the depths and ages of our correlation

`

[*Holbourn et al.*, 2014]. The low $CaCO_3$ transient associated with the 15.5 Ma event is clearly visible in all four of our Neogene PEAT cores in Figure 13.

U1337 is one of the few drill sites in which both stable isotope data and high-resolution elemental data cover the entire MCO. Published data from Site 1237, on the Nazca Ridge in the eastern Pacific, only has data younger than 16.5 Ma [*Holbourn et al.*, 2005]. Figure 16 shows the MCO defined in U1337. The MCO begins with an abrupt apparent warming at 16.9 Ma (374.8 mcd in U1337) marked by a 0.7‰ decrease in $\delta^{18}O$ and the minimum Lavender event $CaCO_3$ transient. The MCO ends with a 0.9‰ $\delta^{18}O$ increase beginning at 13.9 Ma [317.7 mcd; *Tian et al.*, 2013]. There is variable $CaCO_3$ throughout the interval, with $CaCO_3$ minima matching with $\delta^{18}O$ minima but average $CaCO_3$ is higher than is found in the Lavender event. The low $CaCO_3$ low $\delta^{18}O$ transients suggest a CO_2 feedback from warming that transfers CO_2 from terrestrial reservoirs into the oceans.

The middle Miocene climate transition that ends the MCO is marked by diatom production events that also dilute $CaCO_3$ at Site U1337, similar to what was found at Site U1338 [*Holbourn et al.*, 2014]. Average $CaCO_3$ through this interval is significantly higher than during the Lavender interval, but the $CaCO_3$ variability near the top of the MCO defines another of the *Mayer et al.* [1986] seismic horizons, the ‘Red’ horizon at 13.5-15 Ma [*Dubois and Mitchell*, 2012].

`

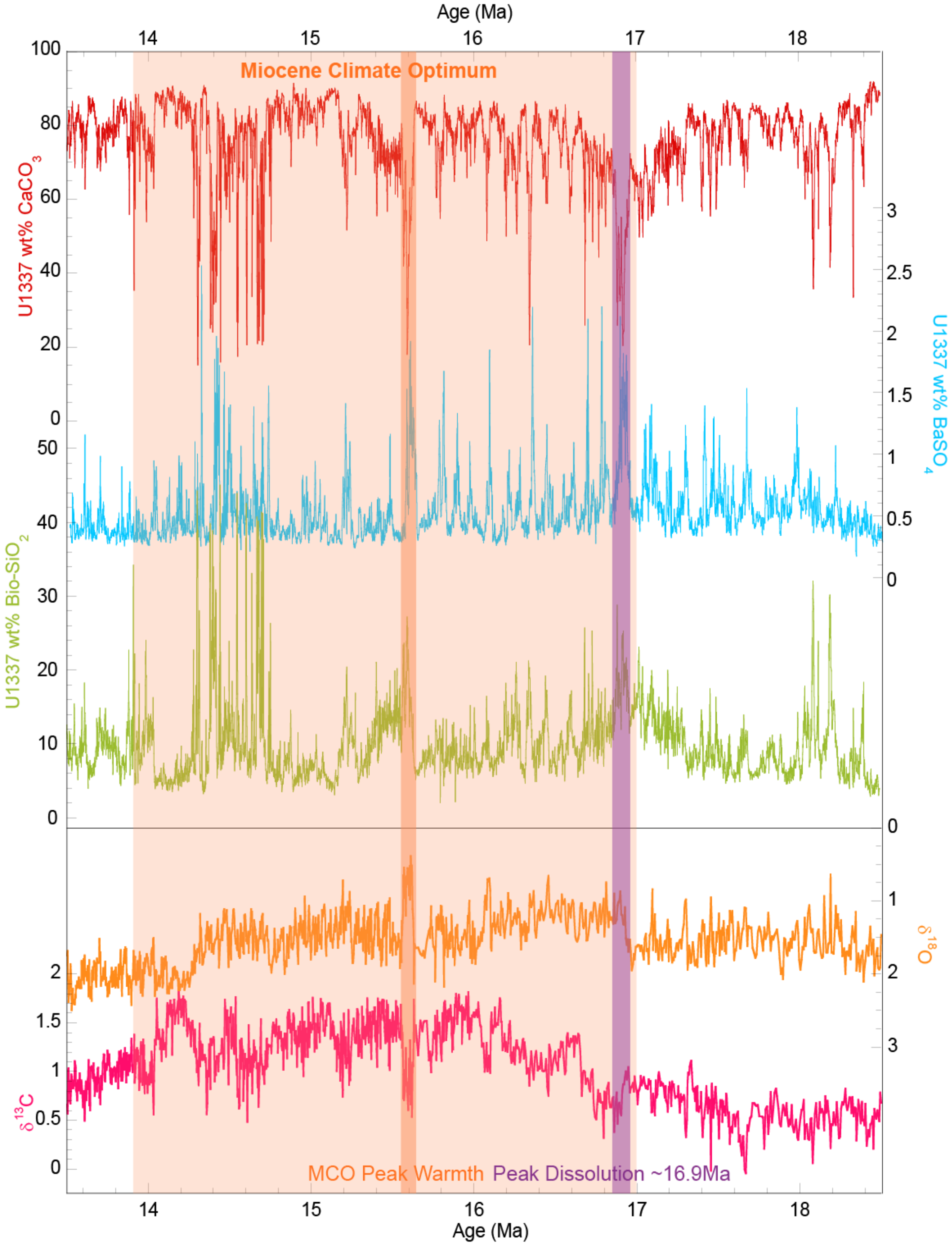

Figure 16 U1337 data over the MCO. U1337 wt% $CaCO_3$ (red), $BaSO_4$ (light blue), and bio-SiO_2 (green) plotted by age from 13.5 to 18.5 Ma. Also shown are benthic foraminiferal $\delta^{18}O$ (orange) and δ13C (pink). The data covers the entirety of the MCO. MCO peak warmth and the Lavender interval peak dissolution are both highlighted.

`

4.5 Discussion

4.5.1 Dissolution Origin of Lavender Event

In the equatorial Pacific low $CaCO_3$ intervals can be caused by either loss of $CaCO_3$ from sediments by dissolution, dilution of $CaCO_3$ by bio-SiO_2, or a combination of the two processes. A low $CaCO_3$ interval caused by dissolution originates from a change in the carbon cycle and how carbon is stored in the deep ocean. An increase in the biological pump and/or a decrease in $CaCO_3/C_{org}$ of particulate rain can lower deep $[CO_3^{2-}]$ and increase $CaCO_3$ dissolution [*Pälike et al.*, 2012]. $CaCO_3$ dissolution can also increase in combination with an increase in CO_2 degassing from the crust or mantle that is not matched by additional continental weathering [*Pälike et al.*, 2012]. Finally, regional dissolution in the equatorial Pacific can be caused by increased $CaCO_3$ deposition in other marine areas, either in different basins or in shallow marine environments [*Opdyke and Wilkinson*, 1988; *Berger*, 1970].

In contrast, low $CaCO_3$ content caused by bio-SiO_2 dilution implies high primary productivity resulting from elevated cycling of nutrients to surface waters from the shallow subsurface. High productivity also affects the carbon cycle through a strengthened biological pump. It is important, from the carbon cycle point of view, to understand whether an individual low $CaCO_3$ interval is driven primarily by high productivity or high dissolution. *Piela et al.* [2012] suggested that the Lavender event at Site 574 was a $CaCO_3$ dissolution interval. If this is true, it must be regional in nature because of the extent of the seismic horizon, and it should also be a dissolution interval in the PEAT cores, especially in U1337.

In order to determine whether the Lavender event was in fact a dissolution event, we looked at the ratio of $CaCO_3$ to $BaSO_4$, as well as the ratio of SiO_2 to TiO_2. High $CaCO_3/BaSO_4$ is indicative of high preservation, whereas a low ratio would indicate increased dissolution. Lower than average $CaCO_3/BaSO_4$ indicates an increase in dissolution because they both are fixed in the water column in proportion to C_{org} rain and are linear with respect to each other [*Dymond and Collier*, 1996; *Piela et al.*, 2012].

We find that the main $CaCO_3$ minimum in U1337, identified by *Dubois and Mitchell* [2012] as the Lavender event, is accompanied by a low $CaCO_3/BaSO_4$ ratio, indicating that there is increased dissolution occurring at this time (Figure 17). As shown in Figure 16, the $CaCO_3/BaSO_4$ ratio is near 18, a minimum within the entire Lavender interval, indicating a loss of $CaCO_3$ relative to $BaSO_4$. Additionally, this ratio is very low during peak MCO warming at 15.5 Ma.

The ratio of Si/Ti has been used to locate intervals of increased productivity [*Holbourn et al.*, 2014]. This ratio is a measure of the relative increase in bio-SiO_2 deposition, assuming that the Ti deposition from aluminosilicates has not varied greatly. The Neogene PEAT core sites are located far from land, so the primary aluminosilicate input to the region is through dust, which adds both Si and Ti to the bulk sediment. However, the majority (~80%) of the Si in equatorial Pacific sediments is in the form of biogenic opal (bio-SiO_2), precipitated from seawater by diatoms and to a minor extent by radiolarians. Clay SiO_2 makes up an average of 20% of the total Si in Site U1337 sediments before and after the Lavender interval.

`

There are only small changes in the SiO_2/TiO_2 ratio (Figure 17) during this time, relative to the rest of the record shown, indicating elevated opal deposition relative to $CaCO_3$ did not occur during the Lavender interval, which would have diluted the carbonate signal causing a decrease in $CaCO_3$ content of the sediment. Since opal is the only major sedimentary component in these cores other than $CaCO_3$, a $CaCO_3$ dissolution event should increase the amount of clay (i.e., dust) and the amount of opal in the bulk sediment but the ratio of SiO_2/TiO_2 would not change significantly. If there is a biogenic opal bloom, the $CaCO_3$ content will have a significant decrease while the SiO_2/TiO_2 will increase greatly [*Holbourn et al.*, 2014], as was found in U1338 at the end of the MCO at 14.0 and 13.8 Ma. *Holbourn et al.* [2014] attributed the events to intensification of equatorial upwelling associated with high-latitude cooling and argued that the enhanced biological pump may have helped to draw down atmospheric CO_2. We find similar SiO_2/TiO_2 events at Site U1337 at the end of the MCO, but do not find similar events during the Lavender interval.

As previously stated, the Lavender interval is present in the cores from U1335, U1336, U1337, and U1338, the estimated wt% $CaCO_3$ of which is plotted in U1337 equivalent depth and interpolated age in Figure 13. Peak dissolution occurred at roughly 16.9 Ma and the entire event lasted from 17.6 to 16.4 Ma. The MCO is currently estimated to have spanned from ~17 to 13.9 Ma [*Holbourn et al.*, 2007; *Tian et al.*, 2013; *Holbourn et al.*, 2014], which encompasses the peak dissolution of the Lavender interval. This peak dissolution is associated with the first warming step of the MCO.

`

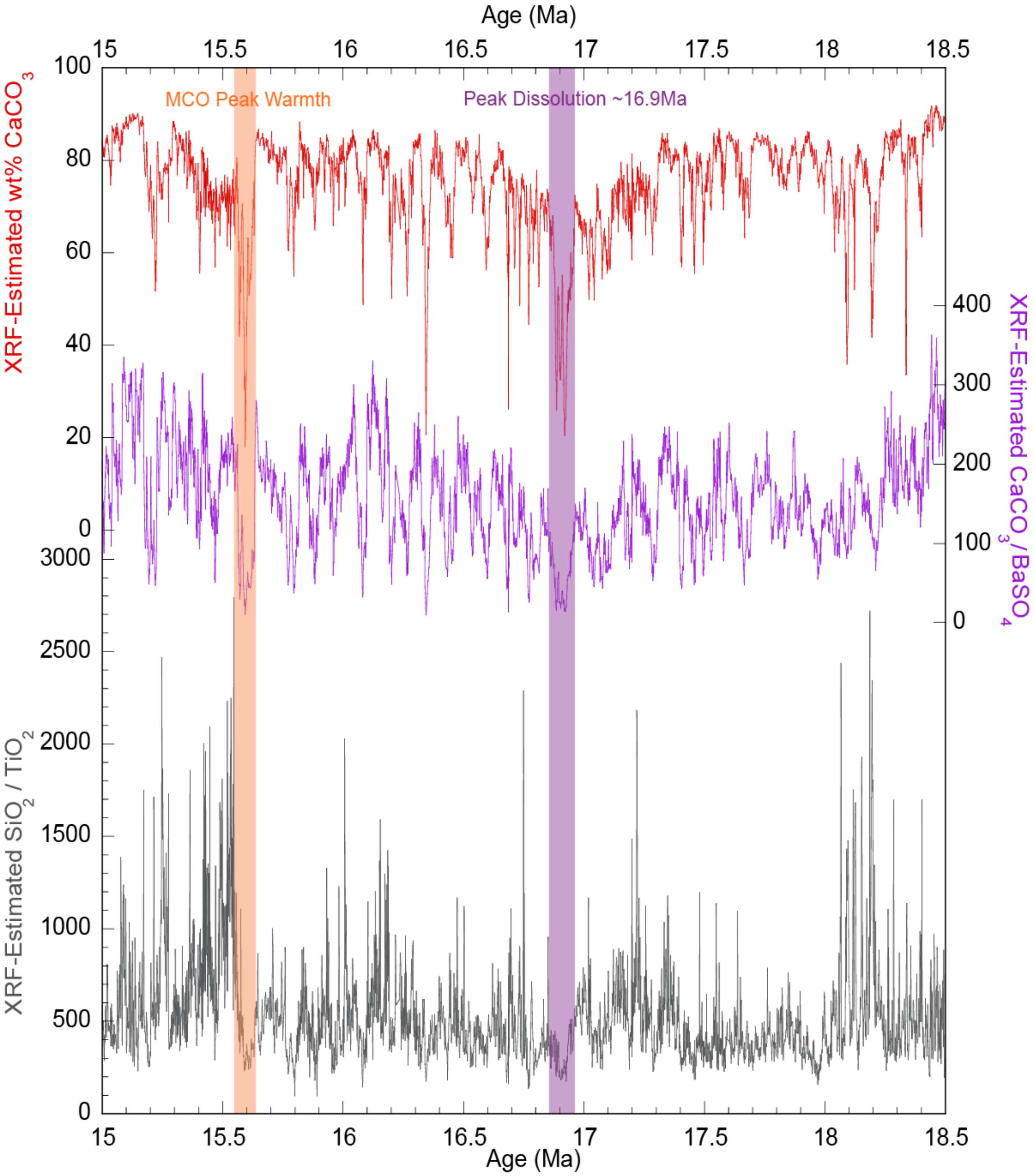

Figure 17 U1337 ratios. U1337 wt% $CaCO_3$ (red) plotted with ratios of $CaCO_3/BaSO_4$(purple) and SiO_2/TiO_2 (grey) by age. MCO peak warmth and Lavender interval peak dissolution are highlighted. The ratio of $CaCO_3/BaSO_4$ is at a minimum at peak dissolution, indicating a loss of $CaCO_3$ relative to $BaSO_4$ and therefore carbonate dissolution. The ratio of SiO_2/TiO_2 shows a relatively small change during peak dissolution indicating elevated opal deposition relative to $CaCO_3$ did not occur at that time, which would have diluted the $CaCO_3$ signal.

`

4.5.2 Causes of Lavender Event $CaCO_3$ Dissolution

We have shown that the Lavender low $CaCO_3$ interval is clearly a dissolution signal, and have also shown that the low $CaCO_3$ interval spanned the entire equatorial Pacific region east of Hawaii. The Lavender event is made up of a series of orbitally-driven dissolution cycles that climaxed at 16.9 Ma.

The Lavender event marks a distinctive disruption in $CaCO_3$ burial in the equatorial Pacific, one of the major $CaCO_3$ depocenters in the global oceans. Such a disruption should indicate a major change in the carbon cycle. Here we investigate 3 potential disrupters of $CaCO_3$ deposition: a change in organic carbon deposition to the deep ocean reducing deep $[CO_3^{2-}]$; a change in mantle CO_2 outgassing associated with the formation of a Large Igneous Province (LIP), the Columbia River Basalt (CRB) province; and basin-basin fractionation, where development of a new $CaCO_3$ depocenter in the Atlantic reduces $CaCO_3$ deposition in the Pacific. Of these 3, the timing of the Lavender event favors basin-basin fractionation.

4.5.2.1 The Monterey Carbon Excursion

The start of the Lavender interval (~17.6 Ma) is earlier than the assumed start of the Monterey carbon isotope excursion [16.9-13.7 Ma, *Holbourn et al.*, 2007], as well as being older than that of the CRB flood basalt eruptions [~16.8-5.5 Ma, *Reidel and Tolan*, 2013]. The Monterey carbon isotope excursion was a long-lasting positive carbon isotope excursion consisting of nine 400 ky cycles showing high coherence with the long (400 ky) eccentricity period [*Holbourn et al.*, 2007]. In addition, the short high-frequency (100 ky) variations superimposed on the low-frequency eccentricity period closely track the modulation of the short eccentricity period. As stated in *Holbourn et al*. [2007], there are multiple records of the Monterey carbon isotope excursion globally, and these records imply changes in the global carbon reservoir linked to eccentricity forcing. Moreover, the rhythm during the Monterey carbon isotope excursion may have been caused by enhanced C_{org} burial, thereby causing increased CO_2 drawdown [*Holbourn et al*., 2007] and higher $CaCO_3$ deposition to remove excess alkalinity relative to the DIC. This would cause the excursion to have more of a preservation signal rather than a dissolution signal. While the beginning of the Monterey excursion was at the same time as peak dissolution during the Lavender interval (~16.9 Ma), it could not have been the driver of the dissolution although the increased carbonate preservation that occurs with increased C_{org} burial may have helped to return $CaCO_3$ burial to levels occurring before 18 Ma.

During the Lavender interval prior to the start of the peak dissolution event (~18 Ma), the CCD in the EEP had shoaled by ~600 m [*Pälike et al*., 2012]. This shoaling lasted for 2.5 million years and has been described as the "carbonate famine" [*Lyle*, 2003]. The CCD deepened again around 16 Ma due to an increase in carbonate productivity [*Pälike et al.*, 2012]. *Pälike et al.* [2012] argue that there are only a couple of mechanisms that would have been able to control the large amplitude CCD changes and sustain the new steady-state. The first involves a change in the type (labile or refractory) of C_{org} being delivered to the seafloor; the second involves changes in weathering and solute input to the deep ocean. An increase in labile C_{org} would increase $CaCO_3$ dissolution owing to that C_{org} being more easily remineralized. Conversely, an

`

increase in refractory C_{org} would increase $CaCO_3$ preservation owing to the C_{org} being harder to degrade and an increase in C_{org} burial.

4.5.2.2 Columbia River Basalt Emplacement

Another hypothesized cause of the Lavender dissolution interval was the eruption of the CRB flood basalts. These eruptions could have released significant amounts of CO_2 trapped in the lithosphere that potentially could, when equilibrated with the ocean, have caused increased carbonate dissolution in the deep Pacific. Unfortunately, the timing does not agree with such a hypothesis. The peak Lavender interval $CaCO_3$ dissolution occurs slightly before the onset of the southeast Oregon eruptions that began the deposition of the CRB in North America [16.8-16.6 ± 0.34 Ma, dated using $^{40}Ar/^{39}Ar$ methods *Barry et al.*, 2010]. Greater than 96% of the basalts in the CRB system were emplaced during the ~800,000 yr between 16.8 and 15.6 Ma, as the Lavender interval was coming to a close. The flood basalt deposition and the equatorial Pacific dissolution event can only be linked if volatile degassing is associated with the initial emplacement of the magma in the crust, not the eruption [*Sobolev et al.*, 2011]. *Sobolev et al.* [2011] modeled the emplacement of the Siberian Traps at the end of the Permian and how that might affect CO_2 degassing. Their model suggests that during mantle plume emplacement, much CO_2 is extracted and released from recycled crust prior to the main basalt eruption. For the CRB emplacement to have been the cause of the Lavender interval, significant degassing would have had to have occurred ~800,000 yr prior to the commencement of peak eruption to fit with Lavender event timing. There is no evidence for this having happened.

`

4.5.2.3 Basin-Basin Fractionation

The best match in timing that we have found for the Lavender dissolution interval is an Atlantic-Pacific basin-basin fractionation interval, driven by an early but temporary increase in Northern Component Water (NCW) formation and increased carbonate deposition in the Atlantic [*Wright and Miller*, 1996]. Evidence of this can be seen in large-scale changes in sedimentation in the North Atlantic as well as in the U1337 and *Wright and Miller* [1996] benthic foraminiferal $\delta^{13}C$ records.

Additional deposition of $CaCO_3$ anywhere in the oceans outside of the Pacific basin will cause a shoaling of the Pacific carbonate compensation depth (CCD) because part of the $CaCO_3$ burial and reduction of alkalinity needed to balance weathering is no longer occurring in the Pacific Ocean. Additional $CaCO_3$ burial on shallow continental margins [*Opdyke and Wilkinson*, 1988] or in deep basins outside of the Pacific [*Berger*, 1970] will partly balance the weathering fluxes of both Ca and HCO_3. The net alkalinity in the deep Pacific and deep $[CO_3^{2-}]$ will necessarily decrease when burial increases elsewhere and more $CaCO_3$ will dissolve from surface sediments in the equatorial Pacific, driving sediment $CaCO_3$% down.

The magnitude of the Atlantic-Pacific basin-basin effect scales roughly with the size of the deep Atlantic versus the deep Pacific assuming similar carbonate mass accumulation rates. If the Atlantic CCD prior to the development of NCW is 3 km and it drops to 4 km with NCW flow, roughly 17×10^6 km^2 [*Menard and Smith*, 1966] becomes a sink for $CaCO_3$, eliminating a similar depositional area in the Pacific. A CCD increase from 3 to 4 km in the Atlantic would cause a shoaling in the Pacific CCD

`

of about 300 m if the CCD was originally at ~5 km, because of the difference in sea floor area between the Pacific and Atlantic [*Menard and Smith*, 1966]. Total shoaling of the Pacific CCD was about 600 m at 17 Ma [*Pälike et al.*, 2012] indicating that the change in carbonate depositional area could have been responsible for at least part of the $CaCO_3$ dissolution in the Pacific during that time.

4.5.2.3.1 Large Scale Sedimentation Changes in the North Atlantic and Evidence of Northern Component Water

Numerous studies [*Miller and Tucholke*, 1983; *Wright and Miller*, 1996; *Davies et al.*, 2001; *Via and Thomas*, 2006; *Thomas and Via*, 2007] have indicated that there were multiple pulses of NCW during the Oligocene and into the early Miocene that were felt throughout the world ocean. In the modern system, Greenland, Iceland, Norwegian (GIN) Seas, and Labrador Sea overflow waters form North Atlantic Deep Water (NADW) by winter convection of high salinity subtropical surface water that has been advected northward and then cooled. In the Late Eocene, the ocean basins were slightly smaller and continental latitudes ~5-10 degrees lower, and cooling of high salinity waters created a proto-NADW water mass and increased latitudinal gradients [*Miller and Tucholke*, 1983]. *Miller and Tucholke* [1983] describe a number of regionally traceable seismic reflectors in the North Atlantic that are used as evidence for the initiation and development of the deepwater circulation in the northern Atlantic. Reflector “R4” is dated to approximately late Eocene to early Oligocene and was the result of an increase in bottom water outflow from the Norwegian-Greenland Sea following the initial subsidence of the Greenland-Scotland Ridge around 40 Ma [*Miller*

`

and Tucholke, 1983]. The widespread distribution of reflector R4 and its correlation with an unconformity indicates that strong abyssal circulation was affecting the North Atlantic basins and was regional in nature. Reflector “R2” dates to the late early Miocene, suggesting continued current-controlled sedimentation in the eastern North Atlantic at this time [*Miller and Tucholke*, 1983].

Wright and Miller [1996] continued to investigate the role of tectonics on the production of a proto-NADW water mass and concluded that the mantle plume activity beneath the region was somewhat responsible for changes in water mass development. Sill depths along the Greenland-Scotland Ridge (GSR), which is part of the mantle plume system centered under the Icelandic Plateau [Figure 1 in *Wright and Miller*, 1996], are important in the production of NCW because the ridge separates the North Atlantic from the colder/denser waters in the Arctic Ocean and Norwegian and Greenland Seas. Overflow is sensitive to small changes in ridge depth and there is a growing body of evidence indicating there was a significant phase of NCW production during the early Miocene [*Wright and Miller*, 1996; *Miller and Tucholke*, 1983; *Davies et al.*, 2001; *Thomas and Via*, 2007]. During periods of low mantle plume activity, NCW production was high, and periods of high mantle plume activity corresponded to periods of low NCW production [*Wright and Miller*, 1996]. *Davies et al*. [2001] concluded that NCW production was initiated during the Oligocene ca. 35 Ma and we hypothesize that increased NCW production during the early Miocene caused increased dissolution and was at least in part responsible for the Lavender dissolution interval in the EEP. *Wright and Miller* [1996] and others [*Davies et al.*, 2001; *Via and Thomas*,

`

2006] conclude that a major pulse of NCW production first appeared prior to the initiation of carbonate dissolution in the EEP but peaked at ~17 Ma and had ceased by ~15 Ma. The timing of this early Miocene pulse of NCW agrees well with our U1337 and the *Holbourn et al.* [2014] U1338 benthic carbon isotopic data as well as the $CaCO_3$ wt% data, as discussed below.

Via and Thomas [2006] and *Thomas and Via* [2007] used changes in ε_{Nd} in cores from the Walvis Ridge (southeastern Atlantic) to track changes in NCW input and source during the Neogene. Their data suggest that the deep waters in the southeastern Atlantic formed in the Southern Ocean until the early Oligocene and that the Nd isotopic values from the Walvis Ridge and Maud Rise diverged, indicating a change in source waters to the Walvis Ridge [*Via and Thomas*, 2006]. This change in source water to the southeast Atlantic began during the Oligocene due to subsidence of the Greenland-Scotland Ridge, however subsidence was not continuous, and NCW was cut off at various points. The NCW contributions to overall Atlantic meridional overturning circulation intensified during the Miocene, however, while there was brief intensification in the early Miocene, *Thomas and Via* [2007] found that the majority of NCW intensification was between 12 and 10 Ma.

4.5.2.3.2 $\delta^{13}C$ Records

The $\delta^{13}C$ values of DIC can be used to trace water masses because the $\delta^{13}C$ value and nutrient content of a water mass is a function of how long that water mass has been isolated from the surface [*Wright and Miller*, 1996]. Deep water that is sourced from the surface and is closer to its source has high DIC $\delta^{13}C$ values and low nutrients because

`

the surface water has been stripped of nutrients and isotopically light $\delta^{13}C$ by primary productivity. As that water mass ages and moves further away from its source, nutrients build up from decay of particulate rain and the $\delta^{13}C$ values of the DIC decrease. This decrease in the $\delta^{13}C$ is due to the oxidation of organic matter, which releases very negative $\delta^{13}C$ [approximately -25‰, *Wright and Miller*, 1996]. Very low $\delta^{13}C$ values are also indicative of a larger DIC pool. Additionally, there is a buildup of CO_2 and DIC in those deep older water masses, making them more corrosive [*Wright and Miller*, 1996; *Lyle et al.*, 1995]. More corrosive water leads to increased $CaCO_3$ dissolution.

At the onset of dissolution in the EEP at 17.6 Ma, there was a ~0.8‰ decrease in $\delta^{13}C$ at Site U1337 followed by a general increase in $\delta^{13}C$ values until ~16.9 Ma. At peak dissolution (16.9 Ma), there is another decrease (~0.6‰) in the $\delta^{13}C$ values, though not as great as at the onset of dissolution. This decrease is then followed by a second increase, which began the "Monterey" carbon-isotope excursion detailed by *Holbourn et al.* [2007]. The cause of these decreases in $\delta^{13}C$ values, we hypothesize, is increased Northern Component Water (NCW) in the North Atlantic, driving changes in the Southern Ocean water entering the Pacific.

According to *Wright et al.* [1992] and *Wright and Miller* [1996], the first pulse of NCW in the Miocene began around 20 Ma and peaked at ~17 Ma. *Wright and Miller* [1996] use the Southern Ocean $\delta^{13}C$ record to investigate the relative strength of input from the Atlantic, Pacific, and Indian Oceans. When NCW production is increased, the Southern Ocean $\delta^{13}C$ values are higher than the Pacific values, though not as high as the Atlantic values. Conversely, when NCW production is reduced or ceases, the Southern

`

Ocean $\delta^{13}C$ values are more similar to the Pacific values [Figure 5, *Wright and Miller*, 1996]. We have plotted our $\delta^{13}C$ data with the data from *Wright and Miller* [1996] in Figure 18 with North Atlantic $\delta^{13}C$ values in green, Southern Ocean in orange, Pacific in black, and U1337 in dark pink. The Lavender dissolution interval has been shaded in purple. The U1337 $\delta^{13}C$ values follow the same trend as the original Pacific values, just at a much finer resolution. The $\delta^{13}C$ values are all fairly similar and begin to diverge around ~18 Ma, with the North Atlantic and Southern Ocean values increasing with respect to the Pacific values. This trend continues throughout the Lavender dissolution interval. The timing of this early Miocene pulse of NCW agrees with our U1337 benthic carbon isotopic data as well as the $CaCO_3$ wt% data.

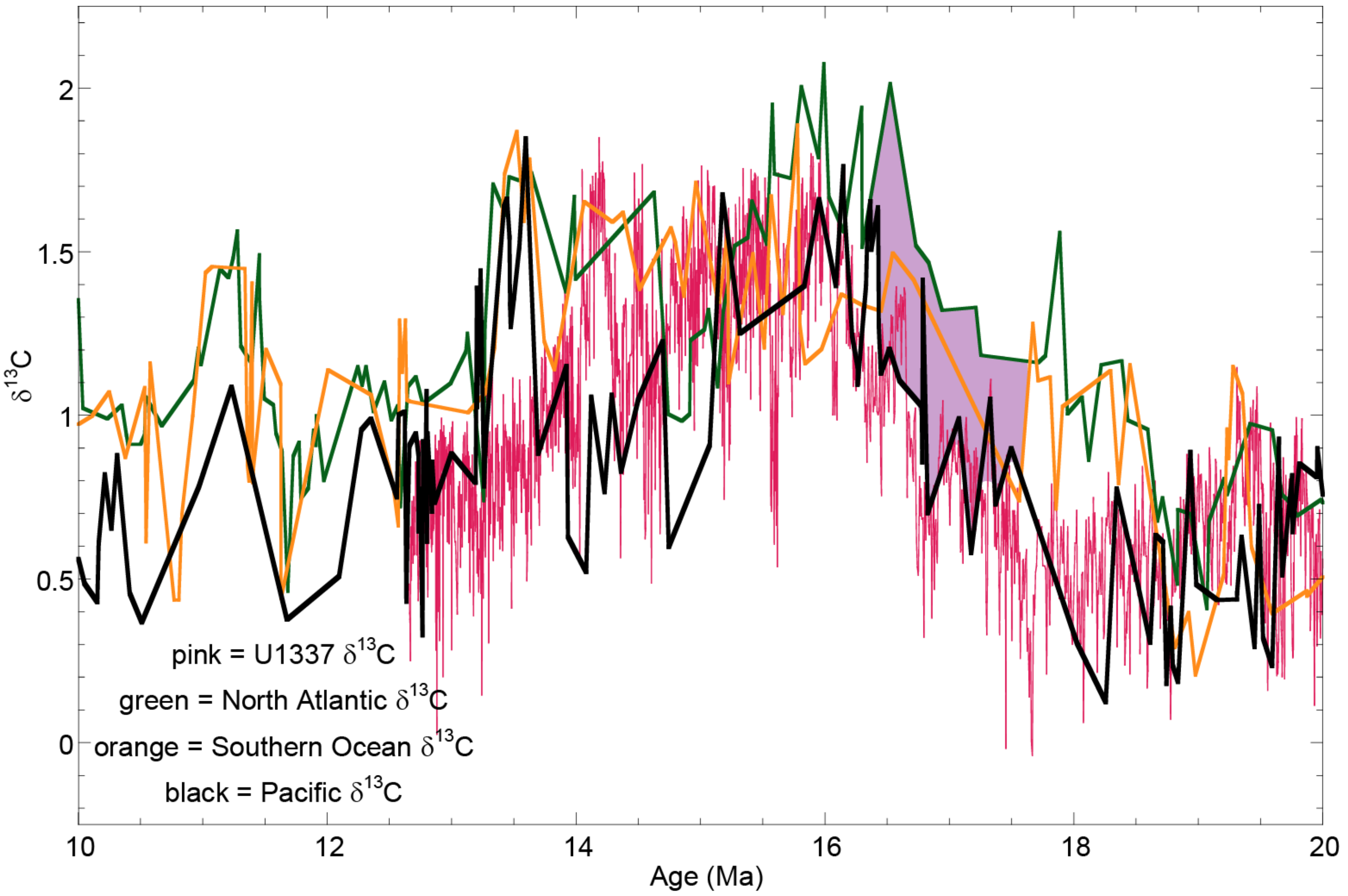

Figure 18 Miocene benthic foraminiferal $\delta^{13}C$ curves. Composite $\delta^{13}C$ curves from the North Atlantic (green), Southern Ocean (orange), and Pacific (black) are from *Wright and Miller* [1996; and references therein]. U1337 d13C (pink) has much finer resolution, however generally follows the Pacific data from *Wright and Miller* [1996]. The Lavender Dissolution Interval is shaded in purple.

4.6 Conclusions

The Lavender dissolution interval lasted approximately 1.2 m.y. and is strongly influenced by orbital insolation changes. Due to the sedimentation rates (~25 m/m.y.) and the spacing of the XRF sampling, we have ~1,000 y resolution in our records from these four PEAT cores. This large amount of data allows us to resolve Milankovitch cycling. The spectral analysis performed on this time series indicates dominant peaks at characteristic Milankovitch cyclicity on an approximately 100,000 y time scale (Figure 19). This periodicity indicates forcing in the eccentricity band.

We have investigated 3 potential causes of the Lavender dissolution interval: a change in organic carbon deposition to the deep ocean reducing deep [CO_3^{2-}]; a change in mantle CO_2 outgassing associated with the formation of the CRB province; and basin-basin fractionation, where development of a new $CaCO_3$ depocenter in the Atlantic reduces $CaCO_3$ deposition in the Pacific. Of these 3 potential drivers, the timing of the Lavender event favors basin-basin fractionation.

`

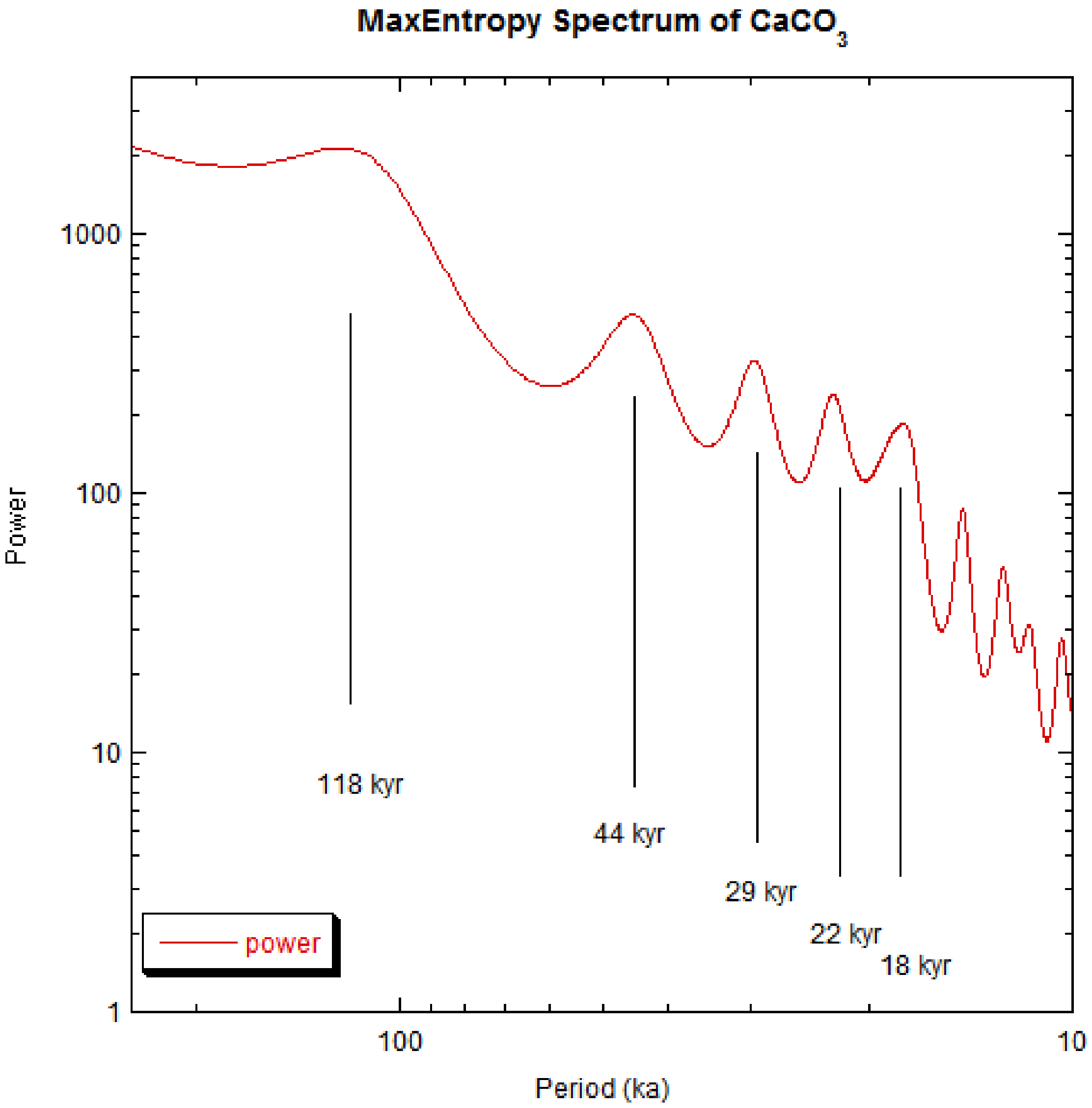

Figure 19 Spectral Analysis. Spectral analysis performed indicates dominant peaks at characteristic Milankovitch cyclicity with forcing in the eccentricity band.

`

CHAPTER V

CONCLUSIONS

As the world's largest ocean, the Pacific Ocean is intrinsically linked to the major changes in current and past climate, in particular, the carbon cycle. Studying the fluctuations in the $CaCO_3$ content of ocean sediments and determining the nature, timing, and drivers of those fluctuations is essential to further understanding of the complex systems at work within the oceans. This project focused on a particular $CaCO_3$ fluctuation that lasted ~1.2 m.y. and was regionally traceable. The stated goals of this study included: collecting and calibrating bulk sediment chemistry on four Neogene PEAT sediment cores; determining the difference between dissolution and productivity signals within those sediment cores; correlating the Lavender interval across the eastern and central Pacific; and utilizing other proxy records to aid in determining the nature, timing, and forcing mechanism that cause the Lavender seismic horizon to be deposited. These goals have been met and have resulted in an extremely large data set that will be incorporated as part of the larger Cenozoic "megasplice" and aid in reconstructing climate over the last 60 m.y.

In addition to producing the dataset and meeting the study goals, the hypotheses of the project have been verified:

1. XRF scanning generates an enormous amount of data and allows for much finer resolution than is typical of discrete geochemical sampling and can be utilized to distinguish between productivity and dissolution events during the Miocene, as seen in the Neogene PEAT sediment cores. The ratios of sedimentary

components are used to distinguish between types of events occurring during deposition.

2. The Lavender seismic horizon originally identified by *Mayer et al.* [1985] has been positively identified as a $CaCO_3$ dissolution event using the XRF scan data as well as other geochemical proxy data. The event has been correlated across the EEP using the IODP 320/321, ODP 199, and DSDP 85 sediment cores and seismic data.
3. The best driver of the Lavender Dissolution Interval has been determined to be basin-basin fractionation caused by an increase in Atlantic NCW formation. The formation of NCW caused the CCD in the Atlantic to deepen, thereby shoaling the CCD in the Pacific and allowing increased deposition of $CaCO_3$ in the Atlantic while prohibiting $CaCO_3$ deposition in the Pacific. Of the three potential drivers investigated, the timing of NCW formation best agrees with the record seen in the sediment cores.

`

REFERENCES

Anderson, R.F., M.Q. Fleisher, Y.Lao, and G. Winckler (2008), Modern $CaCO_3$ preservation in equatorial Pacific sediments in the context of late-Pleistocene glacial cycles, Marine Chemistry, 111, 30-46.

Barry, T.L., S. Self, S.P. Kelley, S. Reidel, P. Hooper, and M. Widdowson (2010), New $^{40}Ar/^{39}Ar$ dating of the Grande Ronde lavas, Columbia River Basalts, USA: Implications for duration of flood basalt eruption episodes, Lithos, 118, 213-222, doi: 10.1016/j.lithos.2010.03.014.

Berger, W. H. (1970), Biogenous deep-sea sediments: fractionation by deep-sea circulation, Geological Society of America Bulletin, 81, 1385-1402.

Berger, W.H. (1972), Deep Sea Carbonates: Dissolution facies and age-depth constancy, Nature, 236, 392-395.

Billups, K., H. Pälike, J.E.T. Channell, J.C. Zachos, and N.J. Shackleton (2004), Astronomic calibration of the late Oligocene through early Miocene geomagnetic polarity time scale, Earth Planet. Sci. Lett., 224, 33-44.

Boudreau, B.P., J.L. Middleberg, and F.J.R. Meysman (2010), Carbonate compensation dynamics, Geophysical Research Letters, Vol. 37, L03603, doi:10.1029/2009GL041847.

Cranston, R.E. and D.E. Buckley (1990), Redox reactions and carbonate preservation in deep-sea sediments, Marine Geology, 94, 1-8.

Davies, R., J. Cartwright, J. Pike, and C. Line (2001), Early Oligocene initiation of North Atlantic Deep Water formation, Nature, 410, 917-920.

Dubois, N. and N.C. Mitchell (2012), Large-scale sediment redistribution on the equatorial Pacific seafloor, Deep-Sea Research I, 69, 51-61.

Dymond, J. and R. Collier (1988), Biogenic particle fluxes in the equatorial Pacific: Evidence for both high and low productivity during the 1982-1983 El Niño, Global Biogeochemical Cycles, 2(2), 129-139.

Dymond, J., E. Suess, and M. Lyle (1992), Barium in deep-sea sediment: A geochemical proxy for paleoproductivity, Paleoceanography, 7(2), 163-181.

Dymond, J., and R. Collier (1996), Particulate barium fluxes and their relationships to biological productivity, Deep Sea Research II, 43(4-6), 1283-1308.

Dymond, J., R. Collier, and J. McManus (1997), Can the aluminum and titanium contents of ocean sediments be used to determine the paleoproductivity of the oceans?, Paleoceanography, 12(4), 585-593.

Emerson, S. and M. Bender (1981), Carbon fluxes at the sediment-water interface of the deep-sea: Calcium carbonate preservation, Journal of Marine Research, 39, 139-162.

Expedition 320/321 Scientists (2010a), Site U1335. In Pälike, H., Lyle, M., Nishi, H., Raffi, I., Gamage, K., Klaus, A., and the Expedition 320/321 Scientists, Proc. IODP, 320/321: Tokyo (Integrated Ocean Drilling Program Management International, Inc.). doi:10.2204/iodp.proc.320321.107.2010.

Expedition 320/321 Scientists (2010b), Site U1336. In Pälike, H., M. Lyle, H. Nishi, I. Raffi, K. Gamage, A. Klaus, and the Expedition 320/321 Scientists, Proc. IODP, 320/321: Tokyo (Integrated Ocean Drilling Program Management International, Inc.), doi:10.2204/iodp.proc.320321.108.2010.

Expedition 320/321 Scientists (2010c), Site U1337. In Pälike, H., M. Lyle, H. Nishi, I. Raffi, K. Gamage, A. Klaus, and the Expedition 320/321 Scientists, Proc. IODP, 320/321: Tokyo (Integrated Ocean Drilling Program Management International, Inc.), doi:10.2204/iodp.proc.320321.109.2010.

Expedition 320/321 Scientists (2010d), Site U1338. In Pälike, H., M. Lyle, H. Nishi, I. Raffi, K. Gamage, A. Klaus, and the Expedition 320/321 Scientists, Proc. IODP, 320/321: Tokyo (Integrated Ocean Drilling Program Management International, Inc.), doi:10.2204/iodp.proc.320321.110.2010.

Expedition 320/321 Scientists (2010e), Methods. In Pälike, H., M. Lyle, H. Nishi, I. Raffi, K. Gamage, A. Klaus, and the Expedition 320/321 Scientists, Proc. IODP, 320/321: Tokyo (Integrated Ocean Drilling Program Management International, Inc.), doi:10.2204/iodp.proc.320321.102.2010.

Farrell, J.W. and W.L. Prell (1989), Climatic change and CaCO3 preservation: an 800,000 year bathymetric reconstruction from the central equatorial Pacific Ocean, Paleoceanography, 4(4), 447-466.

Hach Company (1997), D/R4000 Procedure: Method 8186 Heteropoly Blue Method.

Honjo, S., J. Dymond, R. Collier, and S.J. Manganini (1995), Export production of particles to the interior of the equatorial Pacific Ocean during the 1992 EqPac experiment, Deep-Sea Research, 42(2-3), 831-870.

Holbourn, A., W. Kuhnt, S. Schulz, and H. Erlenkeuser (2005), Impacts of orbital forcing and atmospheric carbon dioxide on Miocene ice-sheet expansion, Nature, 438, 483-487. doi: 10.1038/nature04123.

`

Holbourn, A., W. Kuhnt, W. Schulz, J.A. Flores, and N. Anderson (2007), Orbitally-paced climate evolution during the middle Miocene “Monterey” carbon-isotope excursion, Earth and Planetary Science Letters, 261, 534-550, doi:10.1016/j.epsl.200707.026.

Holbourn, A., W. Kuhnt, M. Lyle, L. Schneider, O. Romero, and N. Anderson (2014), Middle Miocene climate cooling linked to intensification of eastern equatorial Pacific upwelling, Geology, 42(1), 19-22, doi: 10.1130/G34890.1.

Hovan, S.A. (1995), Late Cenozoic atmospheric circulation intensity and climatic history recorded by eolian deposition in the eastern equatorial Pacific Ocean, Leg 138, In Pisias, N.G., L.A. Mayer, T.R. Janecek, A. Palmer-Julson, and T.H. van Andel (Eds.), Proc. ODP, Sci. Results, 138: College Station, TX (Ocean Drilling Program), 615-625, doi: 10.2973/odp.proc.sr.138.110.1995.

Howell, P., N. Pisias, J. Ballance, J. Baughman, and L. Ochs (2006), ARAND Time-Series Analysis Software, Brown University, Providence, RI.

Jansen, J.H.F, S.J. Van der Gaast, B. Koster, and A.J. Vaars, (1998), CORTEX, a shipboard XRF-scanner for element analysis in split sediment cores. Mar. Geol., 151(1-4):143-153. doi:10.1016/S0025-3227(98)00074-7.

Koppers, A.A.P, J. Phipps Morgan, J.W. Morgan, and H. Staudigel (2001), Testing the fixed hotspot hypothesis using ^{40}Ar/^{39}Ar age progressions along seamount trails, Earth Planet. Sci. Lett., 185(3-4), 237-252, doi:10.1016/S0012-821X(00)00387-3.

Laskar, J., P. Robutel, F. Joutel, M. Gastineau, A.C.M Correia, and B. Levrard (2004), A long term numerical solution for the insolation quantities of the Earth, Astron. Astrophys., 428, 261-285.

Lourens, L.J., F.J. Hilgen, J. Laskar, N.J. Shackelton, and D. Wilson (2004), The Neogene period. Gradstein, F., J. Ogg, and A. Smith (Eds.), A Geological Time Scale. Cambridge University Press, pp. 409-440.

Lyle, M., K.A. Dadey, and J.W. Farrell (1995), The late Miocene (11 – 8 Ma) eastern Pacific carbonate crash: Evidence for reorganization of deepwater circulation by the closure of the Panama Gateway, Proc. Ocean Drill. Program Sci. Results, 138, 821-838, doi:10.2973/odp.proc.sr.138.157.1995.

Lyle, M., A. Mix, A.C. Ravelo, D. Andreasen, L. Heusser, and A. Olivarez (2000), Millennial-scale CaCO3 and Corg events along the northern and central California margins: stratigraphy and origins, Proceedings of the Ocean Drilling Program, Scientific Results, 167, 163-182.

`

Lyle, M., A. Mix, and N. Pisias (2002), Patterns of $CaCO_3$ deposition in the eastern tropical Pacific Ocean for the last 150 kyr: Evidence for a southeast Pacific depositional spike during marine isotope stage (MIS) 2, Paleoceanography, 17(2), doi:10.1029/2000PA000538.

Lyle, M. (2003), Neogene carbonate burial in the Pacific Ocean, Paleoceanography, 18(3), 1059, doi:10.1029/2002PA000777.

Lyle, M., H. Pälike, H. Nishi, I. Raffi, K. Gamage, A. Klaus, and the IODP Expeditions 320/321 Science Party (2010), The Pacific Equatorial Age Transect, IODP Expeditions 320 and 321: building a 50-million-year-long environmental record of the equatorial Pacific, Ocean. Sci. Drill., 9:4–15, doi:10.2204/iodp.sd.9.01.2010.

Lyle, M., A. Olivarez Lyle, T. Gorgas, A. Holbourn, T. Westerhold, E. Hathorn, K. Kimoto, and S. Yamamoto (2012), Data report: raw and normalized elemental data along the U1338 splice from X-ray fluorescence scanning, In Pälike, H., M. Lyle, H. Nishi, I. Raffi, K. Gamage, A. Klaus, and the Expedition 320/321 Scientists, Proc. IODP, 320/321: Tokyo (Integrated Ocean Drilling Program Management International, Inc.), doi: 10.2204/iodp.proc.320321.205.2013.

Lyle, M. and J. Backman (2013), Data report: calibration of XRF-estimated CaCO3 along the Site U1338 splice, In Pälike, H., M. Lyle, H. Nishi, I. Raffi, K. Gamage, A. Klaus, and the Expedition 320/321 Scientists, Proc. IODP, 320/321: Tokyo (Integrated Ocean Drilling Program Management International, Inc.), doi: 10.2204/iodp.proc.320321.205.2013.

Marcantonio, R., R.F. Anderson, M. Stute, N.Kumar, P. Schlosser, and A. Mix (1996), Extraterrestrial 3He as a tracer of marine sediment transport and accumulation, Nature, 383(6602), 705-707.

Marchitto, T.M., J. Lynch-Stieglitz, and S.R. Hemming (2005), Deep Pacific $CaCO_3$ compensation and glacial-interglacial atmospheric CO_2, Earth and Planetary Science Letters, 231, 317-336.

Mayer, L.A., T. H. Shipley, F. Theyer, R.H. Wilkens, and E.L. Winterer, E.L. (1985), Seismic modeling and paleoceanography at Deep Sea Drilling Project Site 574. I Mayer, L., Theyer, F., Thomas, E., et al., Init. Repts. DSDP, 85: Washington (U.S. Govt. Printing Office), 947–970.

Mayer, L.A., T.H. Shipley, and E.L. Winterer (1986), Equatorial Pacific seismic reflectors as indicators of global oceanographic events, Science, 233, 761-764.

Menard, H.W., and S.M. Smith (1966), Hypsometry of Ocean Basin Provinces, Journal of Geophysical Research, 71(18), 4305-4325.

`

Miller, K.G., and B.E. Tucholke (1983), Development of Cenozoic abyssal circulation south of the Greenland-Scotland Ridge. In Structure and Development of the Greenland-Scotland Ridge, edited by M.H.P. Bott et al., pp. 549-589, Plenum, New York.

Mitchell, N.C., M.W. Lyle, M. B. Knappenberger, and L. M. Liberty (2003), Lower Miocene to present stratigraphy of the equatorial Pacific sediment bulge and carbonate dissolution anomalies, Paleoceanography, 18(2), doi: 10.1029/2002PA000828.

Moore, T.C., Jr., J. Backman, I. Raffi, C.A. Nigrini, A. Sanfilippo, H. Pälike, and M. Lyle (2004), The Paleogene tropical Pacific: clues to circulation, productivity, and plate motion, Paleoceanography, 19, doi: 10.1029.2003PA000998.

Mortlock, R.A. and P.N. Froelich (1989), A simple method for the rapid determination of biogenic opal in pelagic marine sediments, Deep Sea Research Part A. Oceanography Research Papers, 36(9), 1415-1426.

Müller, P.J. and A. Mangini (1980), Organic carbon decomposition rates in sediments of the Pacific manganese nodule belt dated by 230Th and 231Pa, Earth and Planetary Science Letters, 51(1), 94-114, doi: 10.1016/0012-821X(80)90259-9.

Murray, R.W. and M. Leinen (1993), Chemical transport to the seafloor of the equatorial Pacific Ocean across a latitudinal transect at 135W: tracking sedimentary major, trace, and rare earth element fluxes at the equator and the Intertropical Convergence Zone, Geochimica et Cosmochimica Acta, 57, 4141-4163.

Ohneiser, C., G. Acton, J.E.T. Channell, G.S. Wilson, Y. Yamamoto, and T. Yamazaki (2013), A middle Miocene relative paleointensity record from the Equatorial Pacific, Earth and Planetary Science Letters, 374, 227-238, doi: 10.1016/j.epsl.2013.04.038.

Olivarez Lyle, A., and M.W. Lyle, (2002), Determination of biogenic opal in pelagic marine sediments: a simple method revisited. In Lyle, M., P.A. Wilson, T.R. Janecek,, et al., Proc. ODP, Init. Repts., 199: College Station, TX (Ocean Drilling Program), 1–21. doi:10.2973/odp.proc.ir.199.106.2002.

Opdyke, B.N., and B.H. Wilkinson (1988), Surface area control of shallow cratonic to deep marine carbonate accumulation, Paleoceanography, 3(6), 685-703.

Pälike, H., Nishi, H., Lyle, M., Raffi, I., Gamage, K., Klaus, A., and the Expedition 320/321 Scientists (2010), Expedition 320/321 summary. In Pälike, H., M. Lyle, H. Nishi, I. Raffi, K. Gamage, A. Klaus, and the Expedition 320/321 Scientists, Proc. IODP, 320/321: Tokyo (Integrated Ocean Drilling Program Management International, Inc.), doi:10.2204/iodp.proc.320321.101.2010.

`

Pälike, H., M.W. Lyle, H. Nishi, I. Raffi, A. Ridgwell, K. Gamage, A. Klaus, G. Acton, L. Anderson, J. Backman, J. Baldauf, C. Beltran, S.M. Bohaty, P. Bown, W. Busch, J.E.T. Channell, C.O.J. Chun, M. Delaney, P. Dewangan, T. Dunkley Jones, K.M. Edgar, H. Evans, P. Fitch, G.L. Foster, N. Gussone, H. Hasegawa, E.C. Hathorne, H. Hayashi, J.O. Herrle, A. Holbourn, S. Hovan, K. Hyeong, K. Iijima, T. Ito, S. Kamikuri, K. Kimoto, J. Kuroda, L.Leon-Rodriguez, A. Malinverno, T.C. Moore, Jr., B.H. Murphy, D.P. Murphy, H. Nakamura, K. Ogane, C. Ohneiser, C. Richter, R. Robinson, E.J. Rohling, O. Romero, K. Sawada, H.Scher, L. Schneider, A. Sluijs, H. Takata, J. Tian, A. Tsujimoto, B.S. Wade, T. Westerhold, R. Wilkens, T. Williams, P.A. Wilson, Y. Yamamoto, S. Yamamoto, T. Yamazaki, and R.E. Zeebe, (2012) A Cenozoic record of the equatorial Pacific carbonate compensation depth, Nature, 488(7409):609–614. doi:10.1038/nature11360.

Paillard, D., L. Labeyrie, and P. Yiou (1996), Macintosh program performs time-series analysis, Eos Trans. AGU, 77, 379 pp.

Piela, C.M (2010), Equatorial Pacific Sediment Deposition during the Early to Middle Miocene: Carbon Cycling and Proxies for Productivity. Master's Thesis, Texas A&M University. Available electronically from http://hdl.handle.net/1969.1/ETD-TAMU-2010-12-8194.

Piela, C., M. Lyle, F. Marcantonio, J. Baldauf, and A. Olivarez Lyle (2012), Biogenic sedimentation in the equatorial Pacific: Carbon cycling and paleoproduction, 12-24 Ma, Paleoceanography, 27, PA2204, 18 pp, doi: 10.1029/2011PA002236.

Reidel, S.P, and T.L. Tolan (2013), The late Cenozoic evolution of the Columbia River system in the Columbia River flood basalt province, Special Paper – Geological Society of America, The Columbia River flood basalt province, 497, 201-230.

Richter, T.O., Van der Gaast, S., Koster, B., Vaars, A., Gieles, R., de Stigter, H.C., De Haas, H., and van Weering, T.C.E. (2006), The Avaatech XRF Core Scanner: technical description and application to NE Atlantic sediments. In Rothwell, R.G. (Ed.), New Techniques in Sediment Core Analysis. Geol. Sco. Spec. Publ., 267(1):39-50. doi:10.1144/GSL.SP.2006.267.01.03.

Shackford, J.K., M. Lyle, R. Wilkens, and J. Tian (2014), Data report: raw and normalized elemental data along the Site U1335, Site U1336, and Site U1337 splices from X-ray fluorescence scanning. In Pälike, H., M. Lyle, H. Nishi, I. Raffi, K. Gamage, A. Klaus, and the Expedition 320/321 Scientists, Proc. IODP, 320/321: Tokyo (Integrated Ocean Drilling Program Management International, Inc.).

Sobolev, S.V., A.V. Sobolev, D.V. Kuzmin, N.A. Krivolutskaya, A G. Petrunin, N.T. Arndt, V.A. Radko, and Y.R. Vasiliev (2011), Linking mantle plumes, large igneous provinces and environmental catastrophes, Nature, 477, 312-316, doi:10.1038/nature10385.

`

Taylor, S. R., and S. M. McLennan (1995), The Geochemical Evolution of the Continental Crust, Reviews of Geophysics, 33(241-265).

Thomas, D.J., and R.K. Via (2007), Neogene evolution of Atlantic thermohaline circulation: Perspective from Walvis Ridge, southeastern Atlantic Ocean, Paleoceanography, 22, PA2212, doi: 10.1029/2006PA1297.

Thomas, E., K.K. Turekian, and K.Y. Wei (2000), Productivity control of fine particle transport to equatorial Pacific sediment, Global Biogeochemical Cycles, 14(3), 945-955.

Tian, J., M. Yang, M. Lyle, R. Wilkens, and J. Shackford (2013), Obliquity and long eccentricity pacing of the Middle Miocene climate transition, Geochemistry, Geophysics, Geosystems, 14(6), 1740-1755.

Tjallingii, R., U. Röhl, M. Kölling, and T. Bickert (2007), Influence of the water content on X-ray fluorescence core-scanning measurements in soft marine sediments, Geochemistry Geophysics Geosystems, 8(2), doi: 10.1029/2006GC001393.

Volat, J.L., L Pastouret, and C. Vergnaud-Grazzini (1980), Dissolution and carbonate fluctuations in Pleistocene deep sea cores: a review, Marine Geology, 34, 1-28.

Via, R.K., and D.J. Thomas (2006), Evolution of Atlantic thermohaline circulation: Early Oligocene onset of deep-water production in the North Atlantic, Geology, 34, 441-444.

Wilkens, R.H., G. R. Dickens, J. Tian, J. Backman, and the Expedition 320/321 Scientists (2013), Data report: revised composite depth scales for Sites U1336, U1337, and U1338. In Pälike, H., M. Lyle, H. Nishi, I. Raffi, K. Gamage, A. Klaus, and the Expedition 320/321 Scientists, Proc. IODP, 320/321: Tokyo (Integrated Ocean Drilling Program Management International, Inc.). doi:10.2204/iodp.proc.320321.209.2013.

Wright, J.D., and K.G. Miller (1996), Control of North Atlantic Deep Water circulation by the Greenland-Scotland Ridge, Paleoceanography, 11, 157-170.

Xie, R. C. and F. Marcantonio (2012), Deglacial dust provenance changes in the eastern equatorial Pacific and implications for ITCZ movement, Earth and Planetary Science Letters, 317-318(0), 386-395, doi: 10.1016.j.epsl.2011.11.014.

`

APPENDIX A

Data tables referenced in Chapter II are provided in this appendix. For very large tables, only the first page has been printed, the full tables are provided as supplementary Microsoft Excel (.xls) files.

Table A1 U1335 raw XRF data. Raw XRF peak area data and calculated NMS data for all scans on Site U1335, spliced. The asterisk (*) indicates data that was used in the calculation of NMS values and in the splice. All data are included, however, in the event that the splice is modified and NMS values need to be recalculated.

* Used in Final U1335 Splice	Site, Hole, Core, Type, Section	Depth in section (mm)	Measurement Date	Depth (mbsf) (CSF-A [m])	Depth (mcd) (CCSF-A [m])	Raw component sum (%)	Al area	Al median-scale	Al_2O_3 NMS	Si area	Si median-scale	SiO_2 NMS	S area	Cl area	K area	K median-scale	K_2O NMS	Ca area	Ca median-scale	$CaCO_3$ NMS	Ti area	Ti median-scale	TiO_2 NMS	Mn area	Mn median-scale	MnO NMS	Fe area	Fe median-scale	Fe_2O_3 NMS	Ba area (50kV scan)	Ba median-scale	$BaSO_4$ NMS
*	U1335B-1H-1	25	1/12/2013	0.025	0.025	36.67	64	0.12	0.32	21039	5.79	15.78	3461	89642	4376	0.15	0.40	994545	28.70	78.26	21264	0.74	2.01	25117	0.37	1.02	41718	0.66	1.79	2894	0.16	0.43
*	U1335B-1H-1	50	1/12/2013	0.05	0.05	31.36	69	0.12	0.40	16866	4.64	14.79	3066	77102	2223	0.07	0.24	859703	24.81	79.10	21041	0.73	2.32	19678	0.29	0.93	35593	0.56	1.79	2512	0.14	0.43
*	U1335B-1H-1	75	1/12/2013	0.075	0.075	36.51	16	0.03	0.08	15265	4.20	11.50	3076	78093	1849	0.06	0.17	1054422	30.42	83.34	23873	0.83	2.27	19784	0.29	0.80	34432	0.54	1.48	2393	0.13	0.36
*	U1335B-1H-1	100	1/12/2013	0.1	0.1	45.57	0	0.00	0.00	18783	5.17	11.34	2734	87922	2788	0.09	0.20	1329295	38.36	84.18	25395	0.88	1.93	23240	0.35	0.76	37394	0.59	1.29	2544	0.14	0.30
*	U1335B-1H-1	125	1/12/2013	0.125	0.125	47.06	0	0.00	0.00	20625	5.67	12.05	3361	85103	4176	0.14	0.30	1367729	39.46	83.85	25818	0.89	1.90	13323	0.20	0.42	35318	0.56	1.18	2578	0.14	0.30
*	U1335B-1H-1	150	1/12/2013	0.15	0.15	45.69	55	0.10	0.22	18874	5.19	11.36	3609	94816	4046	0.14	0.30	1336621	38.57	84.41	26330	0.91	2.00	6128	0.09	0.20	35492	0.56	1.22	2478	0.13	0.29
*	U1335B-1H-1	175	1/12/2013	0.175	0.175	65.34	14	0.03	0.04	29423	8.09	12.39	5432	138633	7242	0.24	0.37	1909932	55.11	84.35	26247	0.91	1.39	5746	0.09	0.13	43378	0.68	1.04	3525	0.19	0.29

`

Table A2 U1336 raw XRF data. Raw XRF peak area data and calculated NMS data for all scans on Site U1336, spliced. The asterisk (*) indicates data that was used in the calculation of NMS values and in the splice. All data are included, however, in the event that the splice is modified and NMS values need to be recalculated.

* Used in Final U1336 Splice	Site, Hole, Core, Type, Section	Depth in section (mm)	Measurement Date	Depth (mbsf) (CSF-A [m])	Depth (mcd) (CCSF-A [m])	Raw component sum (%)	Al area	Al median-scale	Al_2O_3 NMS	Si area	Si median-scale	SiO_2 NMS
*	U1336B-1H-1	25	1/26/2012	0.025	0.025	8.45	234	0.42	4.92	7983	1.85	21.91
*	U1336B-1H-1	50	1/26/2012	0.05	0.05	21.98	515	0.91	4.16	17624	4.09	18.59
*	U1336B-1H-1	75	1/26/2012	0.075	0.075	15.42	234	0.42	2.70	11130	2.58	16.74
*	U1336B-1H-1	100	1/26/2012	0.1	0.1	16.38	326	0.58	3.54	12401	2.87	17.56
*	U1336B-1H-1	125	1/26/2012	0.125	0.125	17.61	466	0.83	4.70	13580	3.15	17.88
*	U1336B-1H-1	150	1/26/2012	0.15	0.15	18.61	624	1.11	5.96	16311	3.78	20.32
*	U1336B-1H-1	175	1/26/2012	0.175	0.175	37.65	418	0.74	1.97	18327	4.25	11.28

Continued from above	S area	Cl area	K area	K median-scale	K_2O NMS	Ca area	Ca median-scale	$CaCO_3$ NMS	Ti area	Ti median-scale	TiO_2 NMS
	1147	15715	1627	0.04	0.42	167300	5.87	69.47	994	0.01	0.18
	1727	34481	7635	0.17	0.76	460791	16.17	73.54	2560	0.04	0.17
	1465	24683	3548	0.08	0.50	340413	11.94	77.46	1266	0.02	0.12
	1625	30083	4623	0.10	0.62	351910	12.35	75.40	1631	0.02	0.15
	1883	31865	5597	0.12	0.69	369816	12.97	73.67	1983	0.03	0.17
	2408	35059	6878	0.15	0.81	368041	12.91	69.39	2069	0.03	0.17
	3911	78713	6271	0.14	0.36	894127	31.37	83.31	2307	0.03	0.09

Continued from above	Mn area	Mn median-scale	MnO NMS	Fe area	Fe median-scale	Fe_2O_3 NMS	Ba area (50kV scan)	Ba median-scale	$BaSO_4$ NMS
	2132	0.04	0.47	16073	0.19	2.28	393	0.03	0.35
	4157	0.08	0.36	38008	0.46	2.07	1015	0.08	0.35
	2761	0.05	0.34	23364	0.28	1.82	678	0.05	0.33
	1554	0.03	0.18	30178	0.36	2.21	783	0.06	0.36
	2413	0.05	0.26	33395	0.40	2.27	832	0.06	0.35
	2978	0.06	0.30	41008	0.49	2.64	1027	0.08	0.41
	9646	0.18	0.48	55104	0.66	1.75	3710	0.28	0.74

`

Table A3 U1337 raw XRF data. Raw XRF peak area data and calculated NMS data for all scans on Site U1337, spliced. The asterisk (*) indicates data that was used in the calculation of NMS values and in the splice. All data are included, however, in the event that the splice is modified and NMS values need to be recalculated.

* Used in Final U1337 Splice	Site, Hole, Core, Type, Section	Depth in section (mm)	Measurement Date	Depth (mbsf) (CSF-A [m])	Depth (mcd) (CCSF-A [m])	Raw component sum (%)	Al area	Al median-scale	Al_2O_3 NMS	Si area	Si median-scale	SiO_2 NMS
*	U1337B-1H-1	25	9/20/2012	1.025	0.025	51.55	280	0.71	1.37	28368	15.11	29.32
*	U1337B-1H-1	50	9/20/2012	1.05	0.05	55.11	-59	0.00	0.00	25856	13.77	24.99
*	U1337B-1H-1	75	9/20/2012	1.075	0.075	81.76	229	0.58	0.71	38038	20.26	24.78
*	U1337B-1H-1	100	9/20/2012	1.1	0.1	70.87	404	1.02	1.44	41109	21.90	30.90
*	U1337B-1H-1	125	9/20/2012	1.125	0.125	82.37	-146	0.00	0.00	35381	18.85	22.88
*	U1337B-1H-1	150	9/20/2012	1.15	0.15	107.58	242	0.61	0.57	41586	22.15	20.59
*	U1337B-1H-1	175	9/20/2012	1.175	0.175	106.35	101	0.26	0.24	43714	23.29	21.90

Continued from above	S area	Cl area	K area	K median-scale	K_2O NMS	Ca area	Ca median-scale	$CaCO_3$ NMS	Ti area	Ti median-scale	TiO_2 NMS
	6694	157102	5002	0.18	0.36	924467	32.47	62.99	3726	0.32	0.61
	9528	274853	6358	0.23	0.43	1062665	37.33	67.73	2858	0.24	0.44
	8085	225515	8191	0.30	0.37	1601528	56.25	68.80	3546	0.30	0.37
	9550	233194	8112	0.30	0.42	1227550	43.12	60.84	4791	0.41	0.57
	7217	221931	6009	0.22	0.27	1696157	59.58	72.33	3166	0.27	0.33
	5909	184897	5587	0.21	0.19	2306080	81.00	75.30	3287	0.28	0.26
	6345	195568	6264	0.23	0.22	2243208	78.79	74.09	3672	0.31	0.29

Continued from above	Mn area	Mn median-scale	MnO NMS	Fe area	Fe median-scale	Fe_2O_3 NMS	Ba area (50kV scan)	Ba median-scale	$BaSO_4$ NMS
	70163	1.33	2.58	63264	1.06	2.06	4969	0.36	0.70
	85319	1.62	2.94	78807	1.32	2.40	8128	0.59	1.08
	107587	2.04	2.50	84188	1.42	1.73	8279	0.61	0.74
	107115	2.03	2.87	91168	1.53	2.16	7701	0.56	0.79
	90865	1.72	2.09	69925	1.18	1.43	7625	0.56	0.68
	87716	1.66	1.55	64969	1.09	1.02	7805	0.57	0.53
	92933	1.76	1.66	66917	1.12	1.06	7998	0.58	0.55

Table A4 Shipboard medians. Shipboard weight percent and calculated area medians for sedimentary components at each site used in calculating final NMS values. Medians of shipboard data were for all points measured at each site.

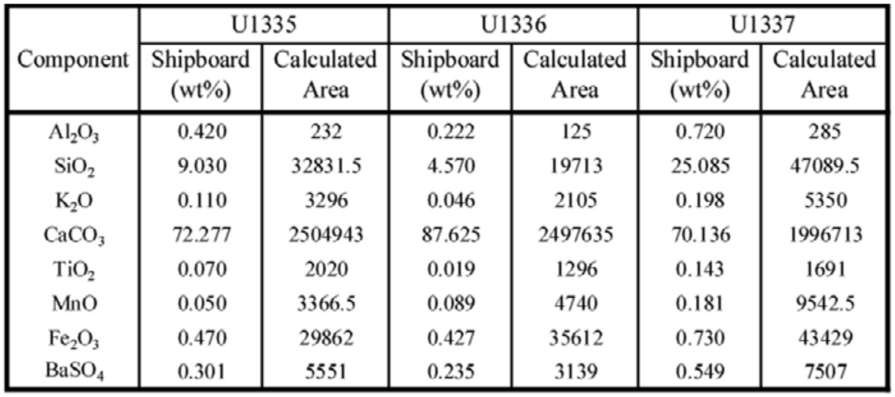

Component	U1335		U1336		U1337	
	Shipboard (wt%)	Calculated Area	Shipboard (wt%)	Calculated Area	Shipboard (wt%)	Calculated Area
Al_2O_3	0.420	232	0.222	125	0.720	285
SiO_2	9.030	32831.5	4.570	19713	25.085	47089.5
K_2O	0.110	3296	0.046	2105	0.198	5350
$CaCO_3$	72.277	2504943	87.625	2497635	70.136	1996713
TiO_2	0.070	2020	0.019	1296	0.143	1691
MnO	0.050	3366.5	0.089	4740	0.181	9542.5
Fe_2O_3	0.470	29862	0.427	35612	0.730	43429
$BaSO_4$	0.301	5551	0.235	3139	0.549	7507

Table A5 U1335, U1336, and U1337 bio- and magnetostratigraphic datums. Age, depth, $CaCO_3$ NMS data, and stratigraphic data are presented and were used to correlate the three sections. Both biostrategraphic and magnetostratigraphic points were used.

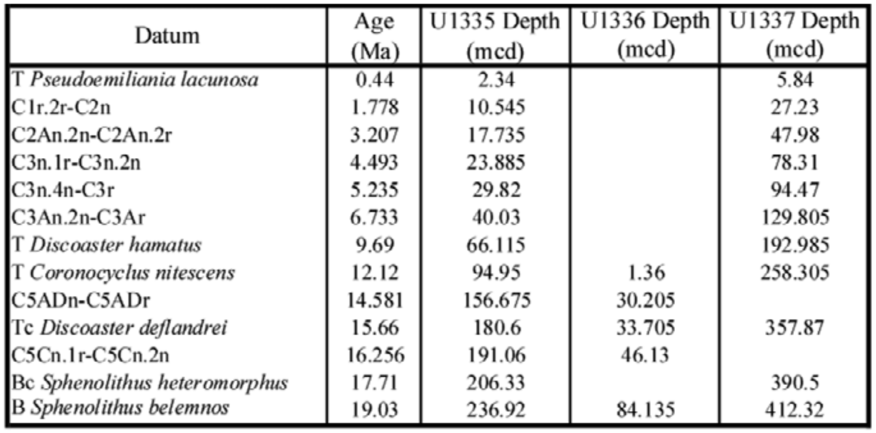

Datum	Age (Ma)	U1335 Depth (mcd)	U1336 Depth (mcd)	U1337 Depth (mcd)
T *Pseudoemiliania lacunosa*	0.44	2.34		5.84
C1r.2r-C2n	1.778	10.545		27.23
C2An.2n-C2An.2r	3.207	17.735		47.98
C3n.1r-C3n.2n	4.493	23.885		78.31
C3n.4n-C3r	5.235	29.82		94.47
C3An.2n-C3Ar	6.733	40.03		129.805
T *Discoaster hamatus*	9.69	66.115		192.985
T *Coronocyclus nitescens*	12.12	94.95	1.36	258.305
C5ADn-C5ADr	14.581	156.675	30.205	
Tc *Discoaster deflandrei*	15.66	180.6	33.705	357.87
C5Cn.1r-C5Cn.2n	16.256	191.06	46.13	
Bc *Sphenolithus heteromorphus*	17.71	206.33		390.5
B *Sphenolithus belemnos*	19.03	236.92	84.135	412.32

`

APPENDIX B

This appendix includes calibrated data tables and calibration figures, as referenced in Chapter III. For the larger data tables, only the first page has been printed and included in this document. The complete tables are available as supplementary Microsoft Excel (.xls) files. Also included in this appendix are the calibration figures referenced in Chapter 3.

Table B1 U1337 geochemical calibration data.

Site, Hole, Core, Type, Section	Depth in section (cm)	Depth (mcd)	^{43}Ca conc.(%)	^{47}Ti conc.(%)	^{55}Mn conc.(%)	^{27}Al conc.(%)	^{56}Fe conc.(%)	Ba conc.(%)	^{232}Th conc.(%)
U1337B-1H-3	45-46	3.045	16.735	0.086	1.470	2.128	1.959	0.611	3.353E-04
U1337C-2H-5	145-146	9.915	8.665	0.098	0.365	2.377	2.302	0.783	3.788E-04
U1337A-3H-4	100-101	15.490	42.173	0.033	1.352	0.941	1.140	0.208	9.231E-05
U1337B-3H-3	50-51	20.690	2.017	0.155	3.279	3.397	3.128	1.336	3.751E-04
U1337B-3H-3	130-131	20.770	24.870	0.038	0.206	1.044	1.010	0.331	1.205E-04
U1337B-3H-4	120-121	22.260	16.249	0.078	0.240	1.932	1.689	0.710	2.251E-04
U1337B-3H-5	35-36	23.675	7.244	0.132	0.330	3.133	2.847	1.040	3.435E-04
U1337B-3H-5	90-91	23.730	29.472	0.029	0.406	0.662	0.745	0.220	9.176E-05
U1337A-4H-5	30-31	26.560	15.773	0.166	0.411	4.363	3.720	--	--
U1337A-5H-3	125-126	35.825	3.881	0.192	0.529	4.781	5.404	1.224	3.462E-04
U1337A-5H-4	70-71	37.270	22.621	0.117	0.837	3.115	3.546	0.888	2.248E-04
U1337B-5H-4	105-106	42.665	16.299	0.073	0.506	1.951	2.111	0.729	1.931E-04
U1337B-5H-5	70-71	44.130	10.729	0.098	0.375	2.256	2.446	1.074	2.285E-04
U1337A-6H-3	60-61	46.390	4.643	0.165	0.687	4.214	4.240	1.256	2.991E-04
U1337B-6H-3	80-81	51.870	19.051	0.072	0.588	1.686	1.759	0.678	1.521E-04
U1337B-6H-5	25-26	54.815	4.418	0.135	0.697	3.088	3.252	1.158	2.758E-04
U1337B-7H-3	40-41	62.430	6.402	0.107	0.395	2.420	2.522	0.940	2.233E-04
U1337B-7H-5	80-81	65.470	1.944	0.116	0.347	2.513	2.422	0.943	2.384E-04
U1337A-8H-2	120-121	67.180	8.810	0.071	0.984	1.580	1.693	0.860	1.976E-04
U1337A-8H-5	10-11	71.570	2.417	0.126	2.837	3.071	2.965	0.924	1.852E-04
U1337A-8H-5	35-36	71.595	4.408	0.113	0.585	2.535	2.189	0.933	1.868E-04

Continued from above

Automate		Difference Method				
%CaCO$_3$	%Carbon	Total-C (wt%)	C$_{org}$ (wt%)	Inorg. C (wt%)	CaCO$_3$ (wt%)	SiO$_2$ (wt%)
39.580	4.750	5.02	0.16	4.86	40.52	18.67
23.530	2.820	3.08	0.21	2.88	23.96	20.40
74.020	8.880	8.57	0.05	8.51	70.94	7.87
3.240	0.390	0.68	0.14	0.54	4.47	17.70
61.640	7.400	7.34	0.13	7.21	60.11	11.90
42.385	5.085	5.24	0.26	4.98	41.47	17.14
16.850	2.020	2.25	0.16	2.09	17.45	24.14
75.760	9.090	9.03	0.09	8.95	74.55	5.20
26.690	3.200	3.57	0.14	3.32	27.70	15.90
5.633	0.678	1.13	0.21	0.92	7.67	27.10
40.220	4.830	6.88	0.14	6.74	56.19	15.90
40.400	4.850	4.94	0.12	4.81	40.10	16.30
27.025	3.240	3.43	0.19	3.24	27.00	24.47
7.410	0.890	3.30	0.19	3.11	25.90	29.85
44.250	5.310	5.49	0.15	5.34	44.51	16.70
8.710	1.040	1.32	0.17	1.14	9.52	24.50
15.510	1.860	1.44	0.21	1.23	10.26	14.53
3.585	0.430	0.76	0.23	0.52	4.37	16.71
30.850	3.700	3.98	0.14	3.84	32.01	19.00
4.775	0.570	1.13	0.29	0.84	6.96	40.62
7.630	0.920	1.26	0.23	1.03	8.61	41.13

Table B2 U1338 geochemical calibration data.

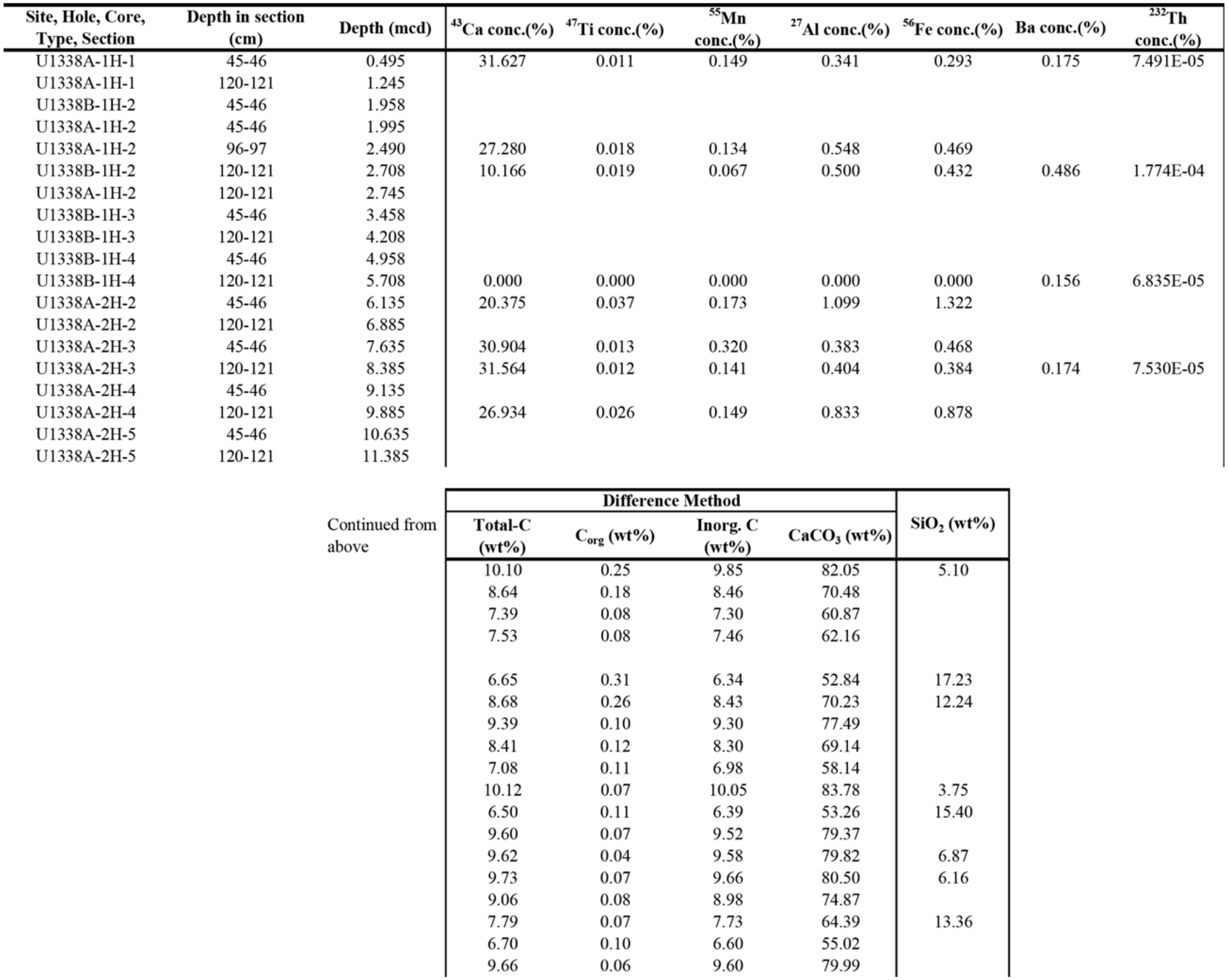

										Difference Method				
Site, Hole, Core, Type, Section	Depth in section (cm)	Depth (mcd)	^{43}Ca conc.(%)	^{47}Ti conc.(%)	^{55}Mn conc.(%)	^{27}Al conc.(%)	^{56}Fe conc.(%)	Ba conc.(%)	^{232}Th conc.(%)	Total-C (wt%)	C_{org} (wt%)	Inorg. C (wt%)	$CaCO_3$ (wt%)	SiO_2 (wt%)
U1338A-1H-1	45-46	0.495	31.627	0.011	0.149	0.341	0.293	0.175	7.491E-05	10.10	0.25	9.85	82.05	5.10
U1338A-1H-1	120-121	1.245								8.64	0.18	8.46	70.48	
U1338B-1H-2	45-46	1.958								7.39	0.08	7.30	60.87	
U1338A-1H-2	45-46	1.995								7.53	0.08	7.46	62.16	
U1338A-1H-2	96-97	2.490	27.280	0.018	0.134	0.548	0.469							
U1338B-1H-2	120-121	2.708	10.166	0.019	0.067	0.500	0.432	0.486	1.774E-04	6.65	0.31	6.34	52.84	17.23
U1338A-1H-2	120-121	2.745								8.68	0.26	8.43	70.23	12.24
U1338B-1H-3	45-46	3.458								9.39	0.10	9.30	77.49	
U1338B-1H-3	120-121	4.208								8.41	0.12	8.30	69.14	
U1338B-1H-4	45-46	4.958								7.08	0.11	6.98	58.14	
U1338B-1H-4	120-121	5.708	0.000	0.000	0.000	0.000	0.000	0.156	6.835E-05	10.12	0.07	10.05	83.78	3.75
U1338A-2H-2	45-46	6.135	20.375	0.037	0.173	1.099	1.322			6.50	0.11	6.39	53.26	15.40
U1338A-2H-2	120-121	6.885								9.60	0.07	9.52	79.37	
U1338A-2H-3	45-46	7.635	30.904	0.013	0.320	0.383	0.468			9.62	0.04	9.58	79.82	6.87
U1338A-2H-3	120-121	8.385	31.564	0.012	0.141	0.404	0.384	0.174	7.530E-05	9.73	0.07	9.66	80.50	6.16
U1338A-2H-4	45-46	9.135								9.06	0.08	8.98	74.87	
U1338A-2H-4	120-121	9.885	26.934	0.026	0.149	0.833	0.878			7.79	0.07	7.73	64.39	13.36
U1338A-2H-5	45-46	10.635								6.70	0.10	6.60	55.02	
U1338A-2H-5	120-121	11.385								9.66	0.06	9.60	79.99	

Continued from above

Table B3 Calibrated U1335 XRF $CaCO_3$ NMS data.

Site, Hole, Core, Type, Section	Depth in section (mm)	Depth (mcd)	Ca Peak Area	$CaCO_3$ NMS	Estimated wt% $CaCO_3$
U1335B-1H-1	25	0.025	994545	78.260	74.202
U1335B-1H-1	50	0.050	859703	79.097	74.962
U1335B-1H-1	75	0.075	1054422	83.340	78.814
U1335B-1H-1	100	0.100	1329295	84.175	79.572
U1335B-1H-1	125	0.125	1367729	83.852	79.278
U1335B-1H-1	150	0.150	1336621	84.412	79.787
U1335B-1H-1	175	0.175	1909932	84.346	79.727
U1335B-1H-1	200	0.200	2057120	82.938	78.449
U1335B-1H-1	225	0.225	2082424	84.730	80.076
U1335B-1H-1	250	0.250	2316819	88.519	83.515
U1335B-1H-1	275	0.275	2180242	87.012	82.147
U1335B-1H-1	300	0.300	2184040	89.287	84.212
U1335B-1H-1	325	0.325	2021388	88.884	83.846
U1335B-1H-1	350	0.350	2406030	88.261	83.281
U1335B-1H-1	375	0.375	2273298	88.431	83.435
U1335B-1H-1	400	0.400	2199505	87.507	82.596
U1335B-1H-1	425	0.425	1980958	86.829	81.981
U1335B-1H-1	450	0.450	2125369	87.276	82.387
U1335B-1H-1	475	0.475	2027864	85.643	80.904
U1335B-1H-1	500	0.500	1507268	86.811	81.965
U1335B-1H-1	525	0.525	1501313	84.003	79.415
U1335B-1H-1	550	0.550	1405079	82.246	77.820
U1335B-1H-1	575	0.575	1190689	79.785	75.587
U1335B-1H-1	600	0.600	1265882	73.082	69.502
U1335B-1H-1	625	0.625	1208552	78.256	74.198
U1335B-1H-1	650	0.650	810248	63.393	60.707
U1335B-1H-1	675	0.675	1098394	68.645	65.475
U1335B-1H-1	700	0.700	719205	57.613	55.460
U1335B-1H-1	725	0.725	1038160	66.027	63.099
U1335B-1H-1	750	0.750	760517	49.219	47.842
U1335B-1H-1	775	0.775	703200	44.206	43.290
U1335B-1H-1	800	0.800	1045778	57.216	55.100
U1335B-1H-1	825	0.825	766718	50.224	48.753
U1335B-1H-1	850	0.850	602203	43.643	42.780
U1335B-1H-1	875	0.875	457966	53.046	51.315
U1335B-1H-1	900	0.900	451524	54.826	52.931
U1335B-1H-1	925	0.925	521146	41.206	40.568
U1335B-1H-1	950	0.950	340163	44.566	43.618
U1335B-1H-1	975	0.975	867837	55.814	53.828
U1335B-1H-1	1000	1.000	1204847	64.930	62.103
U1335B-1H-1	1025	1.025	1721048	76.216	72.347
U1335B-1H-1	1050	1.050	1787486	78.690	74.593
U1335B-1H-1	1075	1.075	883024	64.609	61.811
U1335B-1H-1	1100	1.100	1771131	78.734	74.633
U1335B-1H-1	1125	1.125	2018830	81.900	77.507
U1335B-1H-1	1150	1.150	2156385	81.185	76.858
U1335B-1H-1	1175	1.175	1974244	81.851	77.462
U1335B-1H-1	1200	1.200	1868958	81.897	77.504
U1335B-1H-1	1225	1.225	1885907	79.309	75.155
U1335B-1H-1	1250	1.250	1510317	74.015	70.349

Table B4 Calibrated U1336 XRF CaCO$_3$ NMS data.

Site, Hole, Core, Type, Section	Depth in section (mm)	Depth (mcd)	Ca Peak Area	CaCO$_3$ NMS	Estimated w CaCO$_3$
U1336B-1H-1	25	0.025	167300	69.474	51.176
U1336B-1H-1	50	0.050	460791	73.544	57.113
U1336B-1H-1	75	0.075	340413	77.460	62.826
U1336B-1H-1	100	0.100	351910	75.395	59.814
U1336B-1H-1	125	0.125	369816	73.675	57.304
U1336B-1H-1	150	0.150	368041	69.392	51.055
U1336B-1H-1	175	0.175	894127	83.314	71.365
U1336B-1H-1	200	0.200	963970	83.277	71.311
U1336B-1H-1	225	0.225	1138167	83.166	71.150
U1336B-1H-1	250	0.250	1298467	85.310	74.277
U1336B-1H-1	275	0.275	1356017	84.804	73.539
U1336B-1H-1	300	0.300	1586750	88.776	79.333
U1336B-1H-1	325	0.325	1785079	89.465	80.339
U1336B-1H-1	350	0.350	1799238	89.669	80.636
U1336B-1H-1	375	0.375	1344254	87.641	77.678
U1336B-1H-1	425	0.425	1282903	86.853	76.528
U1336B-1H-1	450	0.450	1349089	84.177	72.625
U1336B-1H-1	475	0.475	1381994	83.089	71.038
U1336B-1H-1	500	0.500	1307998	82.782	70.590
U1336B-1H-1	525	0.525	1362761	85.780	74.963
U1336B-1H-1	550	0.550	1452745	85.114	73.991
U1336A-1H-1	300	0.560	1337571	82.559	70.265
U1336A-1H-1	325	0.585	1421315	83.859	72.160
U1336A-1H-1	350	0.610	1649045	87.046	76.810
U1336A-1H-1	375	0.635	1693713	88.133	78.395
U1336A-1H-1	400	0.660	1725763	87.956	78.137
U1336A-1H-1	425	0.685	1791309	88.799	79.367
U1336A-1H-1	450	0.710	1739634	89.469	80.345
U1336A-1H-1	475	0.735	1517922	89.519	80.418
U1336A-1H-1	500	0.760	1453492	88.043	78.264
U1336A-1H-1	525	0.785	1598018	88.854	79.447
U1336A-1H-1	550	0.810	1653555	88.853	79.445
U1336A-1H-1	575	0.835	2109187	89.732	80.728
U1336A-1H-1	600	0.860	2021699	89.518	80.416
U1336A-1H-1	625	0.885	2073789	90.221	81.442
U1336A-1H-1	650	0.910	1957972	88.787	79.349
U1336A-1H-1	675	0.935	1947303	88.797	79.364
U1336A-1H-1	700	0.960	1859382	88.015	78.223
U1336A-1H-1	725	0.985	1761734	88.346	78.706
U1336A-1H-1	750	1.010	1925020	88.408	78.797
U1336A-1H-1	775	1.035	1961058	87.223	77.067
U1336A-1H-1	800	1.060	2022278	87.190	77.019
U1336A-1H-1	825	1.085	2097671	87.537	77.526
U1336A-1H-1	850	1.110	2061028	89.027	79.700
U1336A-1H-1	875	1.135	1549211	87.217	77.059
U1336A-1H-1	900	1.160	1638078	89.063	79.752
U1336A-1H-1	925	1.185	1588063	88.615	79.099
U1336A-1H-1	950	1.210	1587647	87.433	77.374
U1336A-1H-1	975	1.235	1800894	84.226	72.696
U1336A-1H-1	1000	1.260	1791549	83.716	71.953

Table B5 Calibrated U1337 XRF NMS data.

Site, Hole, Core, Type, Section	Depth in section (mm)	Depth (mcd)	Age (Ma)	Al Peak Area	Al_2O_3 NMS	Estimated wt% Al_2O_3	Ba Peak Area	$BaSO_4$ NMS	Estimated wt% $BaSO_4$
U1337B-1H-1	25	0.025	0.001	280	1.372	1.359	4969	0.705	1.119
U1337B-1H-1	50	0.050	0.002	-59	0.000	0.000	8128	1.079	1.625
U1337B-1H-1	75	0.075	0.003	229	0.708	0.701	8279	0.741	1.167
U1337B-1H-1	100	0.100	0.005	404	1.440	1.427	7701	0.795	1.241
U1337B-1H-1	125	0.125	0.006	-146	0.000	0.000	7625	0.677	1.081
U1337B-1H-1	150	0.150	0.007	242	0.568	0.563	7805	0.531	0.883
U1337B-1H-1	175	0.175	0.008	101	0.240	0.238	7998	0.550	0.910

Continued from above

Ca Peak Area	$CaCO_3$ NMS	Estimated wt% $CaCO_3$	Fe Peak Area	Fe_2O_3 NMS	Estimated wt% Fe_2O_3
924467	62.993	62.837	63264	2.063	1.869
1062665	67.726	67.260	78807	2.404	2.130
1601528	68.805	68.267	84188	1.731	1.603
1227550	60.841	60.826	91168	2.162	1.946
1696157	72.328	71.560	69925	1.427	1.350
2306080	75.297	74.334	64969	1.015	0.988
2243208	74.089	73.206	66917	1.058	1.026

Continued from above

MnO Peak Area	MnO NMS	Estimated wt% MnO	Si Peak Area	SiO_2 NMS	Estimated wt% Total SiO_2	Estimated wt% Bio-SiO_2
70163	2.582	1.476	28368	29.316	16.332	10.028
85319	2.936	1.584	25856	24.991	14.096	9.456
107587	2.496	1.448	38038	24.784	13.988	10.041
107115	2.867	1.564	41109	30.900	17.152	11.229
90865	2.092	1.304	35381	22.881	13.004	9.459
87716	1.547	1.072	41586	20.593	11.821	8.918
92933	1.657	1.123	43714	21.896	12.495	9.269

Continued from above

TiO_2 Peak Area	TiO_2 NMS	Estimated wt% TiO_2
3726	0.611	0.082
2858	0.439	0.060
3546	0.367	0.051
4791	0.572	0.077
3166	0.325	0.046
3287	0.258	0.038
3672	0.292	0.042

Table B6 Calibrated U1338 XRF NMS data.

Site, Hole, Core, Type, Section	Depth in section (mm)	Depth (mcd)	Al Peak Area	Al_2O_3 NMS	Estimated wt% Al_2O_3	Ba Peak Area	$BaSO_4$ NMS	Estimated wt% $BaSO_4$	Ca Peak Area	$CaCO_3$ NMS	Estimated wt% $CaCO_3$	Fe Peak Area	Fe_2O_3 NMS	Estimated wt% Fe_2O_3	MnO Peak Area	MnO NMS	Estimated wt% MnO	Si Peak Area	SiO_2 NMS	Estimated wt% Total SiO_2	Estimated wt% Bio-SiO_2	TiO_2 Peak Area	TiO_2 NMS	Estimated wt% TiO_2
U1338A-1H-1	25	0.065	-196	0.000	0.000	3398	0.381	0.326	2258381	87.281	81.481	50683	1.382	0.813	65711	1.576	0.503	31096	9.376	8.671	7.470	1320	0.003	0.016
U1338A-1H-1	50	0.090	-98	0.000	0.000	12199	1.040	0.918	2914316	85.551	79.709	90042	1.865	1.049	114737	2.090	0.540	39489	9.044	8.401	6.540	3180	0.006	0.024
U1338A-1H-1	75	0.115	31	0.014	0.023	10974	0.704	0.616	3917938	86.555	80.737	89287	1.392	0.818	120200	1.648	0.510	54291	9.357	8.656	6.766	4312	0.006	0.024
U1338A-1H-1	100	0.140	-64	0.000	0.000	9940	0.639	0.557	3879549	85.815	79.980	90977	1.420	0.832	120278	1.651	0.510	58567	10.107	9.266	7.436	4132	0.006	0.024
U1338A-1H-1	125	0.165	261	0.087	0.141	10158	0.467	0.403	5529714	87.539	81.744	90424	1.010	0.616	150111	1.475	0.494	74200	9.164	8.499	6.725	5545	0.006	0.023
U1338A-1H-1	150	0.190	474	0.155	0.251	9623	0.435	0.374	5459765	84.955	79.098	94039	1.033	0.629	116935	1.129	0.454	99029	12.021	10.825	9.259	4785	0.005	0.020
U1338A-1H-1	175	0.215	294	0.096	0.155	9972	0.449	0.387	5622123	87.256	81.454	87932	0.963	0.590	148228	1.428	0.489	79255	9.596	8.851	7.186	5203	0.005	0.022

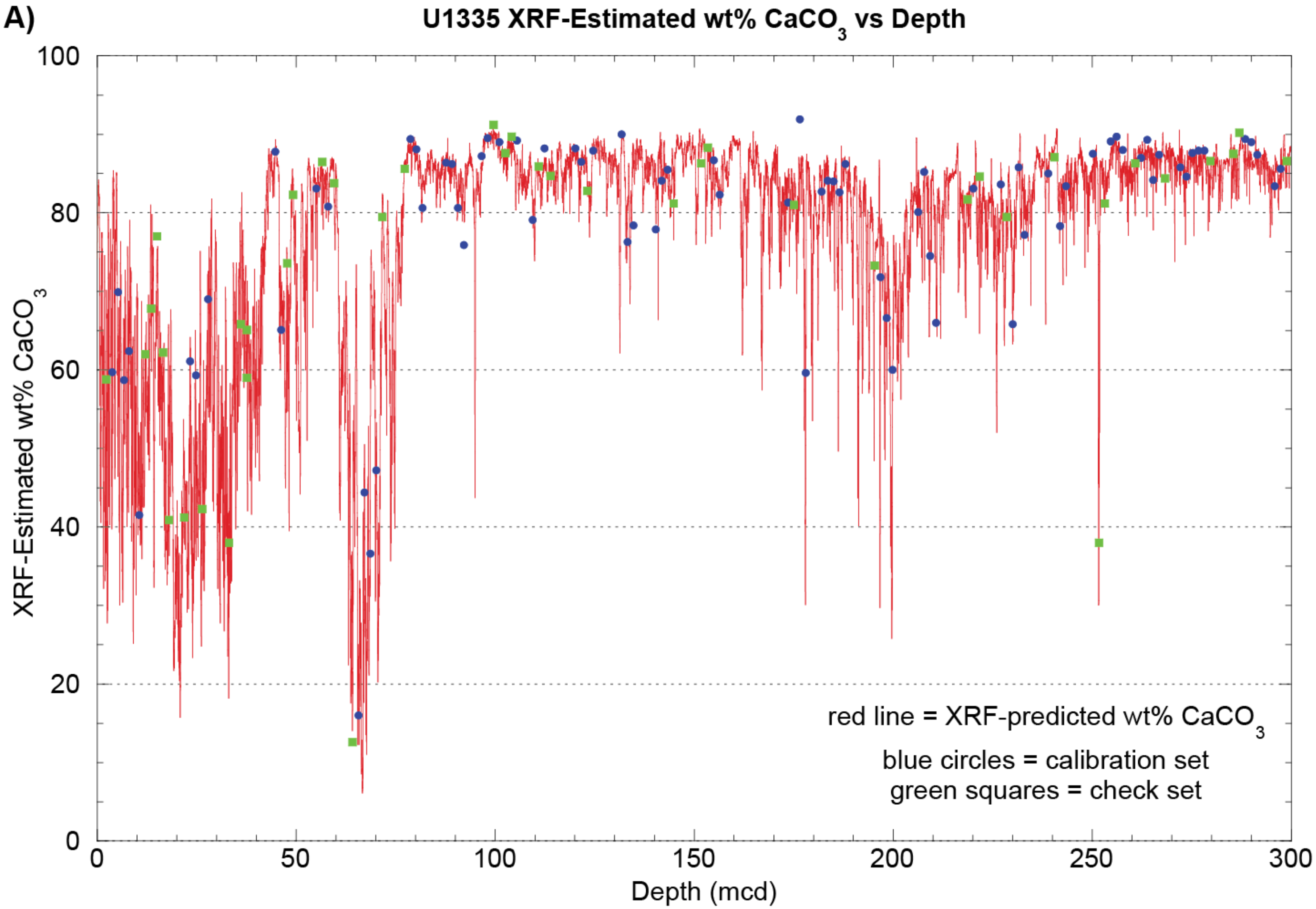

Figure B1 U1335 $CaCO_3$ NMS calibration. Calibration of U1335 $CaCO_3$ NMS data using shipboard geochemical data [*Expedition 320/321 Scientists*, 2010a). A) XRF-predicted wt% $CaCO_3$ versus depth with calibration and check data sets included.

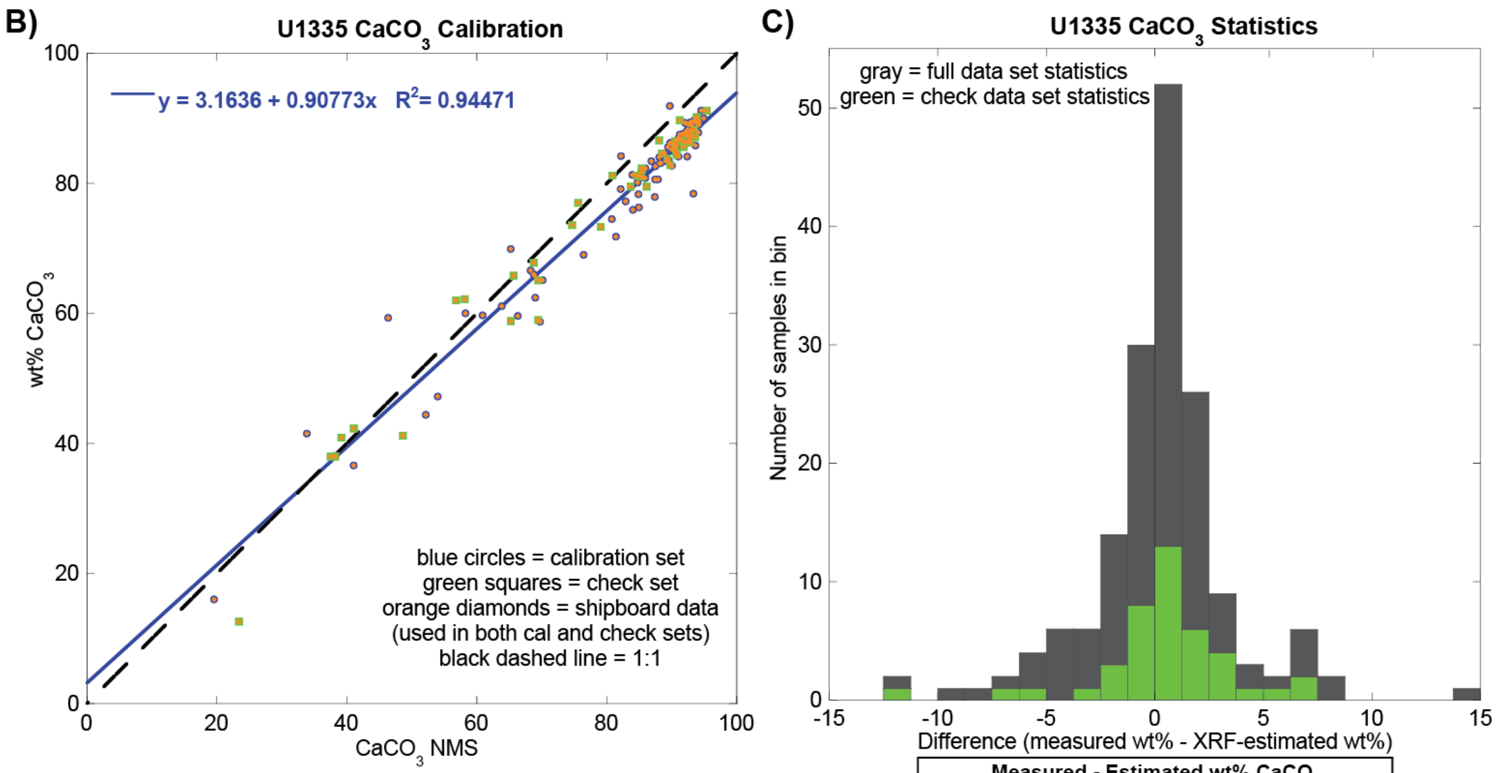

Measured - Estimated wt% $CaCO_3$		
	Full Data Set	**Check Data Set**
Minimum	-11.813	-11.813
Maximum	14.049	7.255
Sum	13.924	13.906
Points	125	42
Mean	0.111	0.331
Median	0.375	0.449
RMS	3.305	3.342
Std Deviation	3.317	3.366
Variance	11.000	11.328
Std Error	0.297	0.519
Skewness	0.066	-1.117
Kurtosis	3.512	3.196

Figure B1 (cont) U1335 $CaCO_3$ NMS calibration (cont). B) Calibration curve: A total of 125 discrete samples were used, 83 as the calibration set and 42 as the check set. A linear relationship was found between the $CaCO_3$ NMS and wt% $CaCO_3$ data, with a correlation of R2 = 0.94471. C) Statistics for the full and check data sets

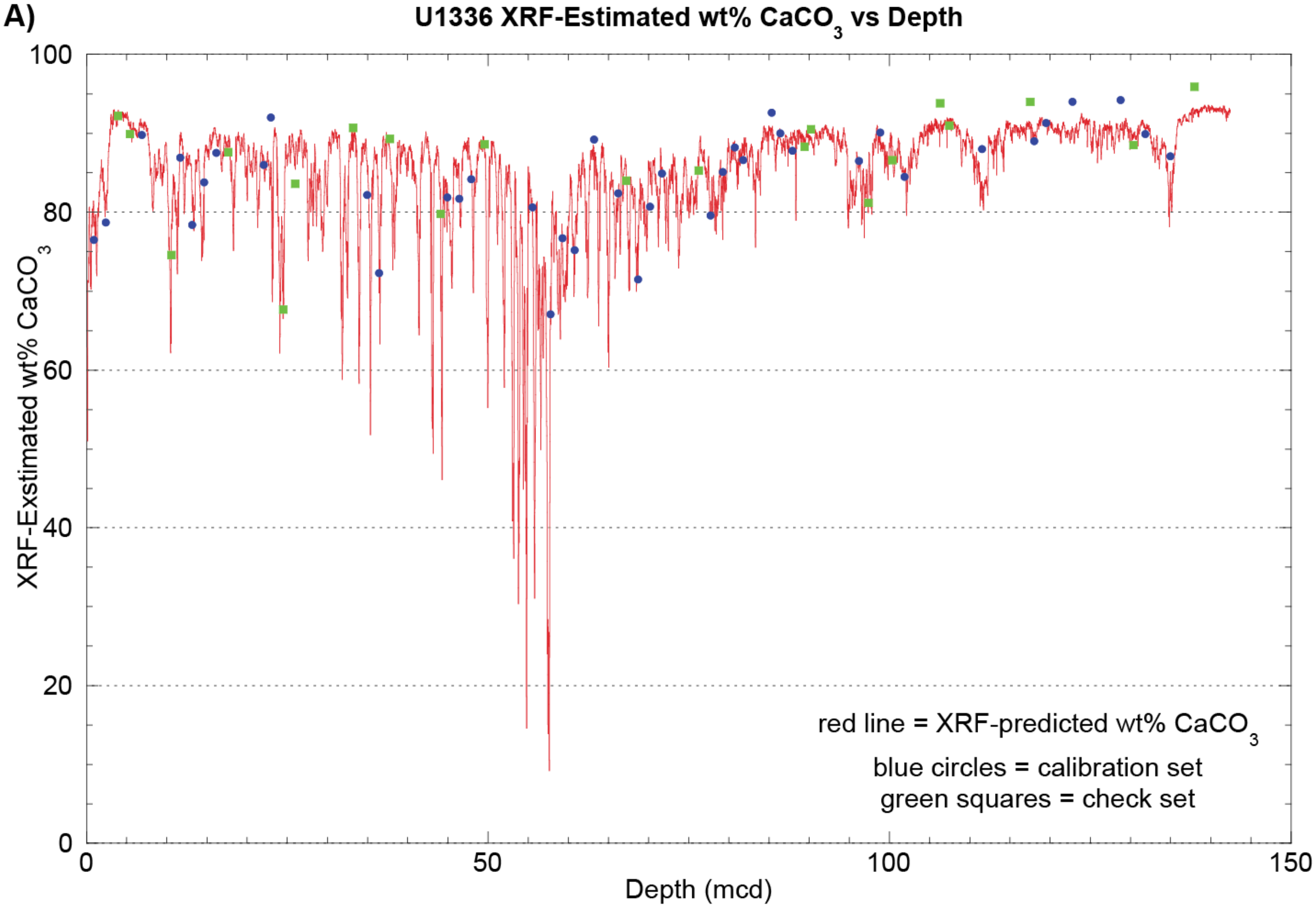

Figure B2 U1336 $CaCO_3$ NMS calibration. Calibration of U1336 $CaCO_3$ NMS data using shipboard geochemical data [*Expedition 320/321 Scientists*, 2010b]. A) XRF-predicted wt% $CaCO_3$ versus depth with calibration and check data sets included.

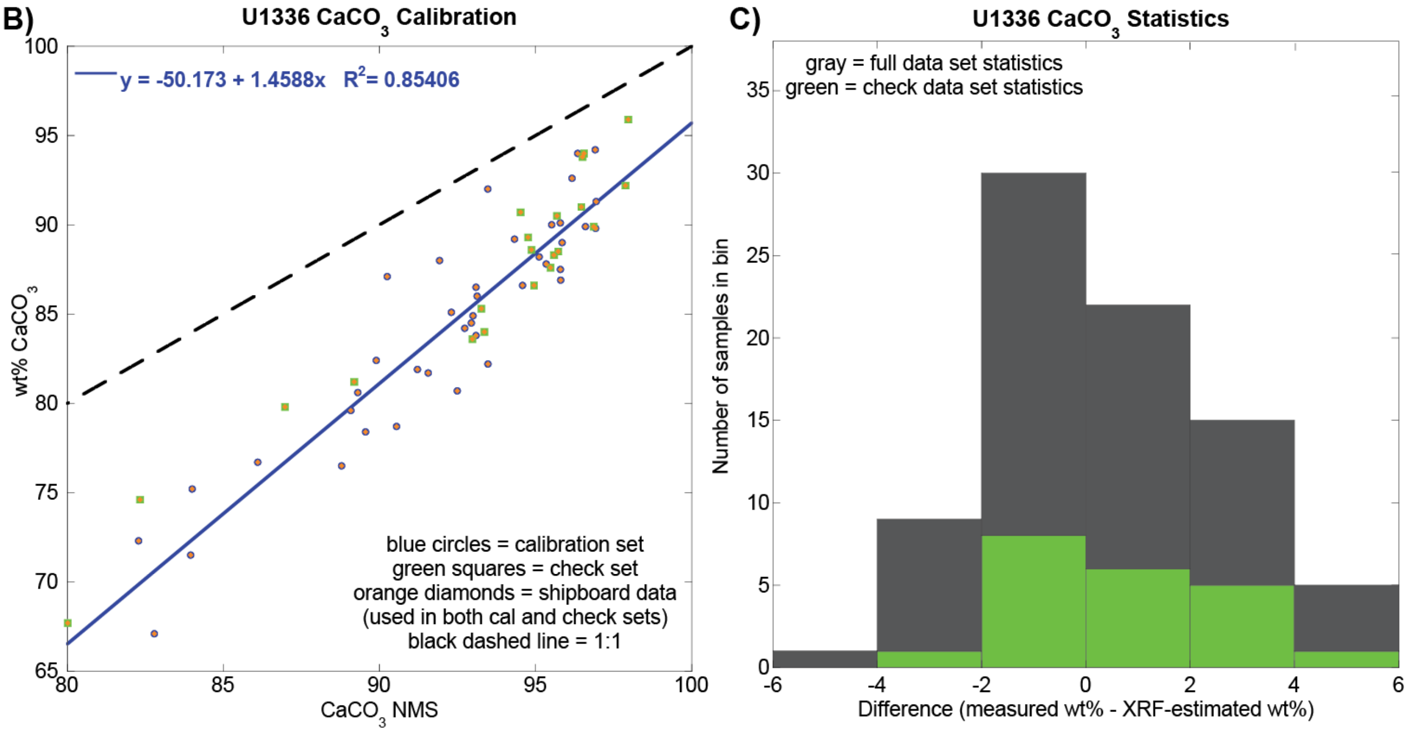

Measured - Estimated wt% CaCO$_3$		
	Full Data Set	Check Data Set
Minimum	-4.054	-2.023
Maximum	5.816	4.666
Sum	14.745	14.667
Points	61	21
Mean	0.242	0.698
Median	-0.183	0.447
RMS	2.299	2.118
Std Deviation	2.305	2.049
Variance	5.314	4.198
Std Error	0.295	0.447
Skewness	0.409	0.326
Kurtosis	-0.352	-1.148

Figure B2 (cont) U1336 CaCO$_3$ NMS calibration (cont). B) Calibration curve: A total of 61 discrete samples were used, 40 as the calibration set and 21 as the check set. A linear relationship was found between the CaCO$_3$ NMS and wt% CaCO$_3$ data, with a correlation of R^2 = 0.85406. C) Statistics for the full and check data sets.

`

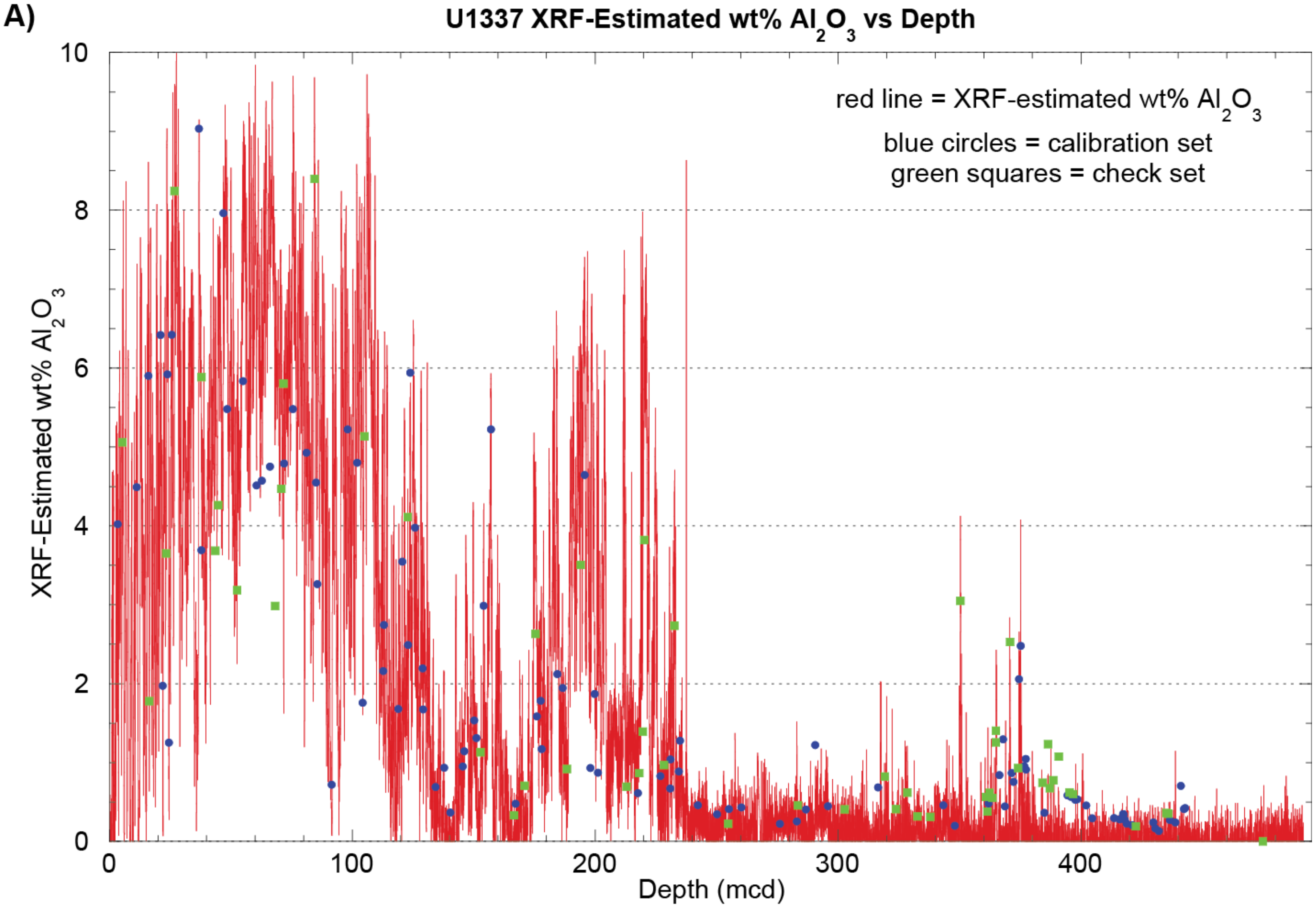

Figure B3 U1337 Al_2O_3 NMS calibration. Calibration of U1337 Al_2O_3 NMS data using shipboard geochemical data [*Expedition 320/321 Scientists*, 2010c] and discrete samples analyzed post-cruise at Texas A&M University. A) XRF-predicted wt% Al_2O_3 versus depth with calibration and check data sets included.

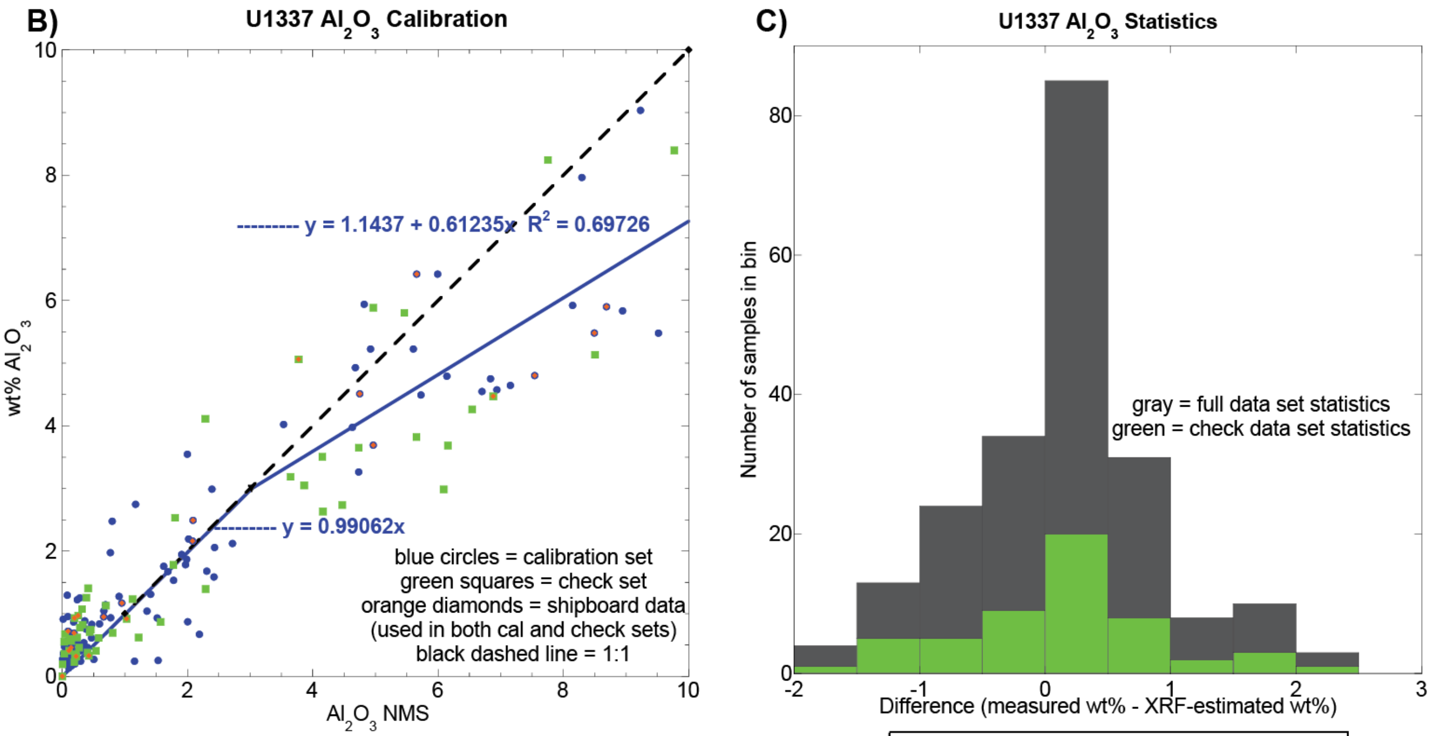

Figure B3 (cont) U1337 Al_2O_3 NMS calibration (cont). B) Calibration curve: A total of 158 discrete samples were used, 104 as the calibration set and 54 as the check set. Two linear relationships were found between the Al_2O_3 NMS and wt% Al_2O_3 data. The best-fit line for the lower portion of data was forced through zero. This line intersects at NMS = 3.023342; wt% = 2.994983 with the best-fit line for the upper portion of data, which has a correlation of $R^2 = 0.69726$. C) Statistics for the full and check data sets.

Measured - Estimated wt% Al_2O_3

	Full Data Set	Check Data Set
Minimum	-1.888	0
Maximum	2.352	7.127
Sum	22.836	100.834
Points	158	54
Mean	0.145	1.867
Median	0.170	0.632
RMS	0.758	2.765
Std Deviation	0.746	2.058
Variance	0.557	4.237
Std Error	0.059	0.280
Skewness	0.052	0.888
Kurtosis	0.685	-0.563

`

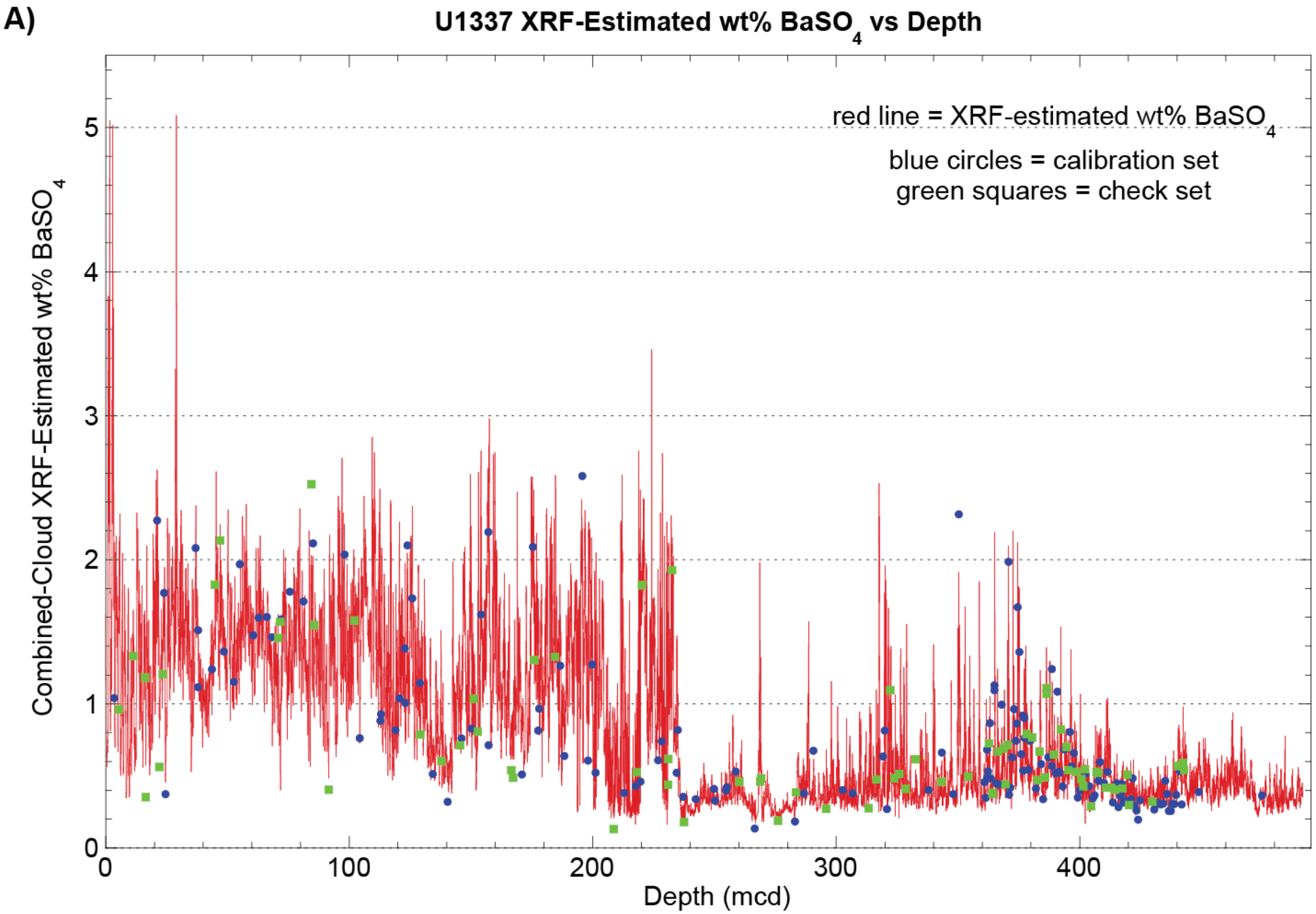

Figure B4 U1337 BaSO4 NMS calibration. Calibration of U1337 $BaSO_4$ NMS data using shipboard geochemical data [*Expedition 320/321 Scientists,* 2010c] and discrete samples analyzed post-cruise at Texas A&M University. A) XRF-predicted wt% $BaSO_4$ versus depth with calibration and check data sets included.

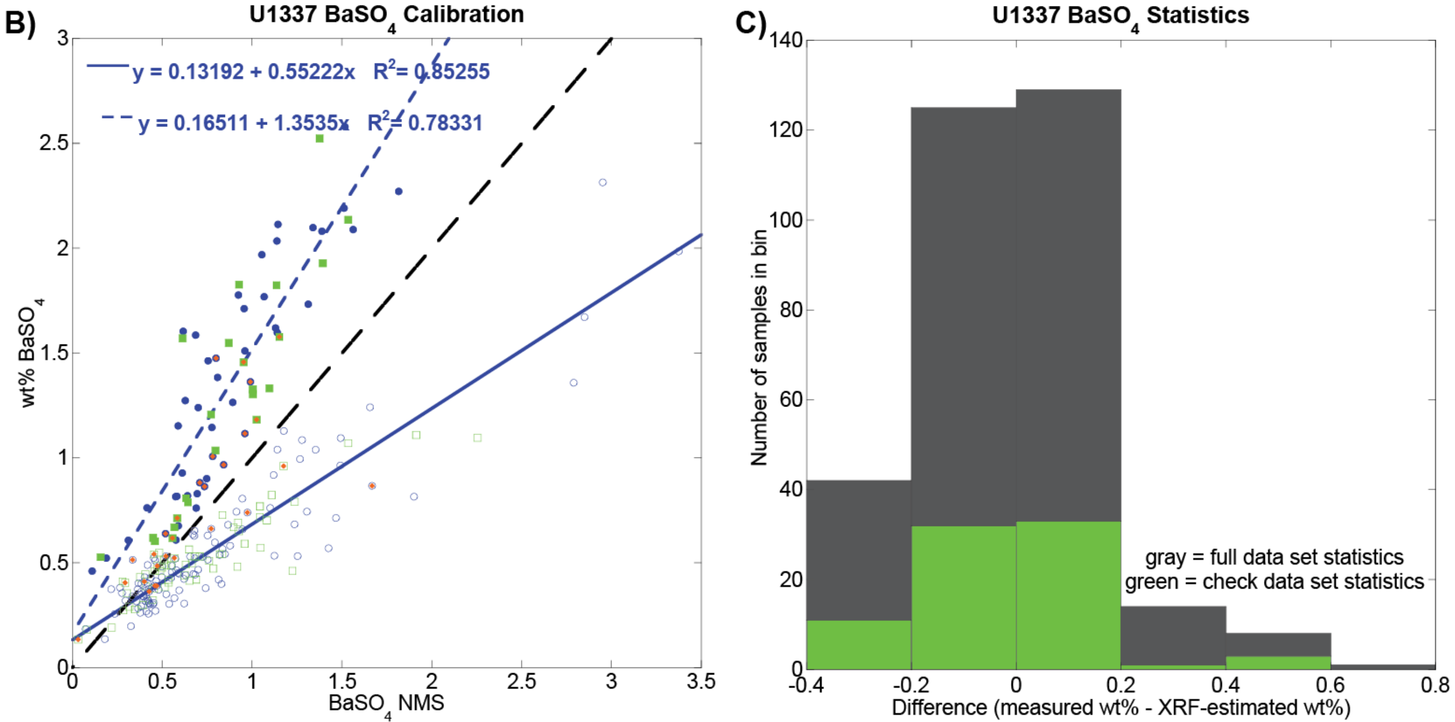

open blue circles = lower cloud calibration set
closed blue circles = upper cloud calibration set
open green squares = lower cloud check set
closed green squares = upper cloud check set
orange diamonds = shipboard data (used in both calibration and check sets)
black dashed line = 1:1

Figure B4 (cont) U1337 BaSO4 NMS calibration (cont).
B) Calibration curve: A total of 239 discrete samples were used, 159 as the calibration set and 80 as the check set. When plotted, data form two distinct clouds with their own best-fit lines. The correlation for the lower data cloud has an $R^2 = 0.85255$ while the correlation for the upper data cloud has an $R^2 = 0.78331$. C) Statistics for the full and check data sets.

Measured - Estimated wt% $BaSO_4$		
	Full Data Set	**Check Data Set**
Minimum	-0.371	-0.371
Maximum	0.603	0.574
Sum	-1.087	-1.088
Points	239	80
Mean	-0.005	-0.014
Median	-0.006	-0.008
RMS	0.171	0.164
Std Deviation	0.171	0.164
Variance	0.029	0.027
Std Error	0.011	0.018
Skewness	0.516	0.631
Kurtosis	1.387	2.206

`

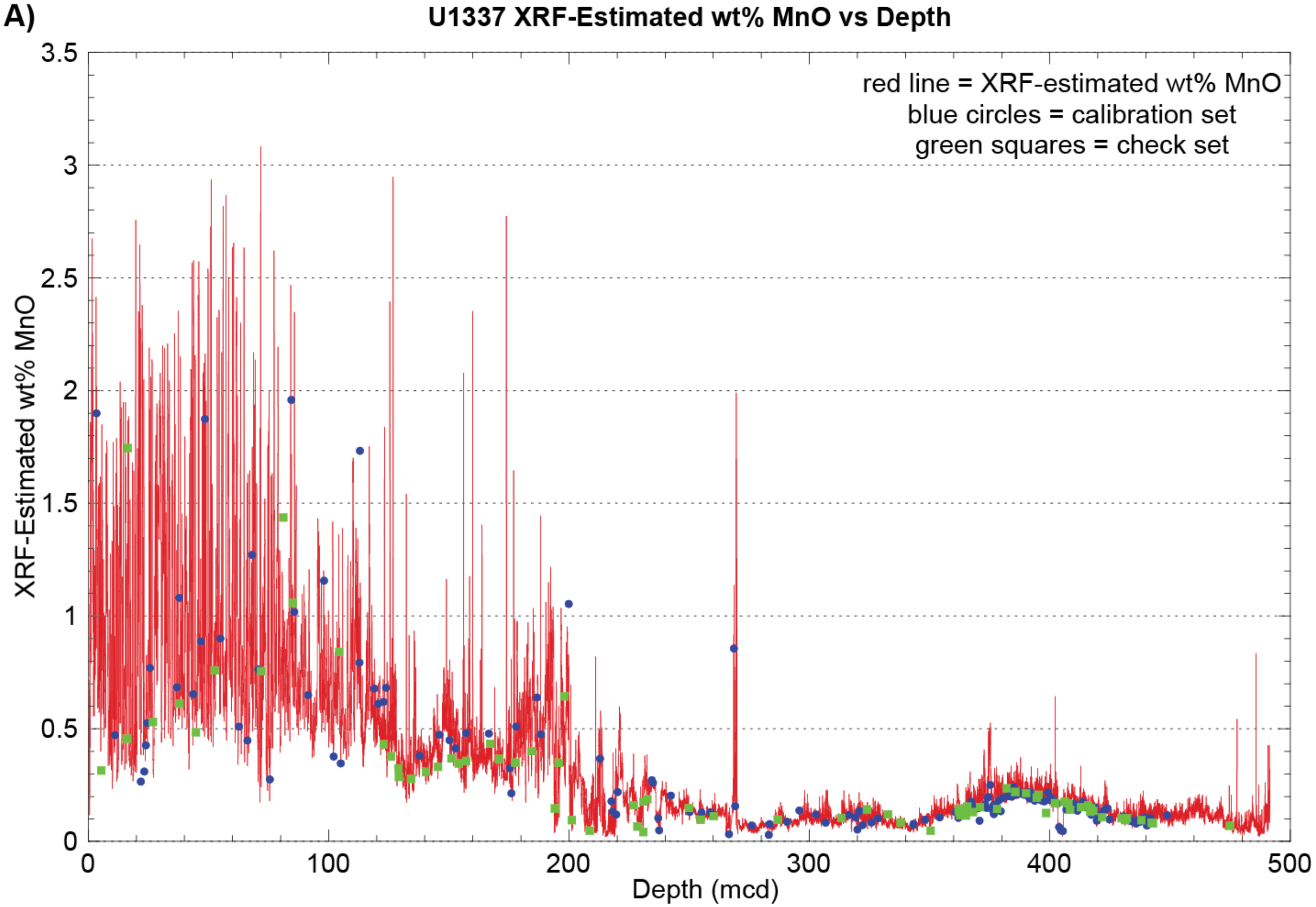

Figure B5 U1337 MnO NMS calibration. Calibration of U1337 MnO NMS data using shipboard geochemical data [*Expedition 320/321 Scientists*, 2010c] and discrete samples analyzed post-cruise at Texas A&M University. A) XRF-predicted wt% MnO versus depth with calibration and check data sets included.

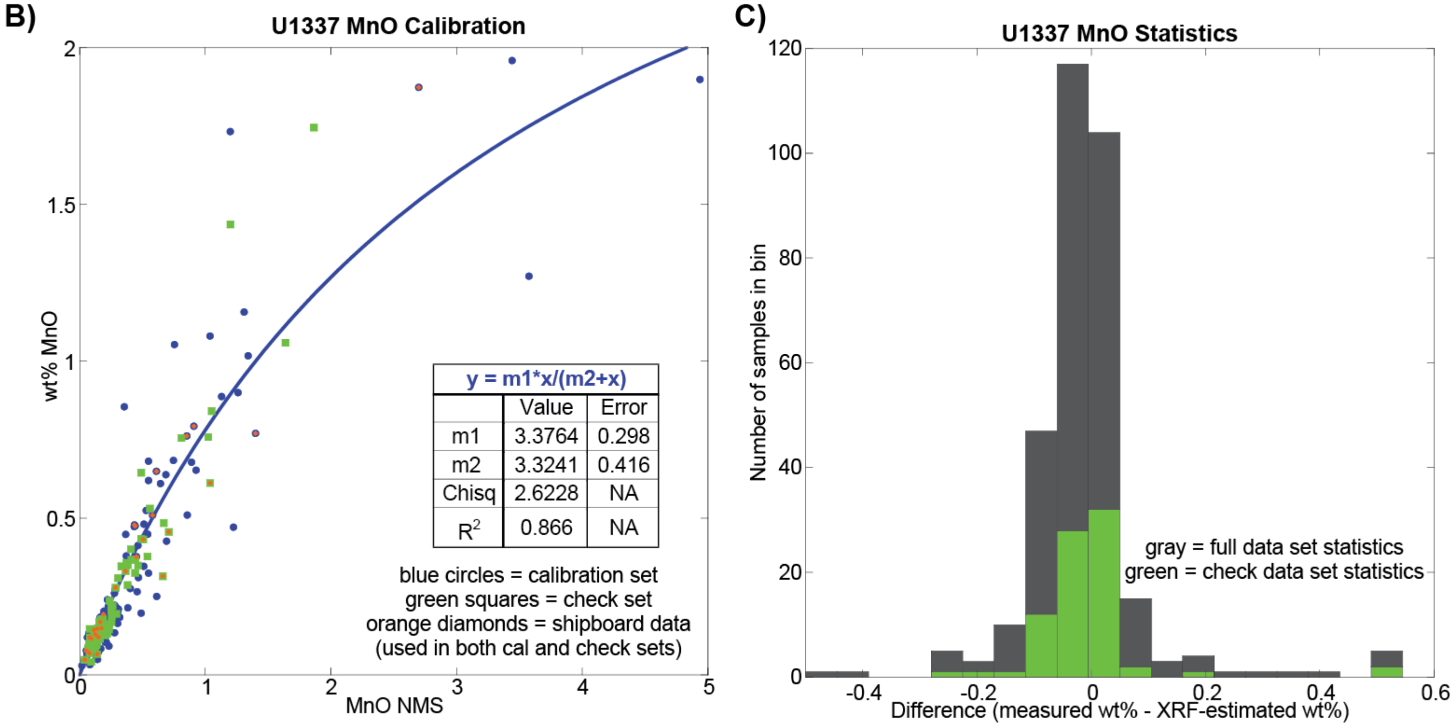

y = m1*x/(m2+x)		
	Value	Error
m1	3.3764	0.298
m2	3.3241	0.416
Chisq	2.6228	NA
R^2	0.866	NA

Figure B5 (cont) U1337 MnO NMS calibration (cont). B) Calibration curve: A total of 240 discrete samples were used, 160 as the calibration set and 80 as the check set. The data do not follow a linear trend, rather the Michaelis-Menten equation was used to determine the best fit and predict wt% MnO. The $R^2 = 0.86559$. C) Statistics for the full and check data sets.

Measured - Estimated wt% MnO		
	Full Data Set	**Check Data Set**
Minimum	-0.479	-0.246
Maximum	0.837	0.541
Sum	-2.116	-0.383
Points	240	80
Mean	-0.009	-0.005
Median	-0.017	-0.010
RMS	0.120	0.103
Std Deviation	0.120	0.104
Variance	0.014	0.011
Std Error	0.008	0.012
Skewness	2.457	3.430
Kurtosis	16.027	16.768

`

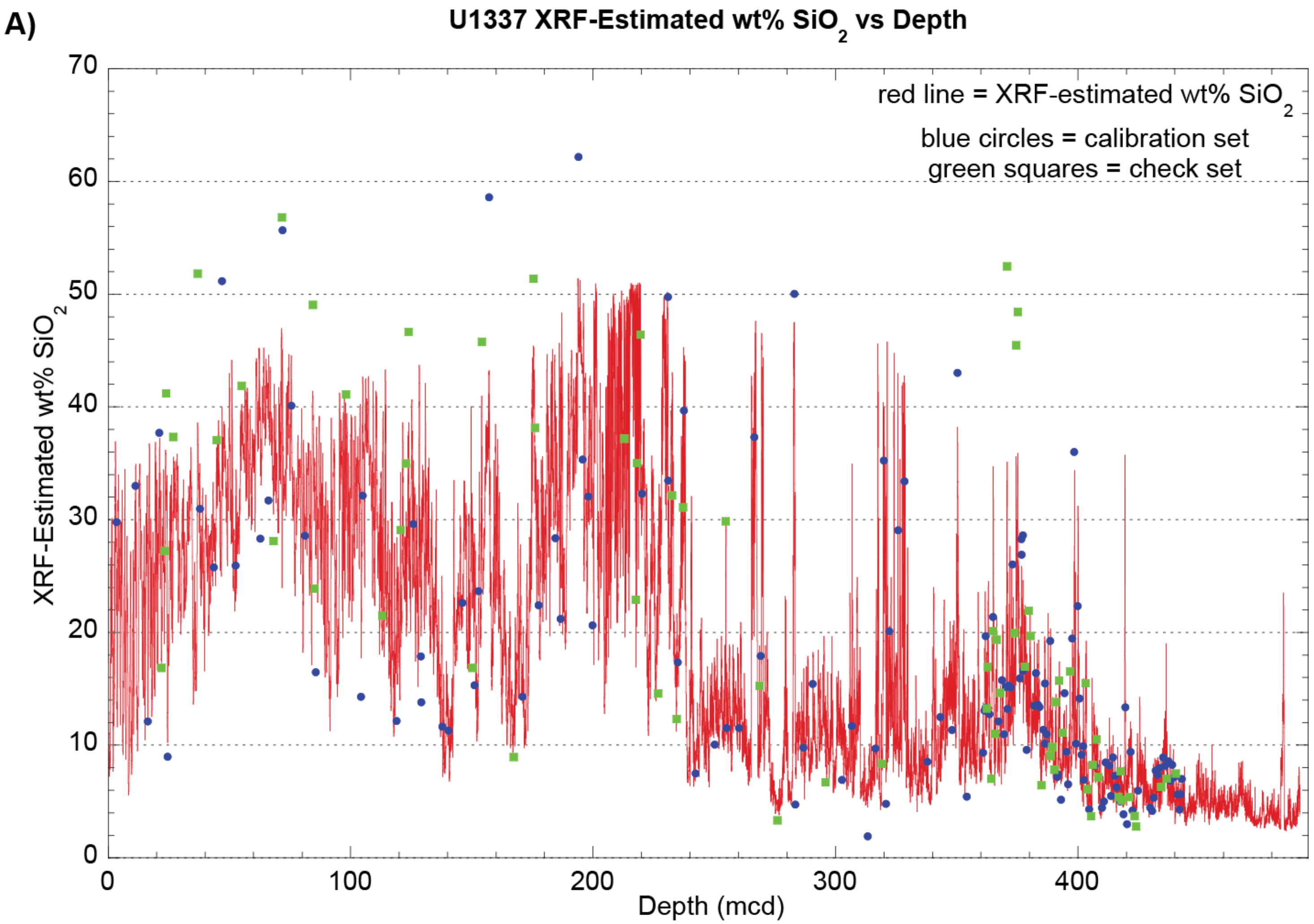

Figure B6 U1337 SiO_2 NMS calibration. Calibration of U1337 SiO_2 NMS data using discrete samples analyzed post-cruise at Texas A&M University. A) XRF-predicted wt% SiO_2 versus depth with calibration and check data sets included.

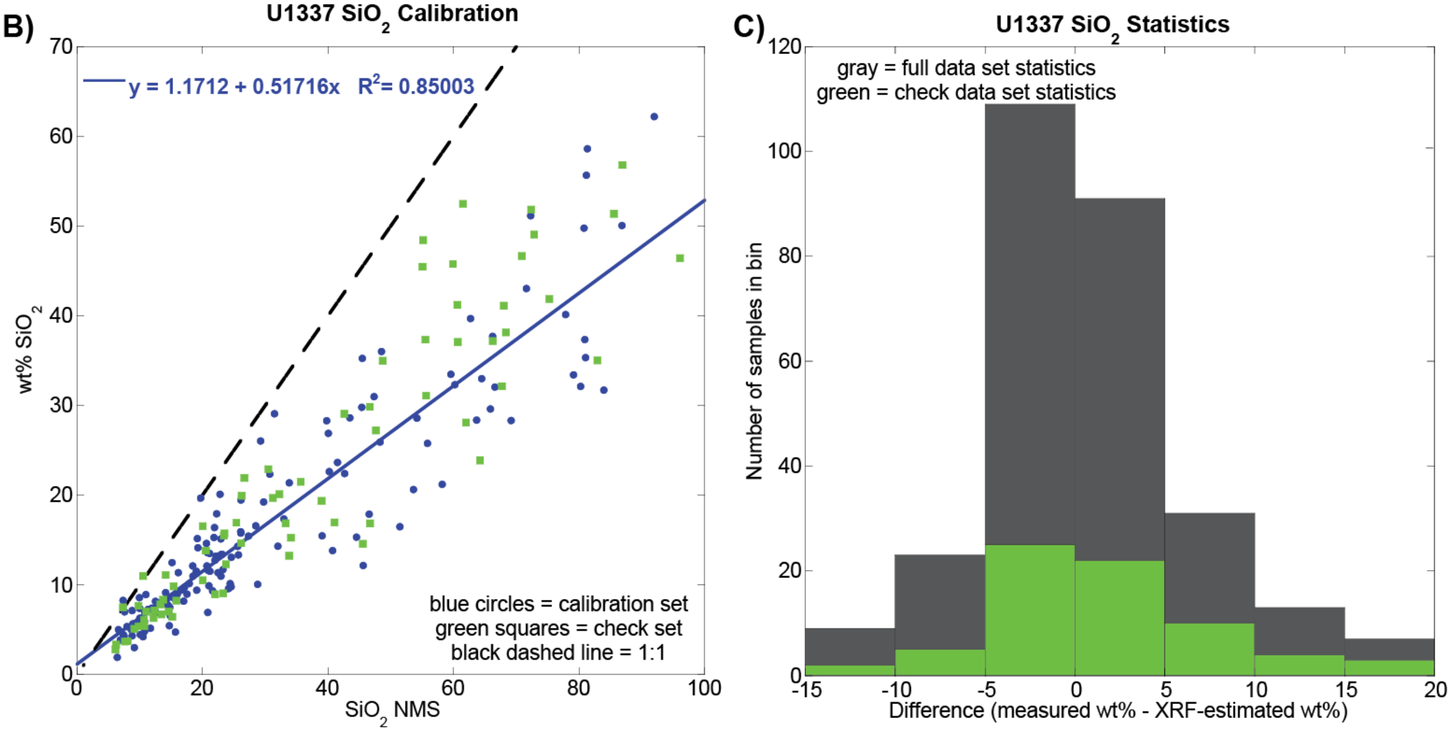

Figure B6 (cont) U1337 SiO_2 NMS calibration (cont). B) Calibration curve: A total of 212 discrete samples were used, 141 as the calibration set and 71 as the check set. A linear relationship was found between the SiO_2 NMS and wt% SiO_2 data, with a correlation of R^2 = 0.85003. C) Statistics for the full and check data sets.

Measured - Estimated wt% SiO_2		
	Full Data Set	**Check Data Set**
Minimum	-12.921	-10.518
Maximum	19.477	19.477
Sum	119.215	121.155
Points	212	71
Mean	0.562	1.706
Median	-0.071	1.121
RMS	5.354	6.230
Std Deviation	5.337	6.034
Variance	28.486	36.411
Std Error	0.367	0.716
Skewness	0.578	0.737
Kurtosis	1.527	0.965

`

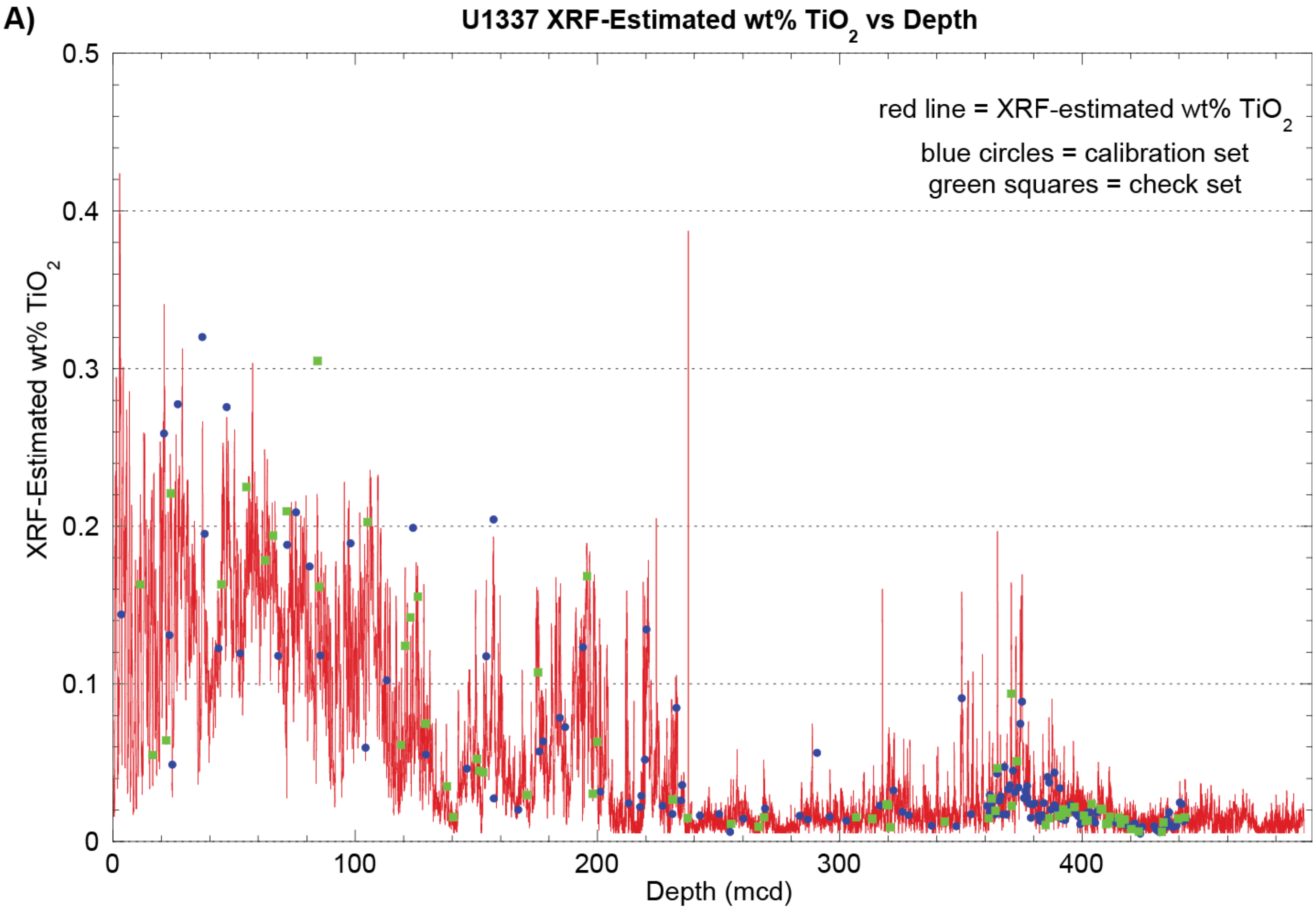

Figure B7 U1337 TiO2 NMS calibration. Calibration of U1337 TiO_2 NMS data using discrete samples analyzed post-cruise at Texas A&M University. A) XRF-predicted wt% TiO_2 versus depth with calibration and check data sets included.

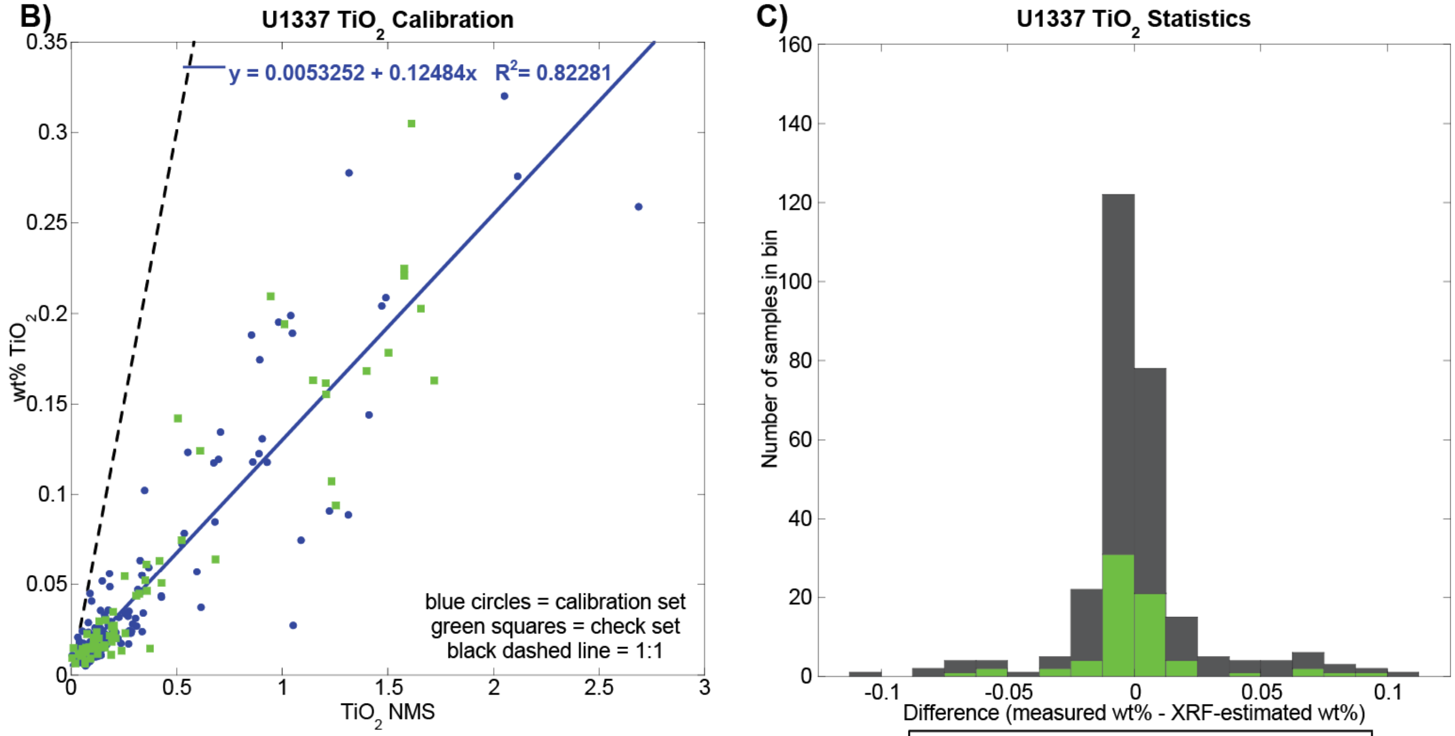

Measured - Estimated wt% TiO_2		
	Full Data Set	**Check Data Set**
Minimum	-0.109	-0.068
Maximum	0.108	0.098
Sum	0.048	0.048
Points	209	70
Mean	0.000	0.001
Median	-0.002	-0.001
RMS	0.026	0.025
Std Deviation	0.026	0.026
Variance	0.001	0.001
Std Error	0.002	0.003
Skewness	0.441	1.313
Kurtosis	5.361	5.056

Figure B7 (cont) U1337 TiO2 NMS calibration (cont). B) Calibration curve: A total of 209 discrete samples were used, 139 as the calibration set and 70 as the check set. A linear relationship was found between the TiO_2 NMS and wt% TiO_2 data, with a correlation of R^2 = 0.82281. C) Statistics for the full and check data sets.

`

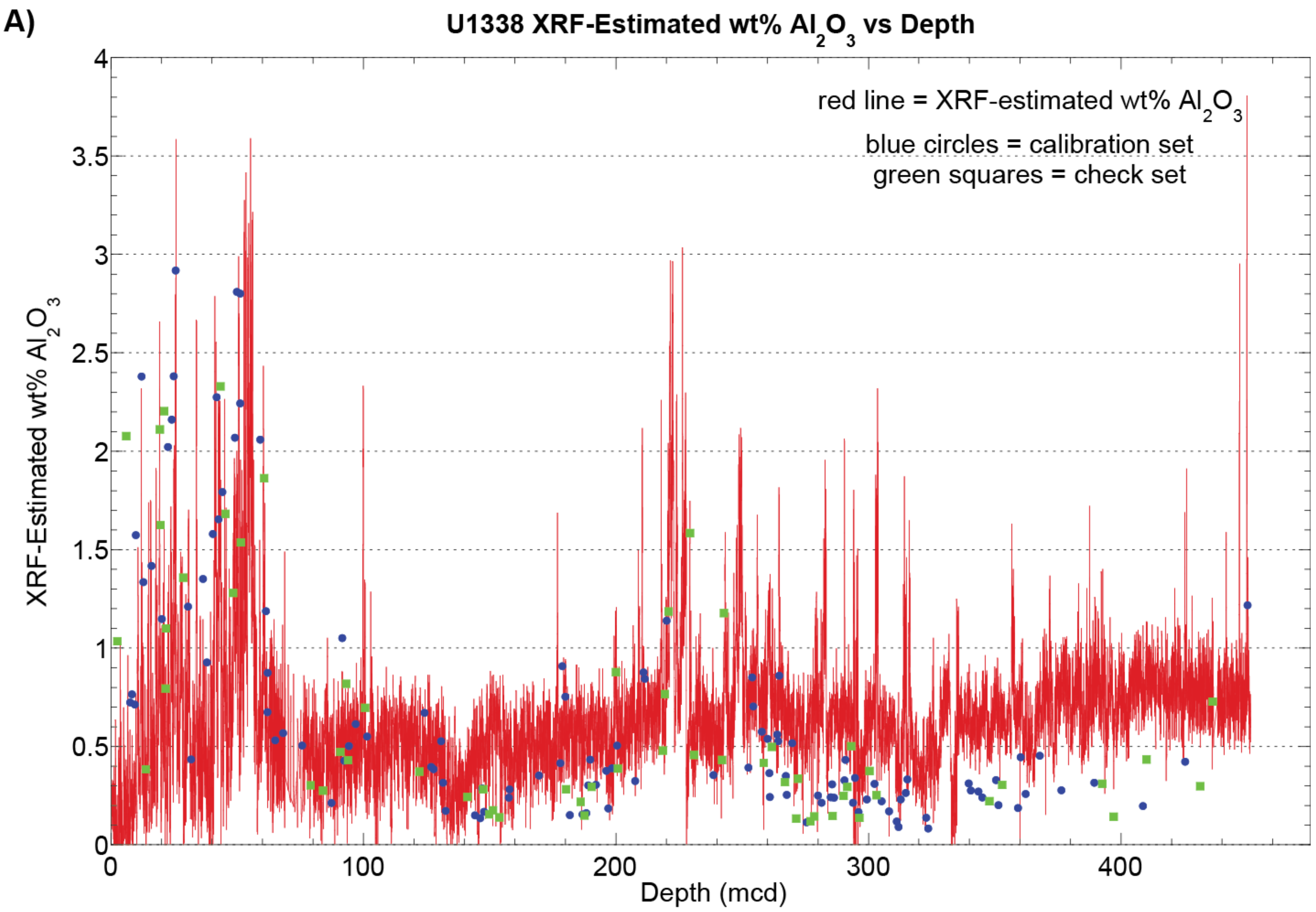

Figure B8 U1338 Al_2O_3 NMS calibration. Calibration of U1338 Al_2O_3 NMS data using shipboard geochemical data [*Expedition 320/321 Scientists*, 2010d] and discrete samples analyzed post-cruise at Texas A&M University. A) XRF-predicted wt% Al_2O_3 versus depth with calibration and check data sets included.

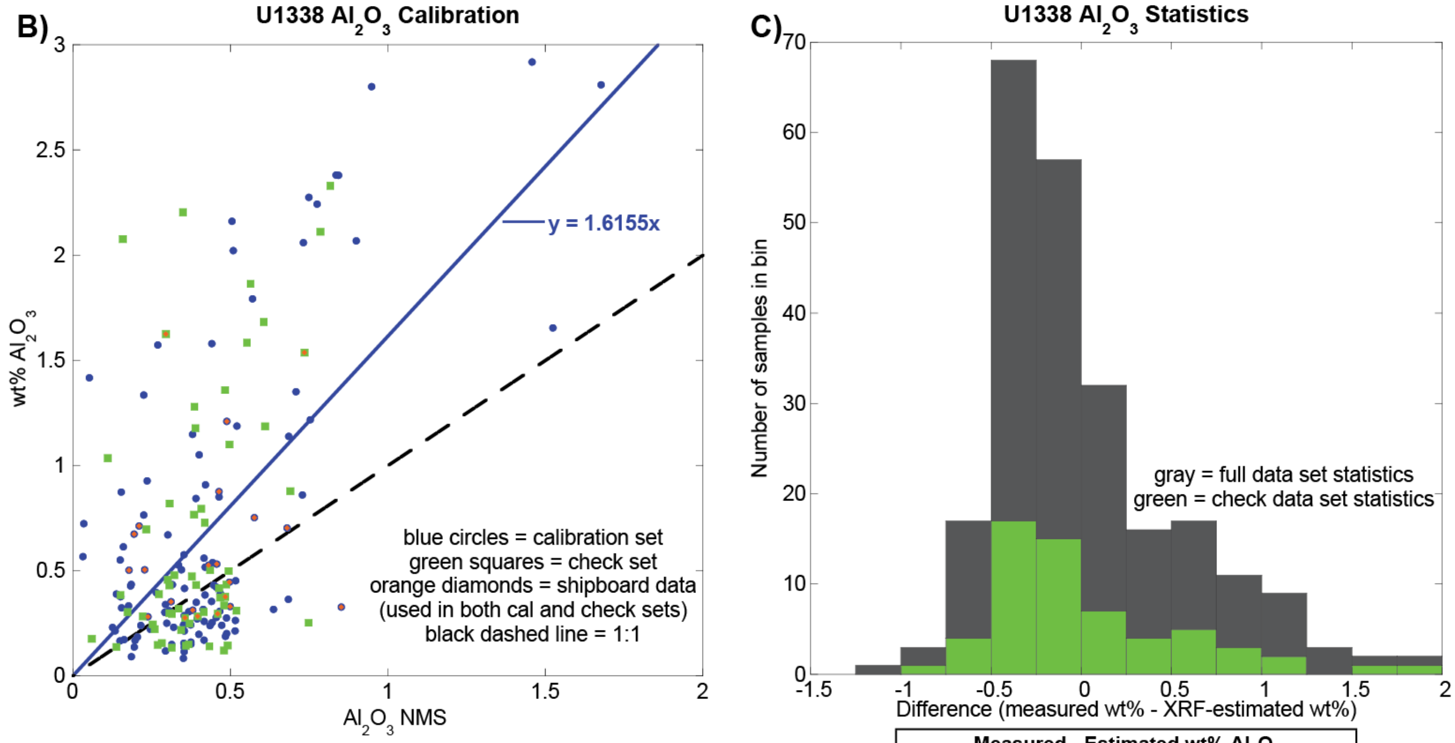

Figure B8 (cont) U1338 Al_2O_3 NMS calibration (cont). B) Calibration curve: A total of 178 discrete samples were used, 118 as the calibration set and 60 as the check set. The best-fit line has been forced through zero. C) Statistics for the full and check data sets.

Measured - Estimated wt% Al_2O_3		
	Full Data Set	**Check Data Set**
Minimum	-1.050	-0.956
Maximum	1.820	1.820
Sum	1.479	1.821
Points	178	60
Mean	0.008	0.030
Median	-0.149	-0.151
RMS	0.520	0.552
Std Deviation	0.521	0.556
Variance	0.272	0.309
Std Error	0.039	0.072
Skewness	1.038	1.208
Kurtosis	0.784	1.303

`

A)

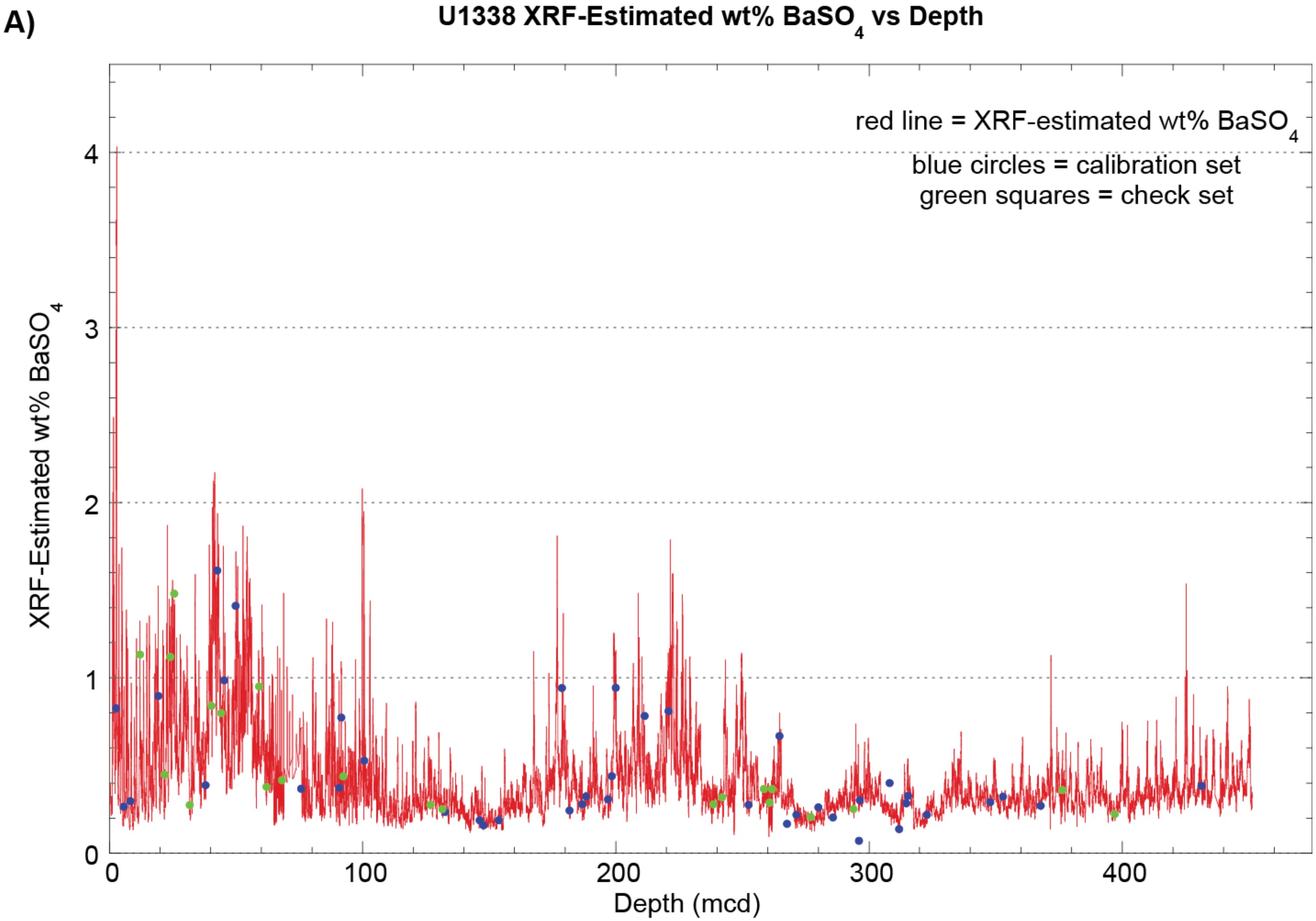

Figure B9 U1338 $BaSO_4$ NMS calibration. Calibration of U1338 $BaSO_4$ NMS data using discrete samples analyzed post-cruise at Texas A&M University. A) XRF-predicted wt% $BaSO_4$ versus depth with calibration and check data sets included.

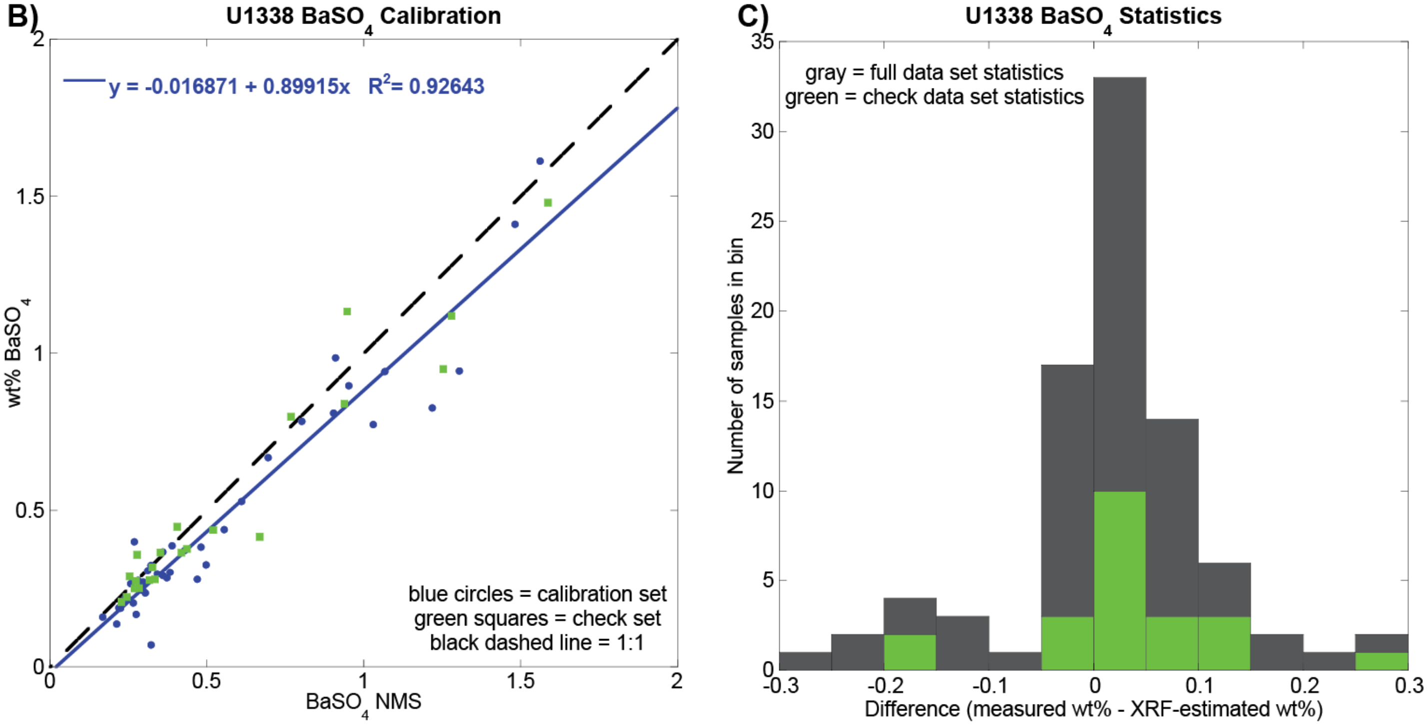

Figure B9 (cont) U1338 $BaSO_4$ NMS calibration (cont). B) Calibration curve: A total of 64 discrete samples were used, 42 as the calibration set and 22 as the check set. A linear relationship was found between the $BaSO_4$ NMS and wt% $BaSO_4$ data, with a correlation of R^2 = 0.92643. C) Statistics for the full and check data sets.

Measured - Estimated wt% $BaSO_4$		
	Full Data Set	**Check Data Set**
Minimum	-0.253	-0.168
Maximum	0.298	0.298
Sum	0.695	0.695
Points	64	22
Mean	0.011	0.032
Median	0.0123	0.019
RMS	0.094	0.097
Std Deviation	0.094	0.094
Variance	0.009	0.009
Std Error	0.012	0.020
Skewness	-0.179	0.344
Kurtosis	1.762	2.348

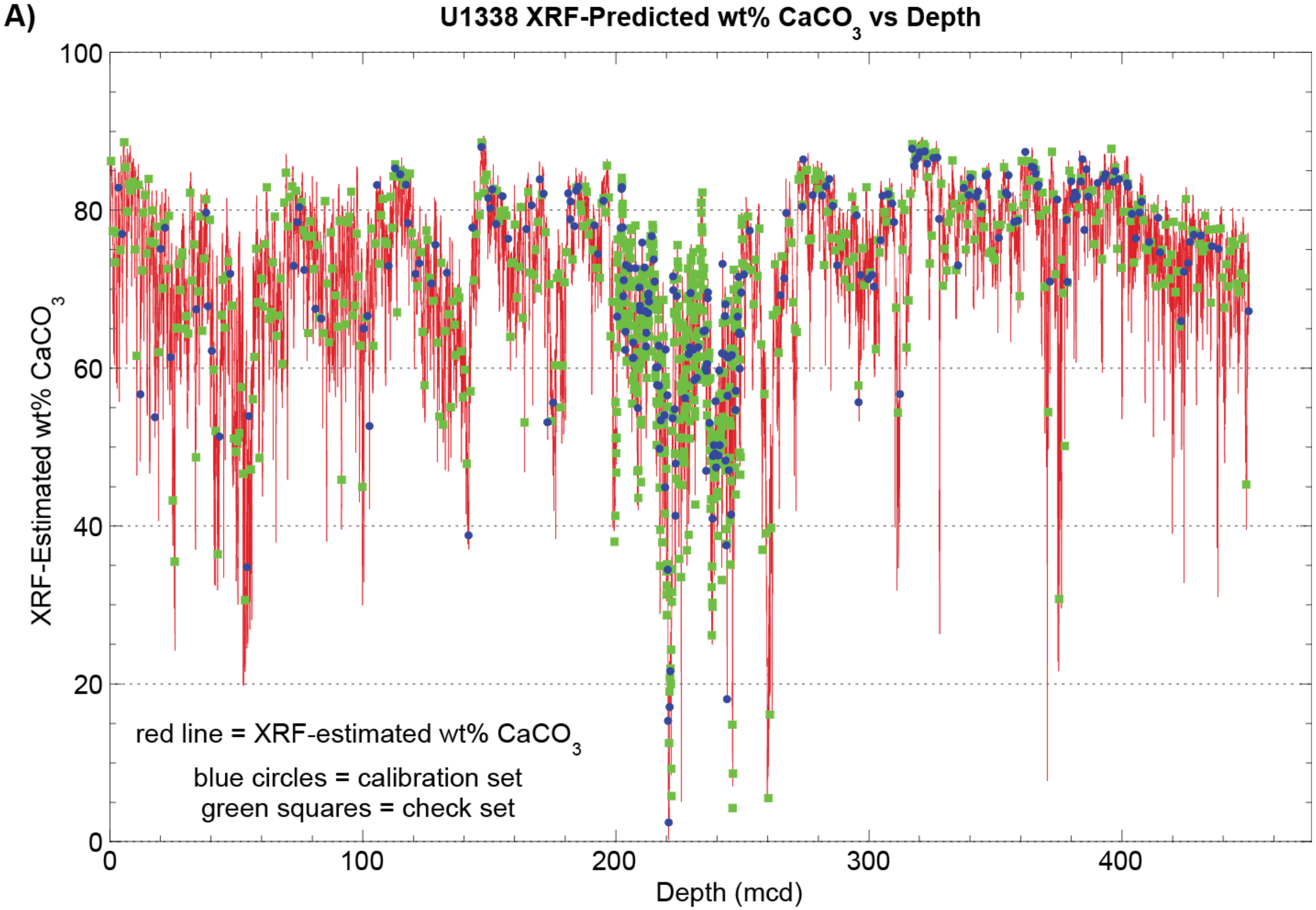

Figure B10 U1338 CaCO$_3$ NMS calibration. Calibration of U1338 CaCO$_3$ NMS data from *Lyle and Backman* [2013]. Previously published data has been replotted on the mcd depth scale for easier comparison with project data. A) XRF-predicted wt% CaCO$_3$ versus depth with calibration and check data sets included.

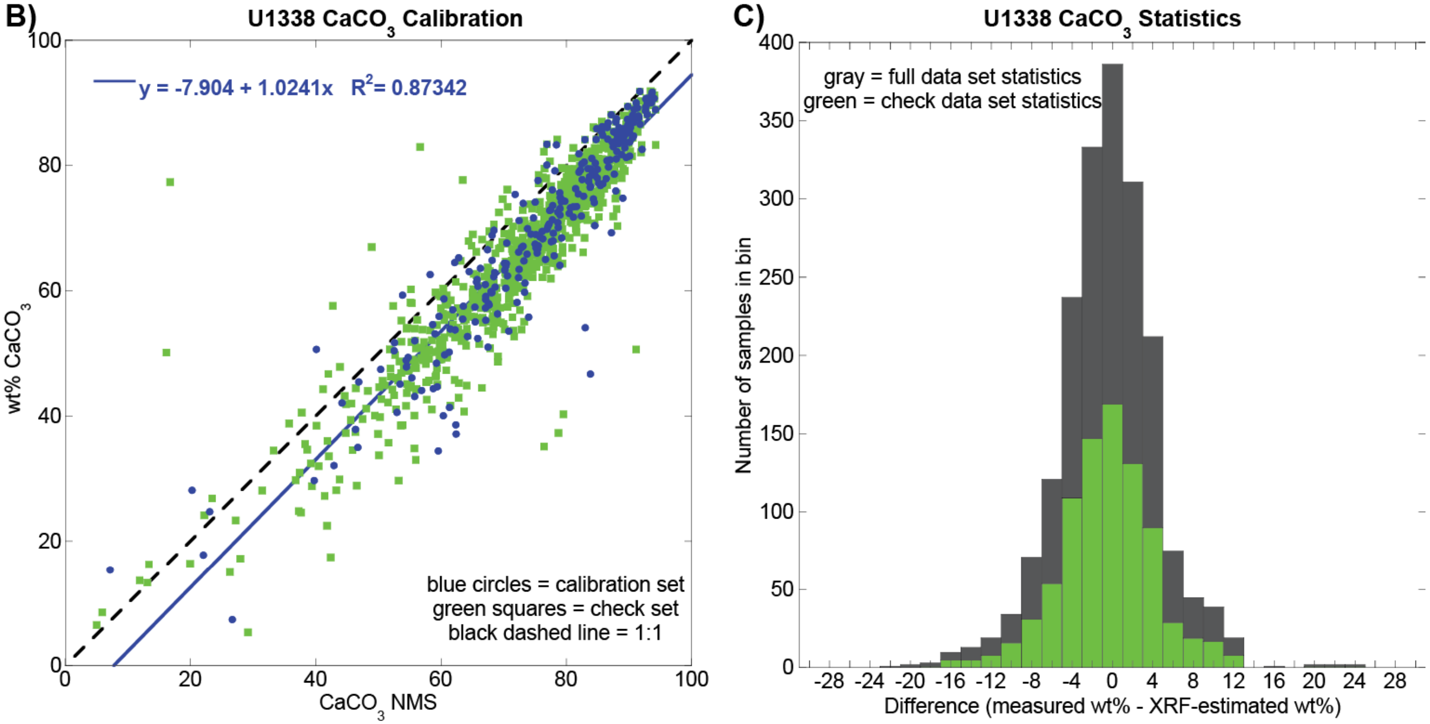

Measured - Estimated wt% CaCO$_3$		
	Full Data Set	**Check Data Set**
Minimum	-35.442	-19.625
Maximum	68.103	31.894
Sum	-508.953	-668.077
Points	1104	843
Mean	-0.461	-0.792
Median	-0.321	-0.699
RMS	6.052	5.047
Std Deviation	6.037	4.987
Variance	36.441	24.871
Std Error	0.182	0.172
Skewness	0.934	0.246
Kurtosis	21.871	3.790

Figure B10 (cont) U1338 CaCO$_3$ NMS calibration (cont).
B) Calibration curve: A total of 1104 discrete samples were used, 261 as the calibration set and 843 as the check set. A linear relationship was found between the CaCO$_3$ NMS and wt% CaCO$_3$ data, with a correlation of R^2 = 0.96336.
C) Statistics for the full and check data sets.

`

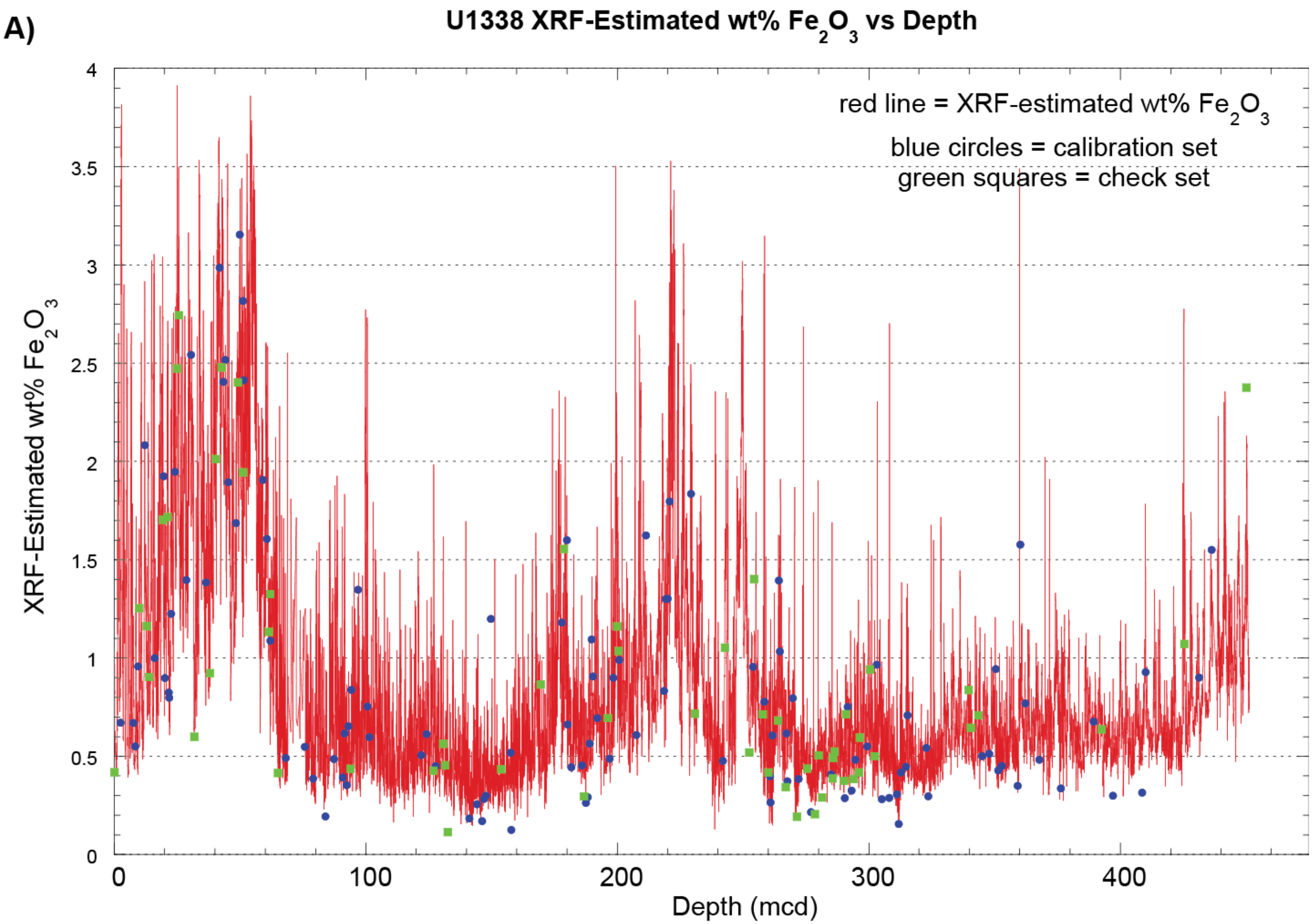

Figure B11 U1338 Fe_2O_3 NMS calibration. Calibration of U1338 Fe_2O_3 NMS data using shipboard geochemical data [*Expedition 320/321 Scientists*, 2010d] and discrete samples analyzed post-cruise at Texas A&M University. A) XRF-predicted wt% Fe_2O_3 versus depth with calibration and check data sets included.

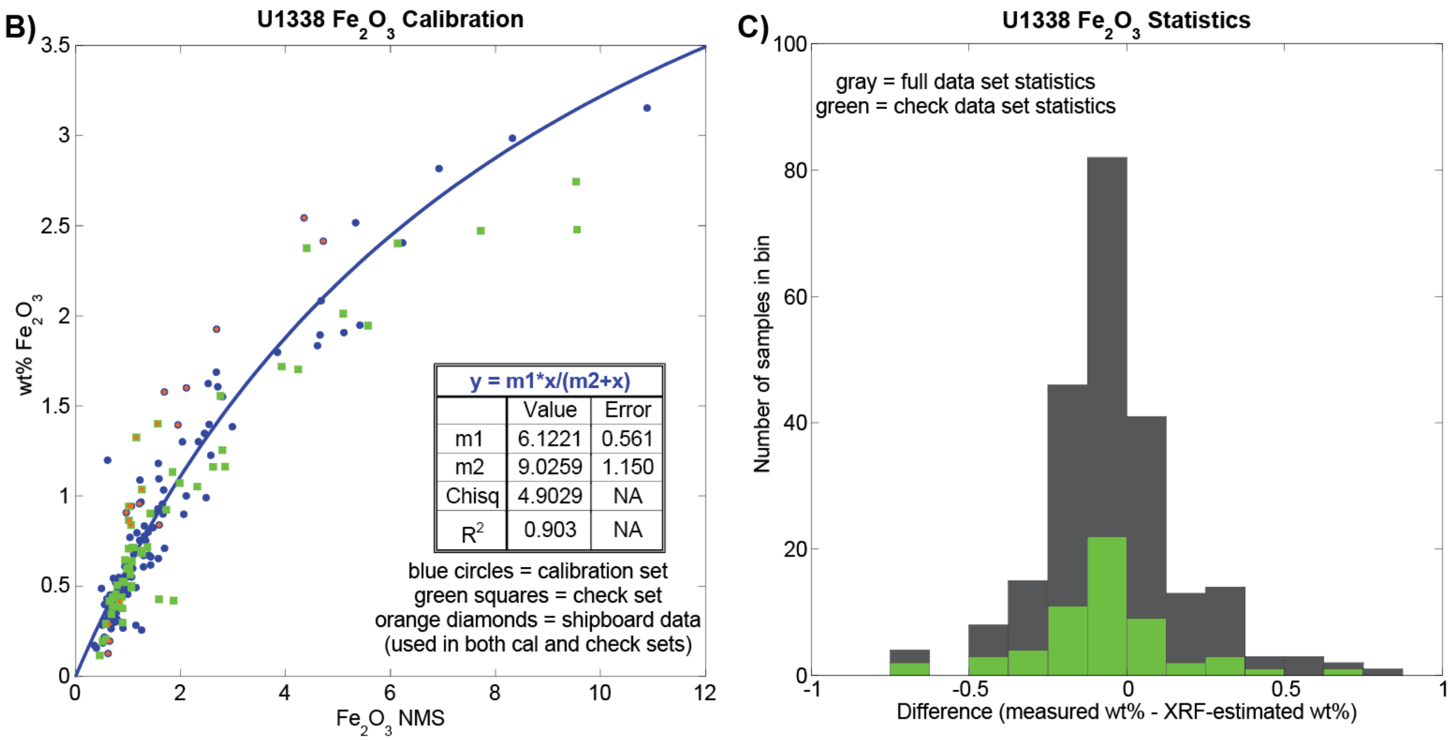

y = m1*x/(m2+x)

	Value	Error
m1	6.1221	0.561
m2	9.0259	1.150
Chisq	4.9029	NA
R^2	0.903	NA

Figure B11 (cont) U1338 Fe_2O_3 NMS calibration (cont). B) Calibration curve: A total of 174 discrete samples were used, 116 as the calibration set and 58 as the check set. The data do not follow a linear trend, rather the Michaelis-Menten equation was used to determine the best fit and predict wt% Fe_2O_3. The $R^2 = 0.90267$. C) Statistics for the full and check data sets.

Measured - Estimated wt% Fe_2O_3

	Full Data Set	**Check Data Set**
Minimum	-0.669	-0.669
Maximum	0.812	0.630
Sum	-5.228	-3.746
Points	174	58
Mean	-0.030	-0.065
Median	-0.052	-0.071
RMS	0.217	0.238
Std Deviation	0.215	0.231
Variance	0.046	0.053
Std Error	0.016	0.030
Skewness	0.693	0.216
Kurtosis	2.141	1.573

`

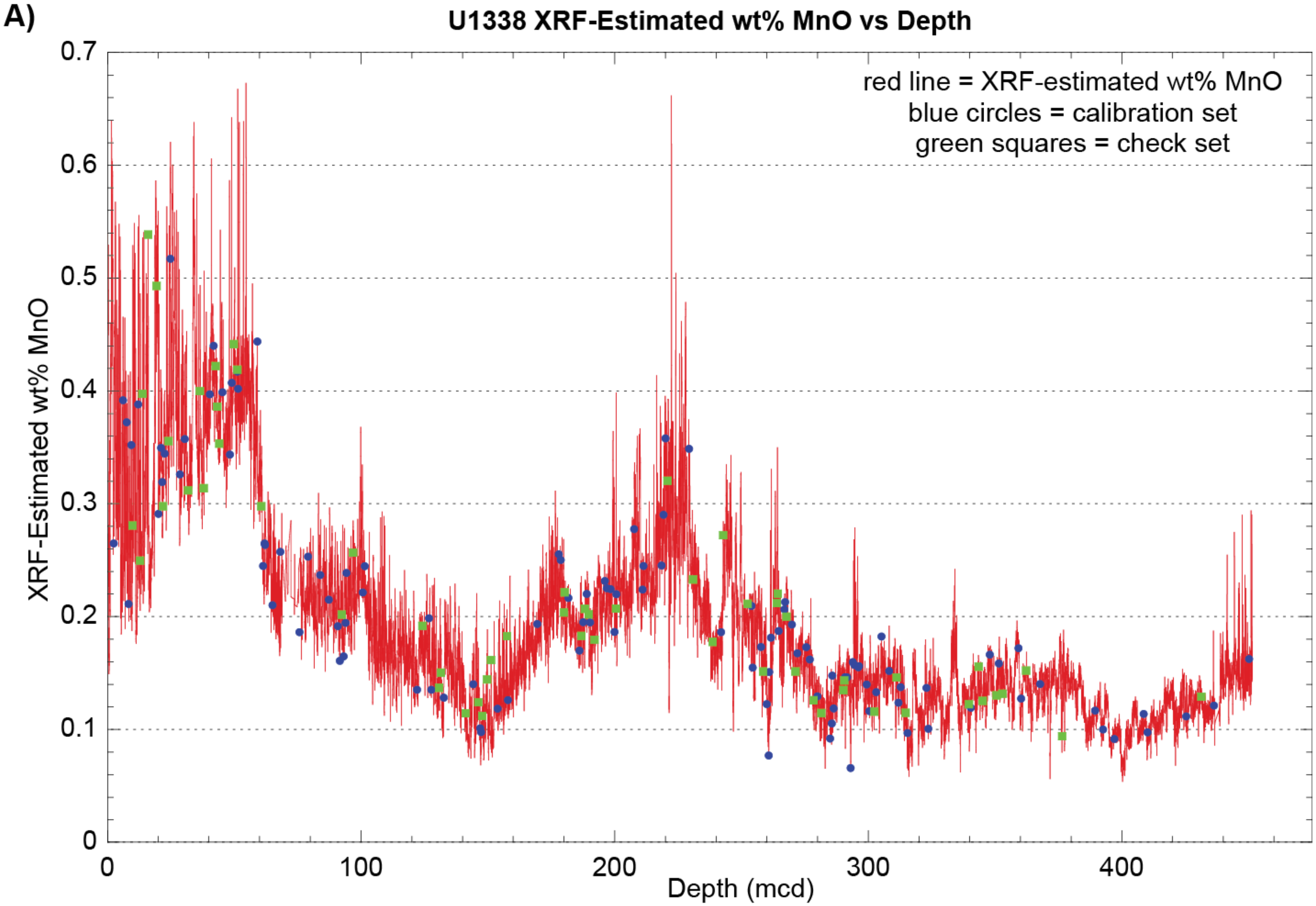

Figure B12 U1338 MnO NMS calibration. Calibration of U1338 MnO NMS data using shipboard geochemical data [*Expedition 320/321 Scientists*, 2010d] and discrete samples analyzed post-cruise at Texas A&M University. A) XRF-predicted wt% MnO versus depth with calibration and check data sets included.

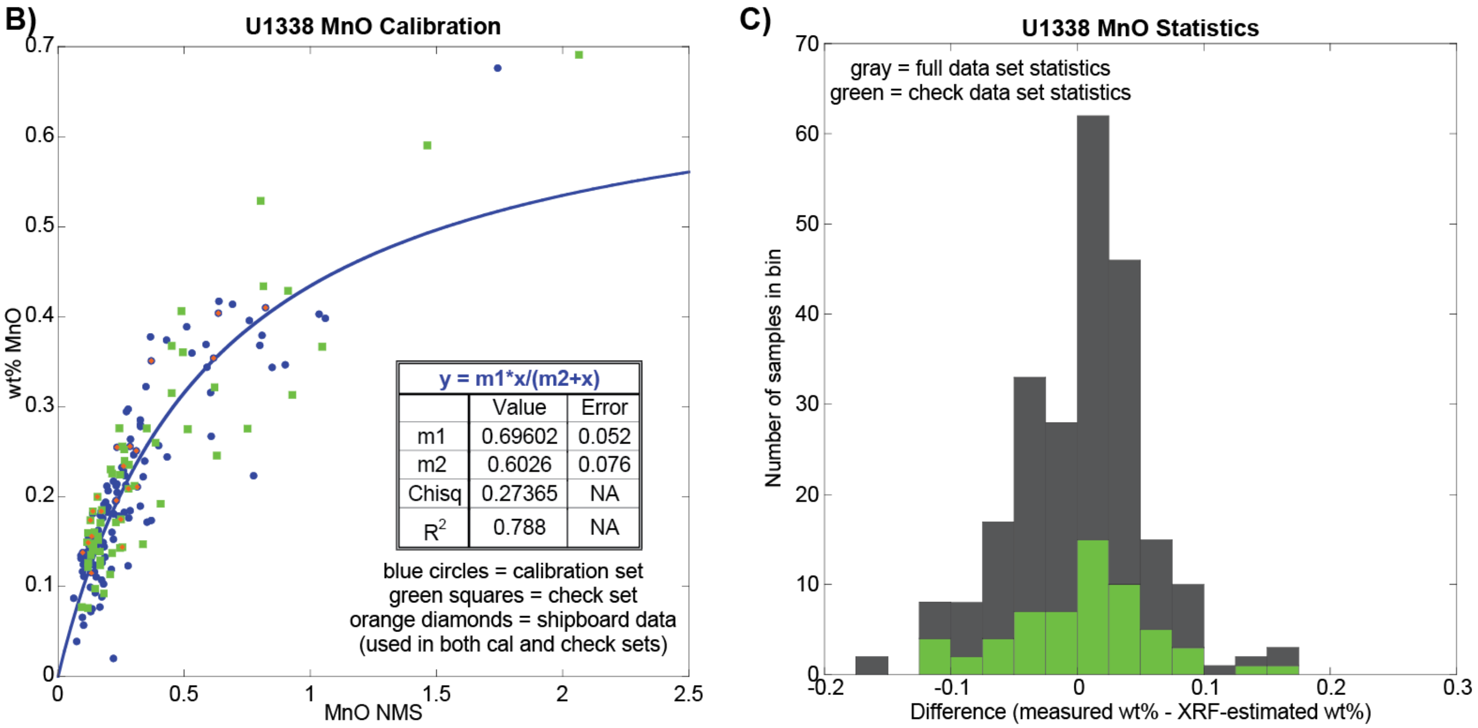

y = m1*x/(m2+x)

	Value	Error
m1	0.69602	0.052
m2	0.6026	0.076
Chisq	0.27365	NA
R^2	0.788	NA

Figure B12 (cont) U1338 MnO NMS calibration (cont). B) Calibration curve: A total of 176 discrete samples were used, 117 as the calibration set and 59 as the check set. The data do not follow a linear trend, rather the Michaelis-Menten equation was used to determine the best fit and predict wt% MnO. The $R^2 = 0.78839$. C) Statistics for the full and check data sets.

Measured - Estimated wt% MnO

	Full Data Set	**Check Data Set**
Minimum	-0.168	-0.110
Maximum	0.159	0.152
Sum	0.294	0.213
Points	176	59
Mean	0.002	0.004
Median	0.011	0.011
RMS	0.051	0.056
Std Deviation	0.051	0.057
Variance	0.003	0.003
Std Error	0.004	0.007
Skewness	-0.240	0.001
Kurtosis	1.136	0.089

`

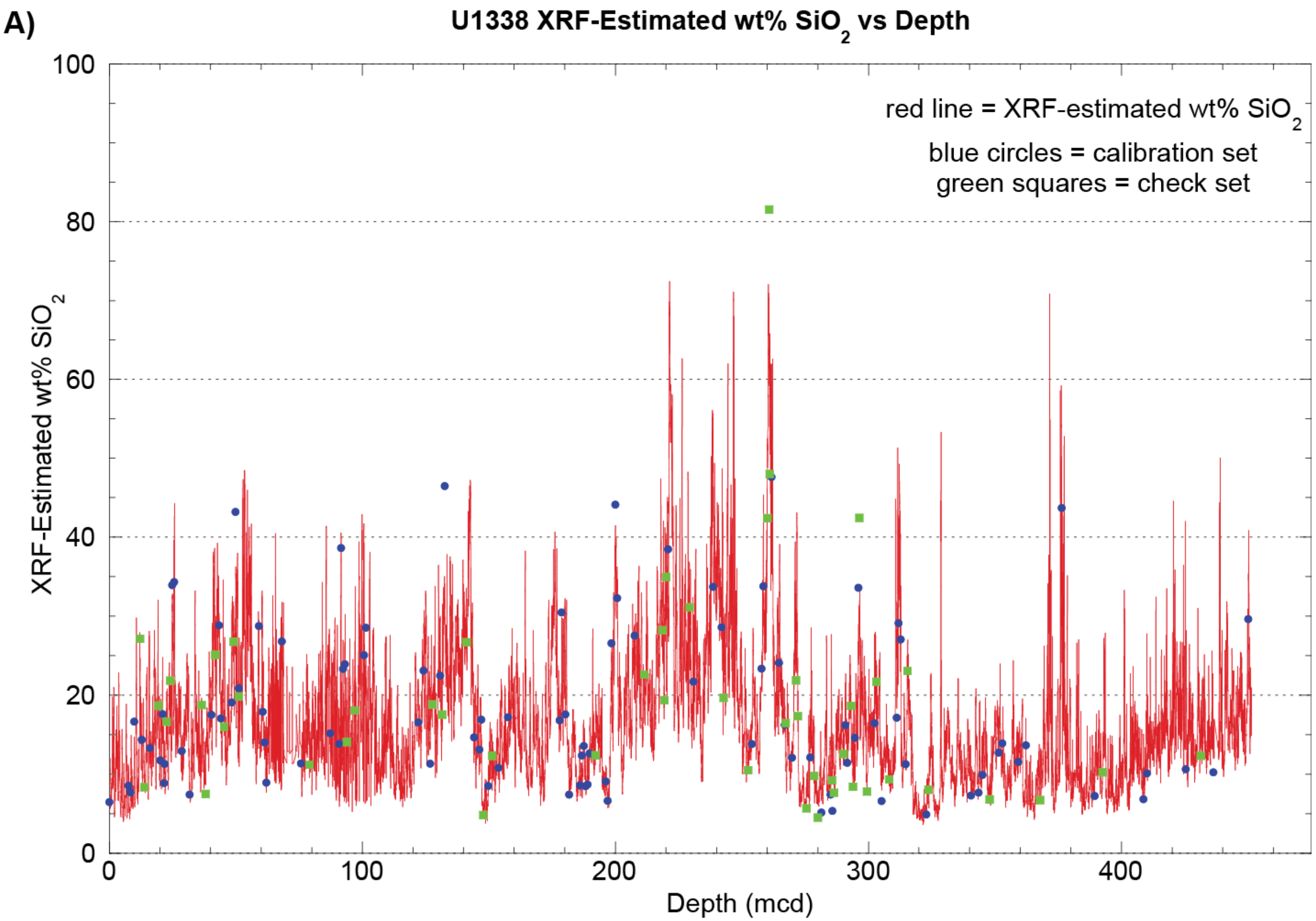

Figure B13 U1338 SiO_2 NMS calibration. Calibration of U1338 SiO_2 NMS data using discrete samples analyzed post-cruise at Texas A&M University. (A upper panel) XRF-predicted wt% SiO_2 versus depth with calibration and check data sets included.

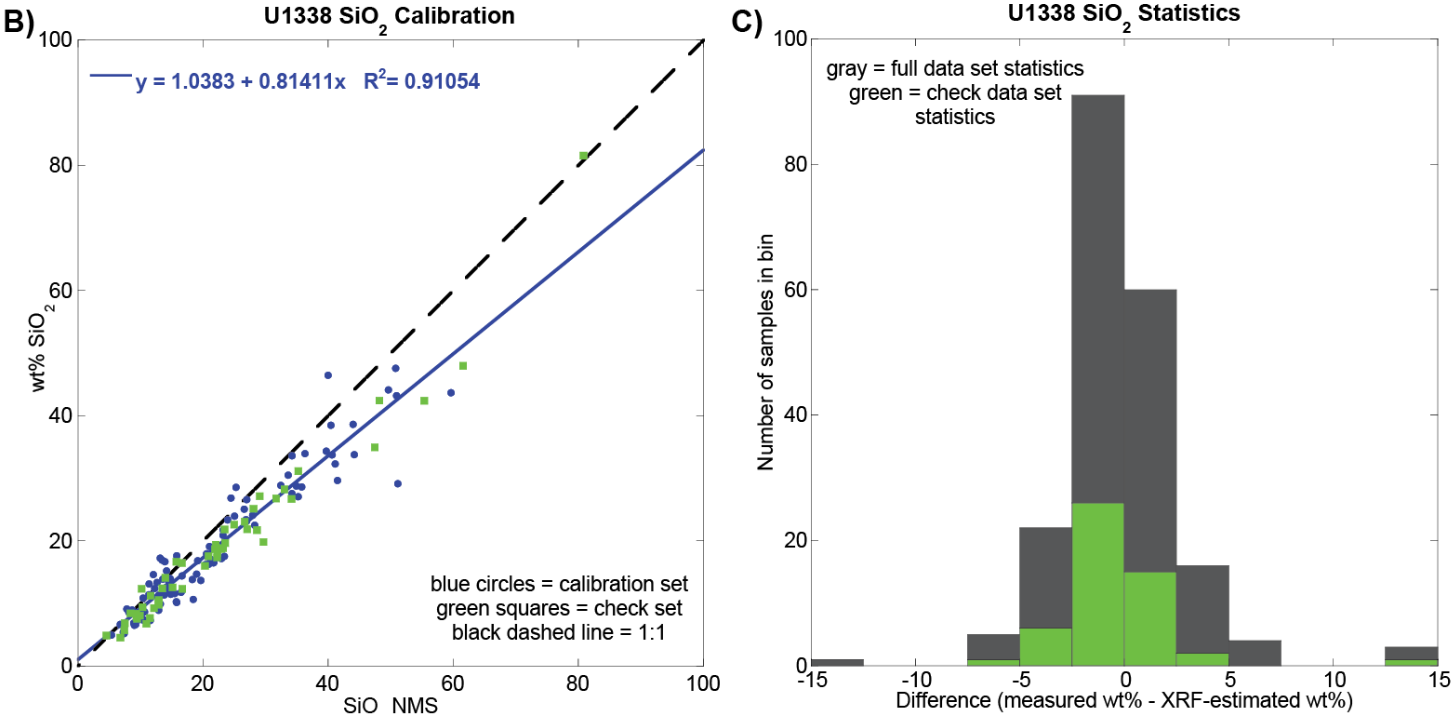

Figure B13 (cont) U1338 SiO$_2$ NMS calibration (cont). B) Calibration curve: A total of 151 discrete samples were used, 100 as the calibration set and 51 as the check set. A linear relationship was found between the SiO$_2$ NMS and wt% SiO$_2$ data, with a correlation of R^2 = 0.91054. C) Statistics for the full and check data sets.

Measured - Estimated wt% SiO$_2$

	Full Data Set	Check Data Set
Minimum	-13.576	-5.351
Maximum	14.709	14.709
Sum	-16.088	-16.084
Points	151	51
Mean	-0.107	-0.315
Median	-0.320	-0.765
RMS	3.013	2.798
Std Deviation	3.021	2.808
Variance	9.129	7.883
Std Error	0.246	0.393
Skewness	0.841	2.898
Kurtosis	6.954	14.319

`

A)

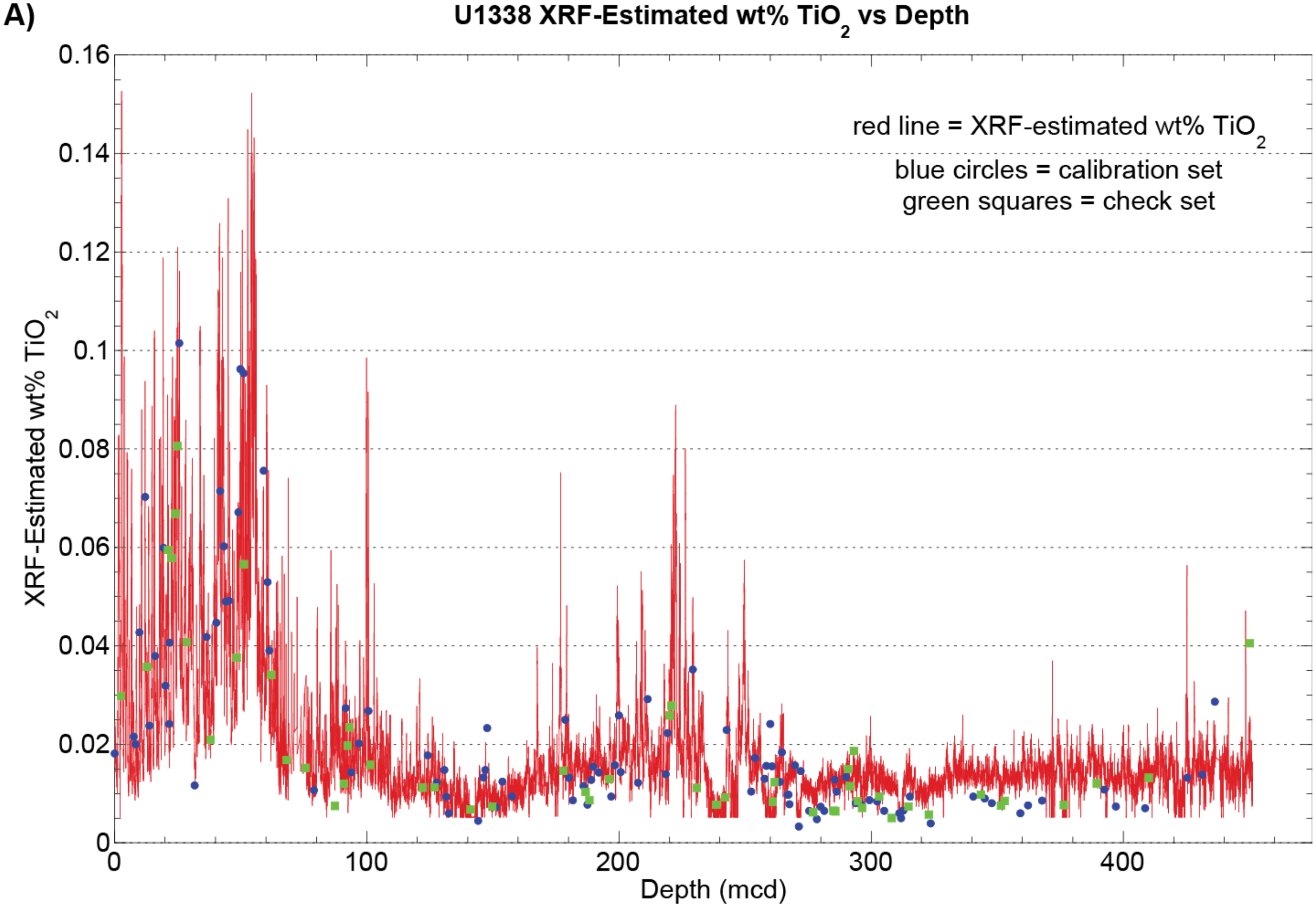

Figure B14 U1338 TiO$_2$ NMS calibration. Calibration of U1338 TiO$_2$ NMS data using discrete samples analyzed post-cruise at Texas A&M University. A) XRF-predicted wt% TiO$_2$ versus depth with calibration and check data sets included.

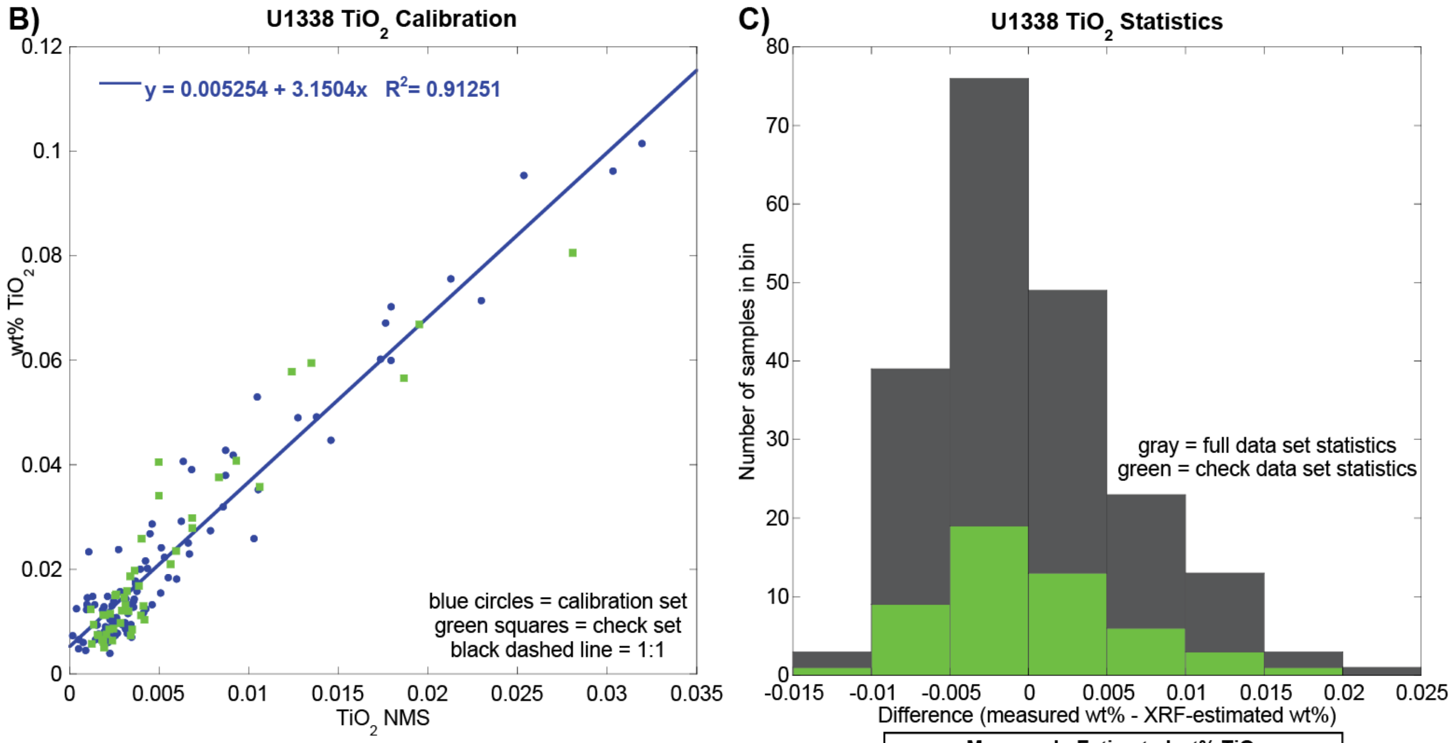

Measured - Estimated wt% TiO_2		
	Full Data Set	**Check Data Set**
Minimum	-0.013	-0.013
Maximum	0.023	0.020
Sum	0.004	0.004
Points	155	52
Mean	2.784e-05	8.316e-05
Median	-0.001	-0.000
RMS	0.006	0.006
Std Deviation	0.006	0.006
Variance	3.816e-05	3.860e-05
Std Error	0.001	0.001
Skewness	0.954	0.77685647
Kurtosis	1.014	0.950

Figure B14 (cont) U1338 TiO_2 NMS calibration (cont). B) Calibration curve: A total of 155 discrete samples were used, 103 as the calibration set and 52 as the check set. A linear relationship was found between the TiO_2 NMS and wt% TiO_2 data, with a correlation of $R^2 = 0.91251$.
C) Statistics for the full and check data sets.

`

APPENDIX C

This appendix includes calibrated data tables and calibration figures, as referenced in Chapter IV. For the larger data tables, only the first page has been printed and included in this document. The complete tables are available as supplementary Microsoft Excel (.xls) files.

Table C1 Neogene PEAT drilling locations. In addition to current latitude, longitude, and water depth, paleolatitude at 10 and 17 Ma and crustal ages have been included.

	Latitude (N)	Longitude (W)	Paleolatitude (N)		Water Depth (m)	Crustal Age (Ma)
			10 Ma	17 Ma		
U1335	~05°18.7'	~126°17.0'	~02°45’	~01°00’	~4300	~26
U1336	~07°42.0'	~128°15.2'	~05°00’	~03°20’	~4200	~32
U1337	~03°50.0'	~123°12.3'	~01°15’	~-00°25’	~4400	~24
U1338	~02°30.5'	~117°58.2'	~00°15’	~-01°30’	~4200	~18

`

Table C2 Neogene PEAT cores with age and U1337 equivalent depth.

U1335				U1336				U1337			U1338			
Age (Ma)	U1335 Depth (mcd)	U1337 Equiv. Depth (mcd)	XRF-Estimated wt% $CaCO_3$	Age (Ma)	U1336 Depth (mcd)	U1337 Equiv. Depth (mcd)	XRF-Estimated wt% $CaCO_3$	Age (Ma)	Depth (mcd)	XRF-Estimated wt% $CaCO_3$	Age (Ma)	U1338 Depth (mcd)	U1337 Equiv. Depth (mcd)	XRF-Estimated wt% $CaCO_3$
14.999	97.100	336.509	84.875	14.998	36.100	336.484	86.611	14.999	336.490	80.823	14.999	405.715	335.758	75.179
15.002	97.125	336.555	84.178	15.000	36.125	336.524	86.811	15.000	336.515	84.449	15.001	405.740	335.773	74.362
15.003	97.150	336.578	83.343	15.002	36.150	336.564	87.300	15.001	336.540	82.353	15.004	405.815	335.818	75.048
15.004	97.175	336.601	84.962	15.004	36.175	336.605	87.317	15.002	336.565	83.895	15.005	405.840	335.832	72.311
15.005	97.225	336.624	85.675	15.006	36.200	336.645	86.322	15.004	336.590	82.501	15.006	405.865	335.847	76.168
15.006	97.250	336.647	85.712	15.010	36.250	336.726	84.260	15.005	336.615	81.763	15.008	405.890	335.862	75.919
15.008	97.275	336.670	84.694	15.011	36.275	336.766	84.599	15.006	336.640	80.794	15.009	405.915	335.877	74.381
15.009	97.300	336.693	84.510	15.013	36.300	336.806	82.969	15.007	336.665	82.740	15.010	405.940	335.892	79.356
15.009	97.325	336.716	84.325	15.015	36.325	336.847	81.761	15.008	336.690	81.125	15.010	405.965	335.907	78.131
15.010	97.350	336.739	83.313	15.017	36.350	336.887	78.806	15.009	336.715	80.713	15.011	405.990	335.922	76.726
15.011	97.375	336.762	82.326	15.019	36.375	336.927	77.694	15.010	336.740	80.852	15.012	406.015	335.937	75.281
15.012	97.400	336.785	80.795	15.021	36.400	336.968	76.959	15.011	336.765	82.325	15.014	406.040	335.952	75.321
15.013	97.425	336.807	81.804	15.023	36.425	337.008	69.792	15.013	336.790	82.104	15.015	406.065	335.967	79.567
15.015	97.475	336.830	80.826	15.025	36.450	337.048	69.864	15.014	336.815	83.650	15.016	406.090	335.982	81.019
15.016	97.500	336.853	83.311	15.027	36.475	337.089	71.495	15.015	336.840	84.172	15.017	406.115	335.997	80.017
15.017	97.525	336.876	81.066	15.029	36.500	337.129	74.011	15.016	336.865	84.787	15.018	406.140	336.012	78.599
15.018	97.550	336.899	82.942	15.031	36.525	337.169	72.395	15.018	336.890	83.957	15.019	406.165	336.027	76.218
15.019	97.575	336.922	82.738	15.034	36.550	337.210	65.338	15.019	336.915	83.666	15.021	406.190	336.042	76.159
15.020	97.600	336.945	82.285	15.036	36.575	337.252	63.340	15.020	336.940	83.904	15.022	406.215	336.057	73.129
15.021	97.625	336.968	84.234	15.038	36.600	337.298	78.532	15.021	336.965	85.468	15.023	406.240	336.072	70.820
15.023	97.650	336.991	84.083	15.040	36.625	337.343	82.251	15.023	336.990	83.942	15.024	406.265	336.087	74.159
15.024	97.675	337.014	83.325	15.042	36.650	337.389	78.820	15.024	337.015	84.603	15.025	406.290	336.102	73.970
15.025	97.700	337.037	82.977	15.045	36.675	337.435	78.296	15.025	337.040	83.415	15.026	406.315	336.117	74.940
15.026	97.725	337.060	82.762	15.047	36.700	337.481	80.920	15.026	337.065	81.947	15.028	406.340	336.131	75.063
15.027	97.750	337.083	83.202	15.049	36.725	337.527	80.950	15.028	337.090	82.041	15.029	406.365	336.146	76.551
15.028	97.775	337.106	82.508	15.051	36.750	337.573	83.845	15.029	337.115	80.593	15.030	406.390	336.161	72.745
15.029	97.800	337.129	81.195	15.053	36.775	337.619	86.293	15.030	337.140	79.980	15.031	406.415	336.176	81.503
15.031	97.825	337.152	80.993	15.055	36.800	337.665	88.006	15.031	337.165	78.694	15.032	406.440	336.191	80.030
15.032	97.850	337.175	79.434	15.058	36.825	337.710	87.019	15.033	337.190	78.812	15.033	406.465	336.206	81.209
15.033	97.875	337.198	79.161	15.060	36.850	337.756	88.092	15.034	337.215	77.567	15.035	406.490	336.221	77.436
15.034	97.900	337.221	77.936	15.062	36.875	337.802	89.155	15.035	337.240	74.595	15.036	406.515	336.236	81.076
15.035	97.925	337.241	78.485	15.064	36.900	337.848	88.941	15.036	337.265	79.630	15.037	406.540	336.251	81.201

`

Table C3 Neogene PEAT cores bio- and magnetostratigraphic datums. Age, depth, $CaCO_3$ NMS data, and stratigraphic data are presented and were used in the initial correlation of U1335, U1336, U1337, and U1338.

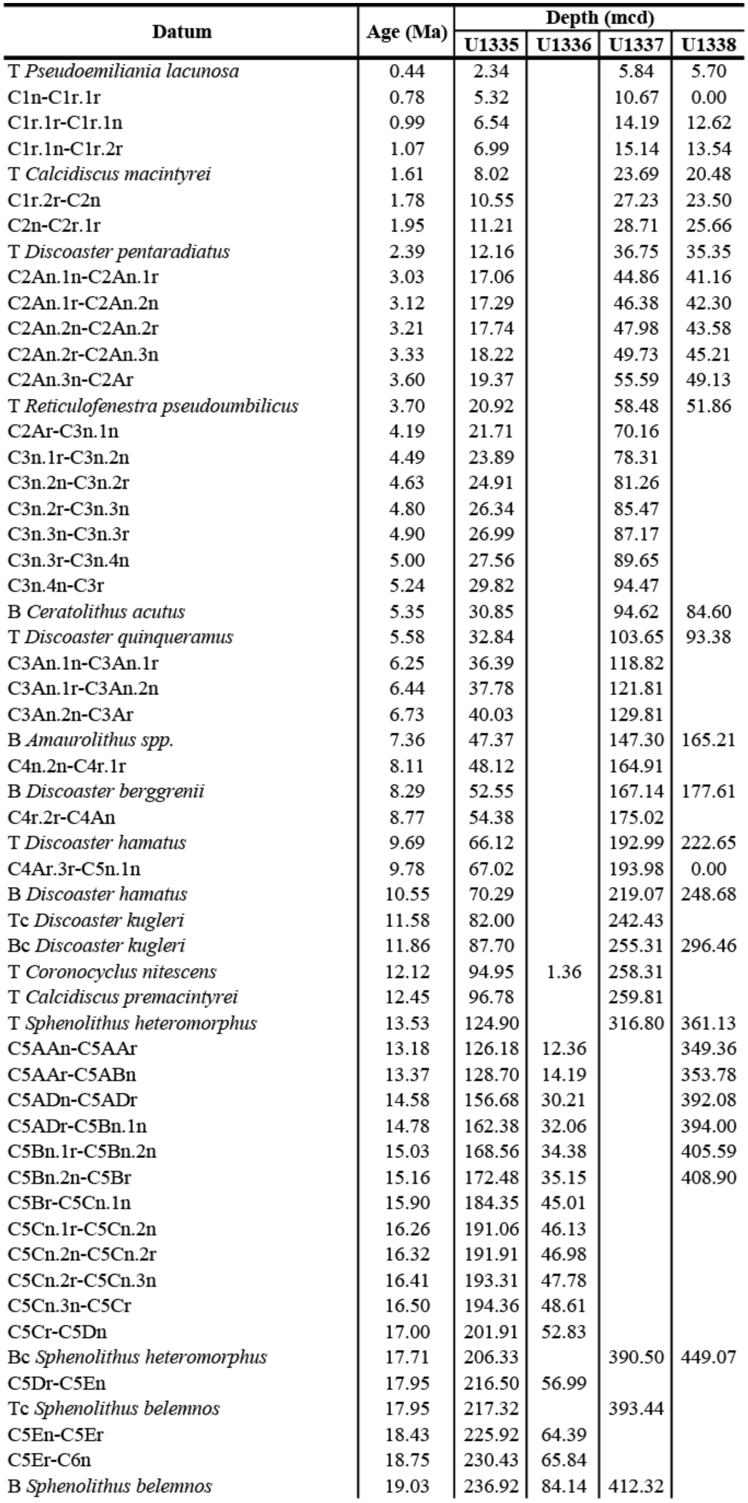

Datum	Age (Ma)	Depth (mcd)			
		U1335	U1336	U1337	U1338
T *Pseudoemiliania lacunosa*	0.44	2.34		5.84	5.70
C1n-C1r.1r	0.78	5.32		10.67	0.00
C1r.1r-C1r.1n	0.99	6.54		14.19	12.62
C1r.1n-C1r.2r	1.07	6.99		15.14	13.54
T *Calcidiscus macintyrei*	1.61	8.02		23.69	20.48
C1r.2r-C2n	1.78	10.55		27.23	23.50
C2n-C2r.1r	1.95	11.21		28.71	25.66
T *Discoaster pentaradiatus*	2.39	12.16		36.75	35.35
C2An.1n-C2An.1r	3.03	17.06		44.86	41.16
C2An.1r-C2An.2n	3.12	17.29		46.38	42.30
C2An.2n-C2An.2r	3.21	17.74		47.98	43.58
C2An.2r-C2An.3n	3.33	18.22		49.73	45.21
C2An.3n-C2Ar	3.60	19.37		55.59	49.13
T *Reticulofenestra pseudoumbilicus*	3.70	20.92		58.48	51.86
C2Ar-C3n.1n	4.19	21.71		70.16	
C3n.1r-C3n.2n	4.49	23.89		78.31	
C3n.2n-C3n.2r	4.63	24.91		81.26	
C3n.2r-C3n.3n	4.80	26.34		85.47	
C3n.3n-C3n.3r	4.90	26.99		87.17	
C3n.3r-C3n.4n	5.00	27.56		89.65	
C3n.4n-C3r	5.24	29.82		94.47	
B *Ceratolithus acutus*	5.35	30.85		94.62	84.60
T *Discoaster quinqueramus*	5.58	32.84		103.65	93.38
C3An.1n-C3An.1r	6.25	36.39		118.82	
C3An.1r-C3An.2n	6.44	37.78		121.81	
C3An.2n-C3Ar	6.73	40.03		129.81	
B *Amaurolithus spp.*	7.36	47.37		147.30	165.21
C4n.2n-C4r.1r	8.11	48.12		164.91	
B *Discoaster berggrenii*	8.29	52.55		167.14	177.61
C4r.2r-C4An	8.77	54.38		175.02	
T *Discoaster hamatus*	9.69	66.12		192.99	222.65
C4Ar.3r-C5n.1n	9.78	67.02		193.98	0.00
B *Discoaster hamatus*	10.55	70.29		219.07	248.68
Tc *Discoaster kugleri*	11.58	82.00		242.43	
Bc *Discoaster kugleri*	11.86	87.70		255.31	296.46
T *Coronocyclus nitescens*	12.12	94.95	1.36	258.31	
T *Calcidiscus premacintyrei*	12.45	96.78		259.81	
T *Sphenolithus heteromorphus*	13.53	124.90		316.80	361.13
C5AAn-C5AAr	13.18	126.18	12.36		349.36
C5AAr-C5ABn	13.37	128.70	14.19		353.78
C5ADn-C5ADr	14.58	156.68	30.21		392.08
C5ADr-C5Bn.1n	14.78	162.38	32.06		394.00
C5Bn.1r-C5Bn.2n	15.03	168.56	34.38		405.59
C5Bn.2n-C5Br	15.16	172.48	35.15		408.90
C5Br-C5Cn.1n	15.90	184.35	45.01		
C5Cn.1r-C5Cn.2n	16.26	191.06	46.13		
C5Cn.2n-C5Cn.2r	16.32	191.91	46.98		
C5Cn.2r-C5Cn.3n	16.41	193.31	47.78		
C5Cn.3n-C5Cr	16.50	194.36	48.61		
C5Cr-C5Dn	17.00	201.91	52.83		
Bc *Sphenolithus heteromorphus*	17.71	206.33		390.50	449.07
C5Dr-C5En	17.95	216.50	56.99		
Tc *Sphenolithus belemnos*	17.95	217.32		393.44	
C5En-C5Er	18.43	225.92	64.39		
C5Er-C6n	18.75	230.43	65.84		
B *Sphenolithus belemnos*	19.03	236.92	84.14	412.32	